UNIVERSITÀ DEGLI STUDI DI NAPOLI
FEDERICO II

SCUOLA POLITECNICA E DELLE SCIENZE DI BASE

A microfluidic approach for membrane separation processes: investigation of fouling and its prevention strategies

Andrea Iginio Cirillo

Supervisor
Ch.mo Prof. G. Tomaiuolo

Scientific Committee
Ch.mo Prof. S. Guido
Ch.mo Prof. W. A. Phillip
Dott. V. R. Villella

A thesis presented for the degree of Doctor of Philosophy in Products and Industrial Processes Engineering

List of Contents

Abstract

By meeting the principles of sustainability which characterize contemporary process intensification strategies, membrane technologies are gradually replacing conventional energy-intensive separation techniques and reactive processes. One of the most important applications of membrane technologies is represented by separation operations based on pressure and concentration differences, e.g., membrane filtration and osmotic processes, where higher product concentration and purity are achieved by exploiting the ability of membranes to regulate the permeation rate of species through the pores.

However, a critical issue undermines the performance of membrane processes, that is the progressive decrease of permeate flux due to fouling. Despite all the research efforts so far, fouling still represents an unsolved problem. The complex interplay of physical and chemical mechanisms governing its evolution is indeed yet to be fully unraveled and the role played by foulants' properties or operating conditions is an area of active research. An interesting approach to fouling investigation concerns the use of microfluidic systems in which low amounts of fluid are processed in channels whose diameter can reach a few micrometers. Indeed, flux decline is governed by events occurring at small time and spatial scales, the latter comparable to pore dimensions. Studying fouling in micro-sized geometries would therefore allow gaining key insights regarding the interactions between foulants and the membrane surface and how these affect the deposition processes.

In this work, the main concepts of microfluidics applied to the study of fouling in membrane processes were reviewed in detail, with particular attention to novel investigation techniques involving microfluidic devices. A microfluidic approach was then employed for the experimental studies. Firstly, the effects of different pumping systems on fouling dynamics of a Bovine Serum Albumin (BSA) solution were investigated by means of an originally microfluidic filtration

module characterized by a modular design. Fouling mitigation strategies were the main area of interest of the following part of the work. Specific attention was given to membrane functionalization techniques, such as antifouling coatings and nanostructure modification aimed to enhance membrane hydrophilicity and hinder foulants' deposition. Finally, given their potential as a possible solution to alleviate the issue of water sustainability, osmotic processes and the influence of process parameters on water recovery were studied.

Thesis Outline

The objective of this research work was to investigate membrane processes and the most relevant phenomena affecting separation, such as fouling, by designing a microfluidic approach.

This thesis has been structured into three chapters, each related to a specific area whose experimental work has been published, is under reviewing or writing. After a detailed introduction on fouling and the most relevant investigation techniques involving microfluidics, the first section is dedicated to the study of protein deposition during microfiltration operations. A miniaturized modular filtration cell was designed for this aim, characterized by the presence of multiple inlets/outlets, which allow the module to be operated equally in dead-end and crossflow filtration modes. In addition, an auxiliary current on the permeate side, e.g., a draw solution stream, may be added if needed. Specifically, a quantitative systematic investigation was carried out at constant pressure with three pumping systems, i.e., a peristaltic pump, a syringe pump and a pressure driven flow controller. A comprehensive view of the evolution of fouling was thus achieved by combining permeate flux, retentate and permeate concentration measurements with SEM micrographs, employed to study the structure of foulant deposits across the section of the processed membranes. Results show how, despite the similar process conditions, the pumping system plays a key role in foulants' deposition.

Fouling mitigation strategies are the topic of interest of the second section. Different antifouling coatings – namely polyethylene glycol (PEG) and tannic acid grafted on polydopamine – are reviewed and tested on both hydrophilic and hydrophobic membranes. Membrane's nanostructure modifications were then studied, with a deeper focus on membrane chemistry rather than on deposition phenomena. By considering as a target functionalization the growth of polyzwitterions – widely known for their antifouling properties – via surface initiated atom transfer radical (SI-ATRP) polymerization, a set of tunable, solvent

resistant, nanoporous membranes was developed, characterized by the presence of moieties that can serve as grafting sites for the SI-ATRP initiator. To do so, different statistical poly(trifluoroethyl methacrylate-co-oligo(ethylene glycol) methyl ether methacrylate-co-glycidyl methacrylate-co-hydroxyethyl methacrylate) (P(TFEMA-OEGMA-GMA-HEMA)) copolymers were synthesized by varying the relative amounts of GMA and HEMA and membranes were subsequently fabricated via nonsolvent induced phase separation (NIPS) methods.

The last section of the thesis is focused on forward osmosis processes, instead. In particular, the application of this process for water recovery is described. By employing the same microfluidic filtration module, several parameters, such as inlet flowrates, concentration difference and transmembrane pressure, were optimized to maximize water recovery. Concentration polarization phenomena were studied as well, due to their relevance in the presence of highly concentrated currents.

Chapter 1

Fouling Phenomena

Chapter Contents

1. Introduction

1.1. The Fouling Phenomena

Fouling is defined as the accumulation of undesired material at an interface, e.g., the contact region between a fluid and a solid [1]. Materials' deposition can cause a series of chemical and physical changes at the interface, leading to a loss in heat and mass transfer, as well as to a pressure buildup [2, 3]. This is a transient process, beginning as soon as fluid comes into contact with a surface, which eventually becomes so fouled that it completely loses its functionality. Fouling can be caused by a plethora of organic and inorganic species, commonly termed foulants, in the form of particulates, colloids, dissolved components and biological microorganisms [4-7].

A wide range of industrial and commercial applications relies on the processing of fluids prone to fouling. In heat exchangers, foulant deposition can take place on both the hot and cold sides of the apparatus, compromising the thermo-hydraulic performances of the system [8, 9]. In fact, the accumulation of substances such as organic matter contained in process currents (e.g., crude oil), or the debris in cooling water, act as an insulator, increasing the resistance to heat transfer. Moreover, the increasing thickness of the deposits over time leads to a reduction in the cross-sectional area with a consequential rise of the pressure drop. In 1972, Taborek et al. indicated fouling as the major unresolved problem in heat transfer, but its relevance is still very high because of its impact in terms of energy losses, fuel consumption and emissions [10, 11]. A similar influence of fouling on thermal and hydraulic resistances also takes place in steam cracking reactors, where the formation of coke on the inner wall of the tubular reactors represents the major reason of process inefficiency [12]. Indeed, due to fouling, systems need

to be periodically halted and decoked, procedures that negatively affect not only process economics but also the reactor lifetime [13].

However, among all the applications where fouling constitutes a technical challenge to process performances, membrane systems are the ones in which this phenomenon represents the most critical issue and limiting condition. As a matter of fact, membrane processes are based on the ability of a membrane to regulate the permeation rate of species through the pores, so that the accumulation of feed stream components is therefore almost unavoidable and triggers a rapid flux decline that lowers the process throughput [3, 14, 15]. Filtration processes are widely used in many industries including wastewater and effluent treatment, food processing, reusable and potable water production and in medical applications such as drug delivery and hemodiafiltration [16-24]. Membrane processes can be classified based on nominal pore size in conventional filtration (from 100 to 10 μm), microfiltration (MF) (from 10 to 0.1 μm), ultrafiltration (UF) (from 0.1 μm to ~50 Å), nanofiltration (NF) and reverse osmosis (RO) (both with a pore size down to ~1 Å) and each class is subject to fouling from different species as shown in Figure 1. MF and UF membranes, for example, are particularly suitable for bio-application since their pore sizes are comparable to the average cell or protein dimensions; NF and RO membranes, instead, can be fouled even by small molecules such as salts and ions, since pore diameter corresponds to the dimensions of voids randomly created by the thermal motion of polymer chains [25]. Owing to the wide variety of foulants affecting filtration processes and to the complex interactions involved, membrane fouling has gained a lot of scientific interest, with a large number of studies devoted to the identification of the mechanisms underlying the transient accumulation process [26-29].

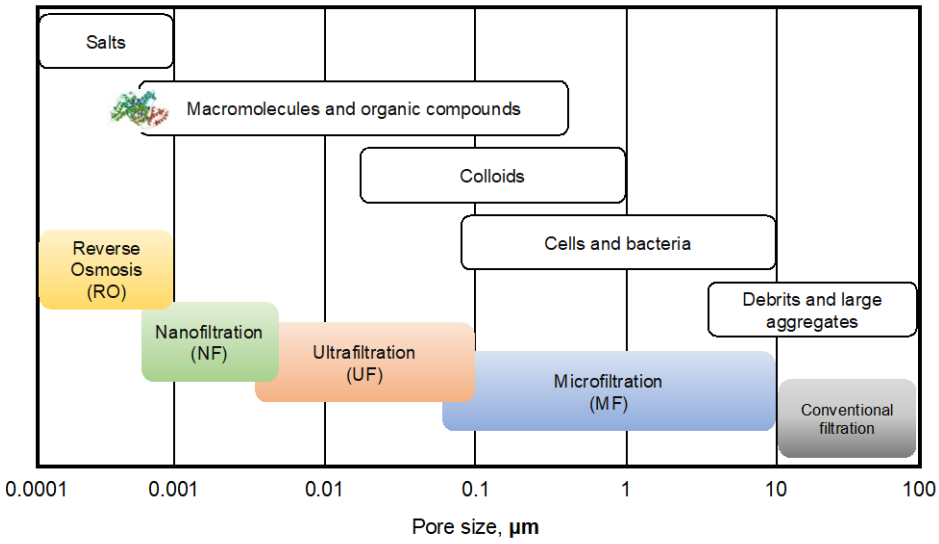

Figure 1. *Nominal pore size classification of membrane processes and characteristic dimensions of various common foulants. Despite the categorization, upper and lower size limits usually overlap between two adjacent processes due to pore size distributions. The figure also shows the most suitable process for each foulant category [30].*

According to Anis et al. [31], membrane fouling forms the third-largest research area in MF with over 600 papers published in the course of 10 years to the date of their work, and such a topic is still receiving attention thanks to the newest trends involving fouling mitigation through membrane modification and innovative investigation techniques aimed at studying the fouling phenomena at a microscopic level [32-35]. Indeed, the effects governing flux decline generally occur at quite small time and spatial scales, the latter corresponding to the dimension of the pores; studying fouling in micro-sized geometries would therefore allow achieving key insights regarding the interactions between foulants and membrane surface.

1.2. Microfluidic Membrane Devices

A technology of great potential for fouling investigation at the micro-scale is microfluidics. In its broadest definition, microfluidics is the science and technology of systems processing low amounts of fluids—between 10^{-18} and

10^{-9} L—in microchannels with typical dimensions down to micrometers [36, 37]. Microfluidics offers a large number of benefits [38]. The most important advantage of microfluidic systems is that the use of small fluid volumes allows reducing the consumption of reagents with a significant decrease in costs, safety risks and waste production, as well as other features including design flexibility, moderate chip cost and the possibility of coupling with microscopy techniques [39, 40].

To study membrane fouling, two microfluidic categories can be identified. The first one is also the simplest one, namely the membrane mimicking microfluidic devices (MMM). Such systems reproduce the pore structure of a membrane in an ideal way through parallel straight or constricted channels, round pillars, non-aligned squares or even complex 3D structures to account for higher pore tortuosity [41-45]. Membrane-mimicking devices allow the investigation of the fouling layer evolution in a single pore or in arrays of arbitrary complexity, yet the resolution of many modern fabrication techniques for microfluidic chips establishes a lower limit for pore dimensions and structure design [46]. The second category corresponds to the embedded membrane microfluidic devices; as the name says, these systems consist of chips specifically designed to house a small portion of the membrane [47-50]. As real membranes can be used, these devices overcome the drawbacks of the previous category, allowing the study of the fouling process at a level of complexity closer to reality; nevertheless, cross-sectional observation of the membrane can be more troublesome compared to MMMs. Embedded membrane microfluidic devices can potentially be useful also to assess the performances of the innovative membrane such as complex-shaped, biocompatible and reinforced ones, as microfluidic modules can be designed ad hoc for specific needs [40, 45, 51, 52].

Many reviews have examined the combination of microfluidics and membranes. A discussion on the application of microfluidic devices to investigate membrane

filtration and failure due to particles accumulation can be found in the work of Bouhid de Aguiar et al. [53]; on the other side, Debnath et al. have reviewed several device configurations involved in colloid filtration, whereas other studies focused on microchip fabrication techniques and the implementation of on-chip operations [54-56]. These works extensively discuss the advantages and limitations of micro-confined environments to study fouling dynamics, so the aim of this review is not to provide a comprehensive analysis of microfluidics applied to filtration processes, but rather to explore the fouling phenomena through microfluidic systems, assessing the fundamental interactions involved and how microfluidics enables a deeper comprehension of the complicate mechanisms governing the process. The principal mathematical models used to describe the various stages of the phenomena will then be briefly reviewed, in order to determine their advantages and limitations in the comprehension of the still debated aspects of fouling. Lastly, the most important dynamic investigation techniques in which microfluidics plays—or can potentially play—a key role will be discussed, analyzing their working principles and how they have been employed to study fouling.

2. Fouling: Stages and Interactions

The fouling process can be generally divided into three stages in series, as depicted in Figure 2: The pre-fouling stage, where foulants migrate from the bulk to the surface proximity; the membrane adsorption and blocking stage, during which pores are gradually clogged, and finally the gel/cake layer stage, in which the membrane is completely covered by foulants [2, 57, 58]. Each stage is characterized by interactions different in nature between the fouling agents themselves and with the membrane surface. In this section, the three fouling stages will be discussed, assessing the principal interactions involved and their effects in microfluidic systems.

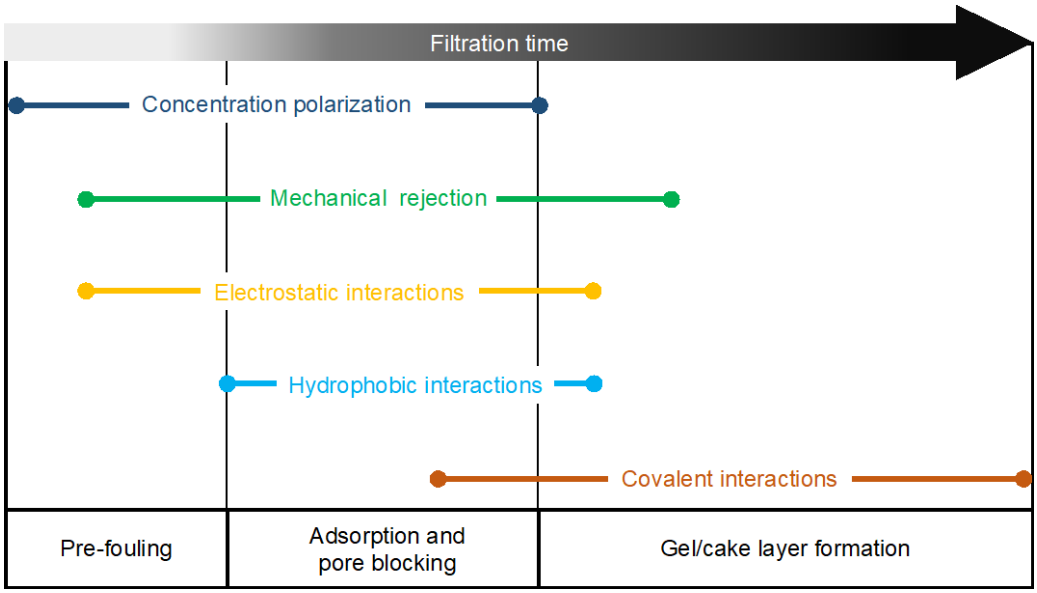

Figure 2. *Principal foulant–foulant and foulant–membrane interactions involved in the three stages of fouling [30].*

2.1. The Pre-Fouling Stage

The first stage of the fouling process is characterized by foulant migration towards the membrane surface, which starts being physically and chemically conditioned for the sequent stages. Owing to steric hindrance, there is a mechanical rejection

of the foulants by the membrane, which causes a rise in concentration near the surface, triggering the so-called concentration polarization phenomenon (CP) (Figure 3). The solutes buildup forms a thin film dominated by diffusive transport, the CP boundary layer, which generates a chemical potential gradient of opposite direction with respect to the permeate flow [25, 59]. As a consequence, a species back-flux and an increase in osmotic pressure are determined, with detrimental effects on mass transfer and selectivity. The onset of CP happens as the feed stream comes in contact with the membrane and continues during the whole filtration process, influencing the subsequent fouling stages. However, CP is not irreversible, since interrupting the feed or flowing a clean current would gradually eliminate the back-flux [4, 60, 61]. In the CP phenomenon, species migrating from the bulk interacts both with the membrane and with other foulants present in the boundary layer. When close to the membrane surface, particles and molecules are subject to long-range electrostatic interactions, which could be either attractive or repulsive according to the carried charges [62]. pH deeply affects the repulsive effects as it impacts on both the sign and number of charges of the functional groups of a molecule. For instance, in the case of proteins, a pH value far from the isoelectric point is responsible for a higher surface charge density, resulting in a strong repulsion from the membrane [63]. The ionic strength of the feed solution plays a role too, due to the possible adsorption of ions [64]. Electrostatic interactions are usually characterized by means of zeta potential measurements [63, 65]. When dealing with colloidal particles, foulant–foulant interactions affect the pre-fouling stage as well. Such long-range forces are either of electrodynamic or electrostatic origin and significantly impact the formation and permeability of the CP layer; colloidal particles are indeed subject to repulsive forces arising from the interaction of the electrical double layers surrounding them [66]. Depending on their diameter, particles in the boundary layer can also experience effects such

as Brownian or shear-induced diffusion and hydrodynamic lift forces that can help in retarding the onset of CP [67, 68].

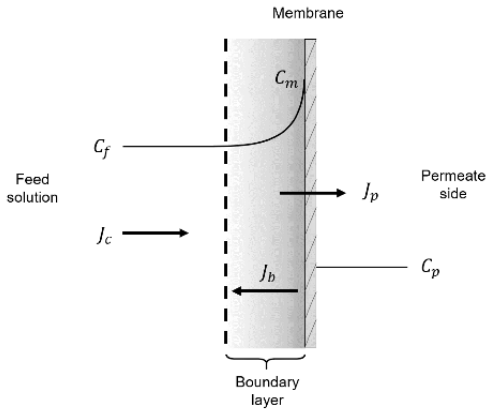

Figure 3. *Schematic representation of the concentration polarization phenomenon. C_f, C_m and C_p, respectively, represent foulant concentration in the feed bulk, at the membrane surface and in the permeate stream, whereas J_c, J_p and J_b indicate the convective flux toward the membrane, the permeate flux and the diffusive black flux determined by the concentration difference between the membrane surface and the feed bulk [30].*

From simulation studies, Wang et al. showed that nanometric particles are mostly affected by inter-particle interactions, while micrometric ones are predominantly influenced by hydrodynamic lift forces; on the other hand, for particles around 100 nm, none of these interactions plays a major role [69].

CP is ubiquitous in all the filtration processes, as it characterizes the first phases of fouling evolution, and its importance depends on the membrane separation process. Nevertheless, most studies have focused on the analysis of the long-term flux decline mechanism, where CP's importance becomes marginal [27, 70]. The role of CP in forward osmosis (FO) processes – a separation process which exploits a semi-permeable membrane to draw water from dissolved solutes – was investigated by Jiao et al., who characterized the development of the boundary layer using a PDMS embedded membrane microfluidic device [71]. Here, experiments were performed flowing the feed solution tangentially to the membrane surface, in the so-called crossflow operation mode (Figure 4) such

configuration is known to be beneficial for fouling prevention as it adds a shear mediated transport back to the feed bulk [72]. Using fluorescence microscopy, the authors were able to visualize the CP layer and monitor its thickness and permeate flux under various tangential flowrates. From the results, they concluded that CP mitigation becomes insignificant as the feed flowrate increases beyond a certain value.

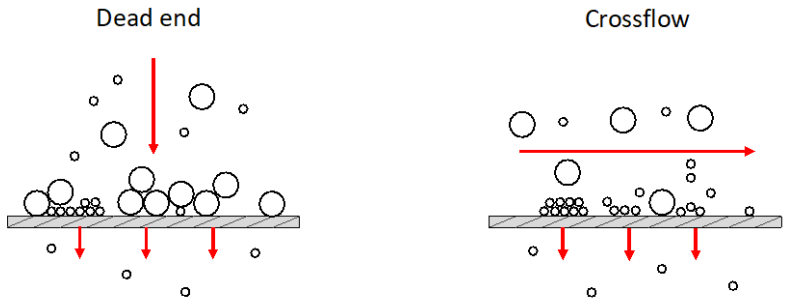

Figure 4. *Dead end and crossflow filtration modalities [30].*

Kaufman et al. explored the implementation of NF and RO processes in microfluidics, optimizing system design in order to contain CP [73]. Joining experimental results and CFD simulations they studied the role of the feed channel hydraulic diameter, showing that its decrease positively affects the mass transport coefficient, thus mitigating the CP phenomenon. The negative effects of CP on NF processes have also been studied by Completo et al., who showed the lower performances of a microfluidic crossflow NF device in comparison to a centrifugal NF system [74]. The optimization of the chip design for fouling mitigation represents a crucial challenge in microfluidic applications, since the flow in such systems is laminar, without any possible convective mixing [75]. Several studies have focused on the implementation of static elements inside microfluidic channels to induce mixing. Among all the different configurations, ribs and staggered herringbones geometries have been successfully used in the investigation of CP (Figure 5a,b) [60, 76].

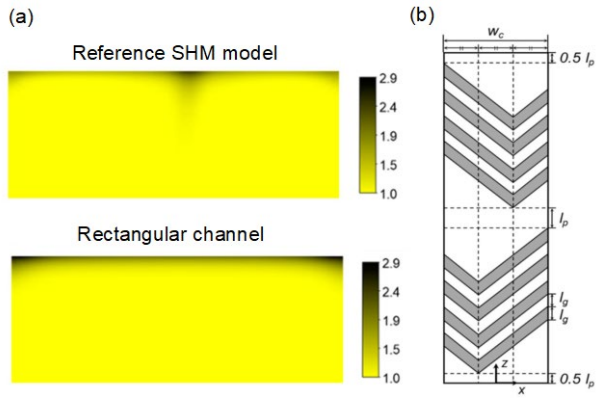

***Figure 5**. **(a)** Evolution of the concentration distribution in a staggered herringbone mixer (SHM) and in a plain rectangular channel with a permeating wall on top obtained by CFD simulations. Color contours represent the dimensionless concentration. The presence of herringbone-like grooves on the bottom of the microchannel determines the development of downwelling flows, which drag foulants downward reducing the development of the CP layer (dark region); **(b)** periodic unit of a staggered herringbone mixer. Adapted from [76].*

2.2. Membrane Adsorption and Pore Blocking

Adsorption and pore blocking define the second stage of the fouling process: Once foulants have traveled from the bulk solution through the CP layer, they come in contact with the membrane surface and the walls of its pores, where system evolution is governed by surface–foulant interactions [29]. With specific reference to the adsorption phenomena, this stage is usually termed "prompt fouling" and happens on very short time scales compared to the long-term flux decline imputable to the formation, growth and settling of a cake (or gel) layer [3]. In the industrial field, membrane performance are often characterized after the onset of prompt fouling; some membranes are indeed commercially useful only after it takes place [3, 77]. Nevertheless, it is principally a negative phenomenon.

Depending on the chemical nature of the species, covalent or non-covalent interactions can occur. Covalent bonds can take place between the functional groups on the foulant particles and the membrane surface; this type of adsorption if affected by the nature of the ligands and by the ion concentration in the feed

solution [4, 78]. The electrostatic forces, whose mechanisms have already been discussed in the previous section, constitute the first kind of non-covalent interactions that affect the adsorption and pore-blocking stage. In the presence of repulsive interactions, it is possible to individuate a critical flux, as defined by Howell [79], below which no deposition occurs since the drag forces are unable to overcome membrane-foulant repulsion. The first studies on the critical flux in MF and UF have been particularly useful for membrane plant operators, interested in maximizing the permeate flux while reducing cleaning operation frequency [61, 80, 81]. Recently, Lucas et al. applied microfluidic technologies to characterize the critical flux behavior of ultrathin nanoporous silicon nitride (NPN) membranes in crossflow filtration of concentrated protein solutions [82]. Results showed that the NPN membrane thickness played a key role in terms of fouling mitigation. Higher critical fluxes were indeed achievable thanks to the lower trans-membrane pressure required to achieve the desired fluxes, without leading to the formation of a compacted protein layer on the membrane surface. Van Zweiten et al. studied the effects of trans-membrane flux on clogging dynamics (e.g., the rate of pore blocking) by means of an MMM crossflow filtration device and a solution of polystyrene particles ($\bar{d}_p = 2.4$ μm) [83]. According to the authors, the lower clogging time at higher trans-membrane fluxes can be explained by the interplay of two opposing effects: The dependance of particle adsorption probability on its residence time in the pore and the higher viscous drag forces at higher fluxes, which push particles away.

Hydrophobic interactions constitute the second category of non-covalent interactions and involve van der Waals forces and Lewis acid–base interactions, which also include hydrogen bonding [57]. Membrane-foulant hydrophobic adsorption particularly affects the initial stages of fouling, and its dynamics can be explained considering hydrogen bonding. The presence of a hydrophobic surface in water disturbs the preexisting network of hydrogen bonds of water

molecules, increasing the free energy of the system; as a consequence, hydrophobic surfaces will be naturally pushed together so as to reduce the water-contacting interfacial area [84]. Membrane and foulant hydrophobicity is notoriously known to be one of the main contributors to fouling especially in protein solution processing [29, 85-88]. Using a microfluidic approach, Bacchin et al. showed how a small change in surface properties of a poly-dimethylsiloxane (PDMS) has drastic consequences on pore blocking and particle adsorption [42]. In hydrophobic conditions, particles formed arches at pore entrances, leading to the formation of a subsequent cake layer; on the other side, for hydrophilic PDMS, particles tended to settle on the walls between adjacent microchannels, forming dendritic structures without causing a severe pore blockage (Figure 6).

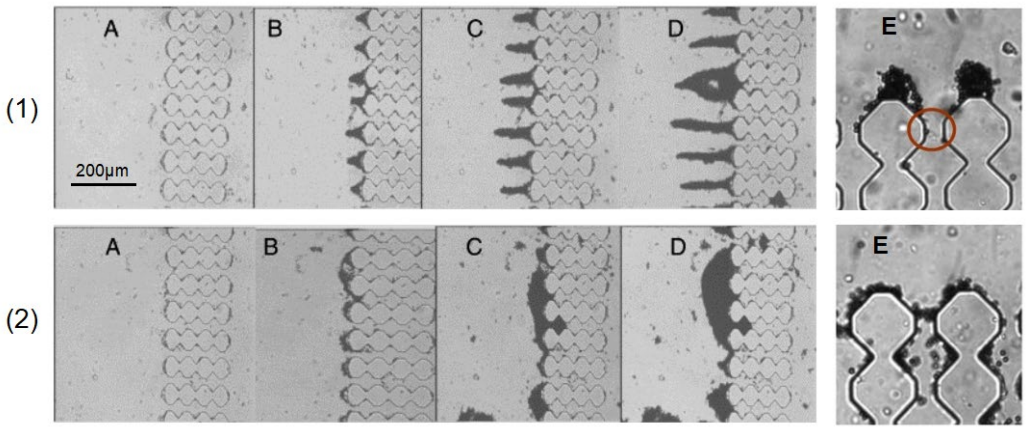

Figure 6. *Observation of pore clogging caused by particle deposition over time (from (**A**–**D**)). Two different behaviors can be identified based on PDMS surface properties. Row (**1**) shows pore blocking in hydrophilic conditions, where particles form dendrites at the pore entrances. Row (**2**) depicts clogging in hydrophobic conditions; here frequent particle collisions with the wall promote the formation of arches (onset E) and the subsequent formation of a cake layer. Adapted from [42].*

Membrane morphological characteristics, such as pore size and shape, tortuosity, connectivity and surface roughness, are relevant for this stage of fouling as well. Bacchin et al. studied the role of connectivity and tortuosity on pore blocking using a microfluidic separator. Experiments on filtration of mono-sized latex microspheres were performed using three microchannel geometries, namely an

array of straight parallel microchannels and two sets of square pillars, the former aligned on three rows, the latter staggered [44]. The feed solution was processed in dead end mode, that is flowing the feed current perpendicularly to the membrane surface [3].

In the most tortuous configuration (e.g., the staggered pillars), particle deposition occurred firstly in the internal spaces of the membrane resulting in a slow evolution of the fouling layers; for connected channels, an intermediate clogging was observed, as the initially captured particles modified the streamlines inside the channels eventually leading to internal blocking. The parallel channels configuration was the least performing, especially at higher velocities, where particles blocked pore entrances by forming arches. Similar dynamics were also observed in membrane experiments, yet not at the pore scale as in Bacchin's studies [89]. Microfluidics has also been adopted to investigate blocking behavior as a function of pore shape and size [90]. Massenburg et al. showed the positive effects of converging microchannels on the reduction of clogging times: The presence of a constriction induces higher fluid velocity and therefore higher shear rates, which prevent particles from attaching to channel walls [91]. As discussed, membrane morphology impacts adsorption and pore blocking dynamics; however, such phenomena, in turn, affect membrane structure, resulting in a detrimental feedback mechanism that eventually leads to the formation of a cake/gel layer. In fact, hydrophobic adsorbed foulants narrow pores, enhancing the mechanical capture of species and causing an acceleration in concentration build-up at the membrane surface.

2.3. The Gel/Cake Layer Formation

The final stage of the fouling process is characterized by the formation of a filter cake on the membrane surface, acting as a shield and thus providing an additional resistance to permeate flux. According to recent theories, the formation of a gel

layer happens as soon as the foulants concentration at the membrane surface reaches a critical value, namely the gel concentration, which marks a phase transition point [92, 93]. Indeed, below the gel concentration, the system behaves like a true solution, while above, it is characterized by an ordered phase having a cake type behavior [94]. Depending on water and foulant concentration, one can distinguish between the gel and cake layer; however, the two definitions often refer to the same species [27, 95, 96]. The gel/cake layer stage is also referred to as cumulative fouling because of its time-dependent nature: After the initial formation due to the high concentration at the membrane, the gel layer keeps growing, fed by the subsequently arriving species from the bulk. Moreover, under the effect of the feed stream, the cake can undergo compaction and structure reorganization, eventually decreasing permeate flux until a stationary value is reached [3].

This fouling stage is dominated by foulant–foulant cohesion, as species approaching the membrane will interact with the already deposited ones, contributing to the growth of the filter cake. In particular, covalent interactions are the main forces leading the gel layer formation. In filtration processes, common gelling foulants are organic substances, e.g., proteins, polysaccharides and humic acids, typically carrying carboxyl, hydroxyl and phosphoric groups, which can be subject to metal-organic complexation with multivalent ions such as calcium and magnesium [27, 57]. In this way, molecules in the gel matrix are crosslinked in a three-dimensional network and the fouling layer reaches macroscopic electro-neutrality [97]. Despite its lower thickness and higher porosity compared to a cake layer formed by particles or sludge flocks, the gel layer presents a contradictory high specific resistance; however, explanations of this behavior are still debated [27, 97]. As regards non-covalent interactions, their effects principally influence the layer's structure in terms of porosity, compactness and permeability. In a recent study, Mokrane et al. investigated the

microstructure of the cake layer formed upon the filtration of a colloidal suspension in an MMM device consisting of an array of parallel straight microchannels [98]. Apparently, changes in ionic strength and pressure did not affect the global porosity of the cake layer; nonetheless, a local study revealed heterogeneity in the clog's structure. Cake porosity was indeed higher nearby the pore entrances, while it was lower far away; furthermore, higher ion concentration in the suspension resulted in smaller colloidal crystals and in more organized structures. These findings allowed the authors to develop a phase diagram concerning foulant–foulant repulsive interactions and hydrodynamic forces. The effects of the latter on the cake growth were also studied by Ngene et al., who developed a filtration microfluidic device, shown in Figure 7, that allowed for side observation of the cake layer formation on the membrane [50].

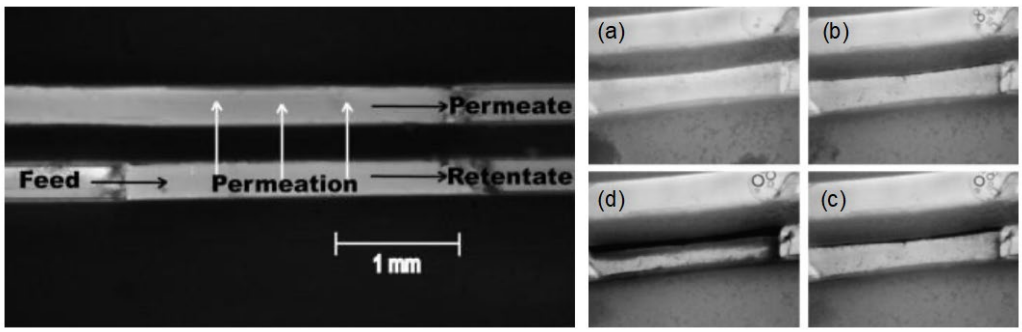

Figure 7*. On the left, a microfluidic filtration device allowing side observation of the membrane developed by Ngene et al. Pictures on the right show the temporal evolution (from* ***a*** *to* ***d****) of the cake layer, which can be clearly distinguished in* ***(d)****. Adapted from [50].*

Foulant–foulant interactions play an important role also in systems containing both organic and inorganic foulants, such as proteins and silica nanoparticles, which can have a synergic effect on cake formation [99]. The dynamics of the cake/gel layer stage are also influenced by particle deformability and compressibility. In fact, even if larger than the pore, soft particles are able to pass through the membrane by deforming and deswelling. Such foulants are common in several industrial applications, e.g., wastewater treatment and emulsion

filtration [100, 101]. The behavior of a soft microgel in a microfluidic filtration system and in a centrifugation one was investigated by de Aguiar et al. [102]. While at low pressure, pores were blocked immediately, microgel particles were more prone to deformation at higher pressures, clogging pores deeper in the structure of the model membrane.

The cake deformation recovery process was assessed via centrifugation experiments, which allowed an irreversible compression impossible to reach in filtration tests. Pore geometry was shown to play a role in cake formation, too. In cases of soft particle filtration, it is important to note that pore size and membrane cut-off are not reliable parameters when it comes to process efficiency evaluation; indeed, further factors such as particle mechanical properties have to be taken into account.

2.4. Biofouling

The unwanted deposition and growth of microorganisms on surfaces characterize the so-called biofouling phenomenon [103]. This process generally follows a series of stages, schematically represented in Figure 8, which shares some similarities with the already discussed ones. Indeed, biofouling usually starts with a conditioning phase where organic foulants accumulate and adsorb on the membrane surface; once microorganisms have attached to the membrane, however, colonies can form and proliferate, eventually forming a mature layer that can be detached by the shear forces the feed flow exerts [104].

Microorganism colonization of a surface is actually a complex process, in which various phenomena take place at different time and length scales; the interactions of bacteria, fungi or algae with the membrane causes the formation of a complex matrix, which hosts microorganisms and is made of nutrients and biological waste products, the extracellular polymeric substances (EPS), that are very prone to gelling [105]. This constitutes a major issue during cleaning procedures. The

common response to biofouling is disinfections, which consists of killing the microorganisms that, however, may still remain attached to the membrane, becoming a nutrient supply for the survived ones [106]. In this way, the exponential proliferation would restore the colony in very short times, resulting in useless disinfection. It is therefore necessary to ensure the complete removal of the biofilm by overcoming the adhesive and cohesive forces—i.e., hydrophobic interactions, hydrogen bonding, entanglements—which bind it to the membrane surface and are provided by di EPS. The most common removal procedures involve hydraulic and pneumatic cleaning [106].

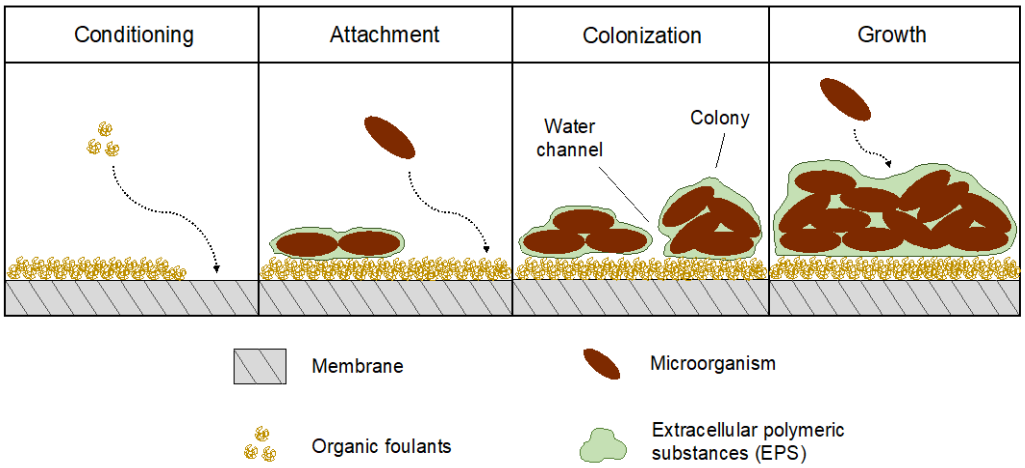

Figure 8. *Schematic representation of biofouling evolution stages [30].*

Biofilm formation is affected by several biological factors, including cell physiology, mechanical properties and physicochemical factors, such as hydrodynamic conditions and membrane morphology [32, 105]. These elements impact the film structure, leading to uncommon fouling phenomena such as the formation of filamentous structures, termed streamers, downstream of the membrane pores [107]. Microfluidics has been proven to be a useful tool for the investigation of bacterial streamers in membrane filtration. Marty et al. investigated the formation of streamers and the effect of pore size and structure,

filtration mode and flowrate on the filtration of an *Escherichia coli* suspension in an MMM device [108]. The streamer formation process is characterized by three steps. Initially, tiny filaments start to adhere to the channel entrances without interfering with bacterial accumulation; after approximately 1 hour, multiple filaments interact to form a network that captures more cells, eventually forming larger bacterial streamers. This process is deeply affected by pore tortuosity, rather than connectivity. In fact, of the three geometries used by the authors, the staggered pillars one exhibited the most severe filament formation, due to the numerous changes in flow directions. These microfluidic configurations were the same as in the work of Bacchin et al. [44], discussed in Section 2.2. *Membrane adsorption and pore blocking*. In addition, streamer build-up was enhanced by smaller pores and lower flowrates; on the other side, crossflow filtration mode appeared to promote streamer formation, although at different magnitudes depending on the pore structure.

3. Fouling Mathematical Modeling

The evolution of fouling during a filtration process is typically monitored by means of techniques that rely on the measurement of parameters such as averaged permeate flux, solute rejection and pressure drop across the filtration cell. In order to assess the various stages of the phenomena, various mathematical models have been proposed to analyze data in both dead-end and crossflow filtration modes. Specific equations have been developed for constant pressure and constant flux, the former being characterized by a flux decrease over time due to fouling, whilst in the latter, an increase in pressure can be observed. In this section, different mathematical models for membrane fouling interpretation will be reviewed briefly, with particular attention to constant pressure filtration.

3.1. Resistance-in-Series Model

The resistance-in-series model derives from Darcy's law and is based on the concept of total resistance, which includes contributions from the intrinsic membrane resistance and from the resistance generated by fouling development [109]. Assuming constant pressure and applying Darcy's law [110]:

$$J = \frac{\Delta p}{\eta\, R_{tot}} \tag{1}$$

where J is the permeate flux ($m^3 m^{-2} s^{-1}$), Δp is the transmembrane pressure (Pa), η is the viscosity of the permeate (Pa s) and R_{tot} is the total resistance (m^{-1}). R_{tot} can also be expressed as the sum of three contributions, namely R_m, R_r and R_{ir}:

$$J = \frac{\Delta p}{\eta\, (R_m + R_r + R_{ir})} \tag{2}$$

where R_m is the hydraulic resistance of the clean membrane, while the other two terms respectively represent the resistance caused by reversible phenomena such

as CP (R_r) and the one caused by irreversible phenomena, e.g., adsorption and permanent external or internal pore blockage (R_{ir}). R_m can be calculated by performing pure water flux experiments (i.e., in absence of foulants); to calculate R_{ir}, a second pure water flux experiment must be performed after carefully rinsing the membrane subsequently to the filtration of the desired feed. A second pure water flux (J'_w) can thus be measured and R_{ir} calculated as follows:

$$R_{ir} = \frac{\Delta p}{\eta_w J'_w} - R_m \qquad \textbf{(3)}$$

indicating with η_w the viscosity of pure water. R_r can be finally evaluated by subtracting the irreversible and membrane resistances to the total resistance. Equations (1) – (3) can be used without further modification for both dead end and crossflow filtration mode.

By evaluating the separate terms contributing to R_{tot}, the resistance-in-series model allows one to study which terms play a key role in the flux decline, giving useful information about whether a filtration process is controlled by reversible or irreversible fouling and thus which cleaning mechanism could be the most appropriate for fouling mitigation [111]. Moreover, from the concavity of R_{tot} as a function of time, it is possible to distinguish between external and internal fouling, or rather if the adhesion of foulants takes place on the membrane surface (downward concavity) or within the pores (upward concavity) [112, 113]. Nevertheless, the resistance-in-series model does not provide specific information about the fouling mechanisms. Indeed, from the evaluation of $R_{tot}(t)$ it is only possible to tell where the foulants are settling, yet how their deposition happens (e.g., complete blocking of the pore entrance or cake formation) is not fully known.

3.2. Blocking Filtration Laws and Cake Filtration Model

The blocking filtration laws and the cake filtration model represent a very useful tool for the interpretation of the physical mechanism governing the blockage of pores over time. The model takes into account the dependence of the filtration behavior on the ratio of the particle size to the pore opening one and consists of four different fouling mechanisms: Complete blocking, standard blocking, intermediate blocking and cake filtration, as represented in Figure 9 [114].

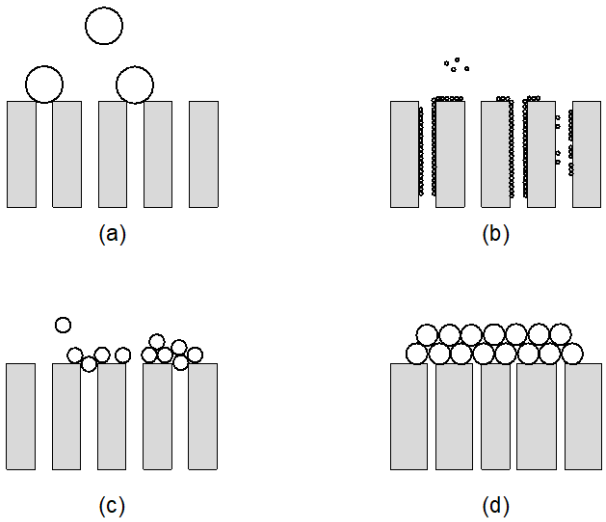

Figure 9. *Hermia's pore blocking models illustration:* ***(a)*** *Complete blocking;* ***(b)*** *standard blocking;* ***(c)*** *intermediate blocking;* ***(d)*** *cake filtration.*

The filtration laws were first proposed by Hermans and Bredée for constant pressure filtration and subsequently reanalyzed by Grace and Hermia, who condensed the laws for the four mechanisms into a single differential equation by adjusting two parameters characteristic of the specific fouling behavior [115-117]:

$$\frac{d^2t}{dv^2} = K_{DE}\left(\frac{dt}{dv}\right)^n \qquad \textbf{(4)}$$

where t is the time (s) and v is the filtrate volume (m^3). K_{DE} and n are constants related to the fouling behavior, the former's physical meaning and the latter's value depends on the mechanism. Equation (4) can also be expressed in terms of flux $J = dv/dt$ [114]:

$$\frac{dJ}{dt} = -K_{DE} J(J)^{2-n} \quad \textbf{(5)}$$

A further development of Equations (4) and (5)—which can only be used for constant pressure dead end filtration—was made by Field et al., who adapted Hermia's blocking filtration laws to constant pressure crossflow filtration by adding a term that represents convective removal:

$$-\frac{dJ}{dt} = K_{CF}\,(J - J^*)\,J^{2-n} \quad \textbf{(6)}$$

where J^* can be considered as a critical flux that should not be exceeded in order to avoid fouling and is usually assumed as the steady-state flux value ($J(t \to \infty)$), while K_{CF} and n are the parameters correlated to each model [109, 111]. Table 1 summarizes the model equations for constant-pressure dead-end and crossflow filtration.

The complete blocking model is characterized by $n = 2$ and is based on the assumption that, considering a membrane with parallel pores of constant diameter and length, each foulant particle arriving at its surface completely seals the entrance of an open pore without depositing over other particles. The permeate flux through unblocked pores is thus unaffected and its reduction over time is equal to the decrease in membrane area available for filtration; as a matter of fact, the parameter K_{CPB} represents the membrane surface blocked per unit of total volume permeated and unit of initial membrane surface porosity [112, 118]. This fouling behavior is typical of systems involving particles whose size is bigger than the pore diameter.

Differently from the complete blocking model, where particle deposition occurs on the membrane surface, the standard blocking model considers the deposition and adsorption of foulants inside the membrane pores due to the irregularity of pore passages. As a consequence, pore diameter decreases proportionally to the permeate volume. Foulants smaller than the pore size are the main responsible of this fouling mechanism, which is described by $n = 3/2$ and its constant K_{SPB} represents to the volume of solid retained per unit of filtrate volume, membrane thickness and inverse surface porosity [118]. It is worth noting that, as fouling takes place on the inside of the pores, in crossflow filtration, flux reduction does not depend on the crossflow velocity and the steady-state permeate flux $J(t \to \infty)$ is zero [119]. The equation describing this model for dead-end and crossflow filtration is therefore the same [112].

According to the intermediate blocking model ($n = 1$), pores are not necessarily blocked by one particle, and the probability that the settlement takes place on an already deposited particle must be taken into consideration; consequently, during filtration, the clean membrane surface diminishes along with the probability of a particle blocking a pore [81]. This model well describes systems where the foulant size is similar to the pore size and, therefore, pore entrances are obstructed but not completely blocked. The physical meaning of the parameter K_{IPB} is similar to the one characterizing the complete blocking model.

Because of its assumptions, the cake filtration model is usually considered apart from the previously described models, which are categorized as pore blocking models. Indeed, in cake filtration, foulants deposit on the membrane surface without entering the pores and a filter cake grows throughout the filtration process adding additional resistance to the permeate flow [114]. In the cake filtration model, $n = 0$ and the constant K_{CLF} is related to both the characteristics of the cake and those of the clean membrane [81].

Table 1. *Membrane fouling models for constant-pressure dead-end and crossflow filtration.*

Filtration Model	n	Dead End [112, 114]	Crossflow [109, 118]
Complete blocking	2	$J(t) = J_0 \exp(-K_{CPB} t)$	$J(t) = J^* + (J_0 - J^*)\, e^{-J_0 K_{CPB} t}$
Standard blocking	3/2	$J(t) = \frac{J_0}{\left(K_{SPB}\, {J_0}^{1/2} t + 1\right)^2}$	$J(t) = \frac{J_0}{\left(K_{SPB}\, {J_0}^{1/2} t + 1\right)^2}$
Intermediate blocking	1	$J(t) = \frac{J_0}{(K_{IPB}\, J_0 t + 1)}$	$J(t) = \frac{J_0\, J^*\, e^{K_{IPB}\, J^* t}}{J^* + J_0 (e^{K_{IPB}\, J^* t} - 1)}$
Cake filtration	0	$J(t) = \frac{J_0}{\left(1 + 2K_{CLF}\, {J_0}^2 t\right)^{1/2}}$	$t = \frac{1}{K_{CLF}\, J^{*2}} \ln\left[\left(\frac{J(t)}{J_0}\frac{J_0 - J^*}{J(t) - J^*}\right) - J^*\left(\frac{1}{J(t)} - \frac{1}{J_0}\right)\right]$

3.3. Combined Models

To understand the fouling mechanisms that interest a filtration process, permeate flux data as a function of time are usually inferred using only one of the discussed blocking filtration laws or cake filtration model for the entire range of data [26, 43]. Although such a procedure can lead to good interpretation, it typically represents the main disadvantage of the presented models. Indeed, fouling is a three-stage process (i.e., pre-fouling, pore blocking and cake formation stages) in which complex mechanisms take place, caused by the presence of particles of different sizes, which might interact with both the membrane and other particles. Moreover, real membranes usually present a pore size distribution and a complex morphology far from that of the parallel straight cylinders structure assumed by the models. A succession of pore blocking mechanisms hence occurs, where transitions between consecutive stages are gradual and happen over small time intervals [112]. Consequently, data fitting can be affected to the point that none of the mechanisms is able to properly explain the flux reduction due to fouling [112]; for this reason, combined models were developed when multiple mechanisms dominate the evolution of fouling.

An approach to data interpretation considering multiple fouling mechanisms is that of inferring the whole set of flux data over time with each one of Hermia's models (single-stage Hermia's model) and analyzing which one gives the best fit for a specified time interval. Such a procedure was adopted by Brião et al. to evaluate the fouling behavior of ultrafiltration membranes, where the resistance-in-series model was also used to understand where the fouling happened preferentially [109]. A similar methodology was implemented by Choobar et al., who used a multistage Hermia model capable of giving information about the dominant mechanism at different times by only fitting a certain interval with the most appropriate mechanism [26]. The general equation of such a model is Equation (7):

$$J_{Multistage\ model} = a\,J_{CPB} + bJ_{IPB} + cJ_{CLF} \quad \textbf{(7)}$$

where a, b, c are factors varying with operating conditions (e.g., TMP and crossflow velocity) while J_{CPB}, J_{IPB} and J_{CLF} are, respectively, the permeate flux connected to the complete blocking, the intermediate blocking and the cake filtration. The proposed model was obtained by first inferring the flux data with a single-stage Hermia's model, which revealed that standard blocking had the lowest overall fitting accuracy and was therefore discarded in the multistage model. The single-stage model-fitting procedure also allowed to identify the dominant mechanism at different times, useful for the subsequent application of the multistage model.

Ho and Zydney developed a combined model for protein fouling, which accounts for both initial pore blocking and subsequent cake layer growth by providing a smooth transition between the two mechanisms without the need for multiple mathematical expressions [120]. The model was derived for dead-end constant-pressure filtration and considers the volumetric flowrate permeating the membrane to be equal to the sum of two flowrates, the former related to open

pores while the latter to the blocked ones. The filtrate flowrate at any given time is hence calculated as follows:

$$Q(t) = Q_0 \left[\exp\left(-\frac{\alpha \Delta p C_b}{\eta R_m} t\right) + \int_0^t \frac{\alpha \Delta p C_b}{\eta (R_m + R_p)} \exp\left(-\frac{\alpha \Delta p C_b}{\eta R_m} t_p\right) dt_p \right] \quad \textbf{(8)}$$

where Q and Q_0 respectively are the volumetric flowrates ($m^3 s^{-1}$) at a given time t and the initial volumetric flowrate through the clean membrane, Δp is the transmembrane pressure (Pa), α is a pore blockage parameter ($m^2\ kg^{-1}$) related to the mass of an aggregate blocking a given area of the membrane, C_b is the bulk concentration ($g\ l^{-1}$), t_p is the time at which a particular region is first blocked by a protein aggregate (s), R_m is the resistance of the clean membrane (m^{-1}) and R_p is the resistance of the protein deposit (m^{-1}) given by Equation (9):

$$R_p = \left(R_m + R_{p0}\right) \sqrt{1 + \frac{2 f' R' \Delta p C_b}{\eta \left(R_m + R_{p0}\right)^2} \left(t - t_p\right)} - R_m \quad \textbf{(9)}$$

where R_{p0} is the resistance associated with a single protein aggregate (m^{-1}), R' is the specific protein layer resistance (m^{-1}) and f' is the fraction of proteins that contribute to the growth of the deposit. The smooth transition between the initial fouling stage and the cake formation provided by the model derives from the assumption that settled aggregates allow a small amount of fluid to flow through pores, with the hydraulic resistance of the fouled areas of the membrane increasing in time because of the proteins transported to the surface. The model thus considers the spatial inhomogeneity of the protein layer, with the firstly fouled regions of the membrane opposing higher resistance to the permeate flow.

A set of five models accounting for the combined effect of different fouling mechanisms was proposed by Bolton et al., instead [121]. The authors derived the

model equations from Darcy's law for both constant pressure and constant flow dead end filtration. The most effective model among the proposed ones is the complete blocking–cake filtration one (Figure 10a), which assumes that cake formation and complete pore blockage happen simultaneously and independently. Here the cake forms on unblocked membrane areas whereas complete blocking can occur where the cake has previously formed.

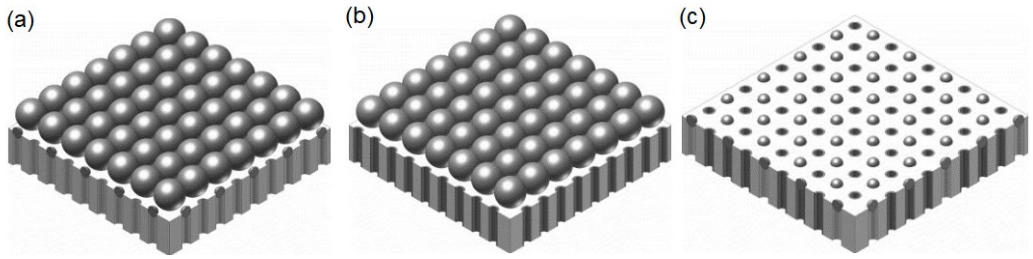

***Figure 10**. Bolton's combined models: **(a)** Cake filtration—complete blocking; **(b)** cake filtration—standard blocking; **(c)** complete blocking—standard blocking. Adapted from [121].*

Therefore, flux reduction is caused by a decrease in the area available for filtration due to complete blocking or by an increase in resistance related to cake growth. The assumptions of this model make it suitable in the presence of distinct foulant species, for example large particles settling on the membrane surface and smaller ones permeating through the cake and blocking membrane pores. In practice, however, the two mechanisms are usually connected as blocked pores could lead to the buildup of a cake; on the other side, an already formed cake layer could prevent a subsequent pore blockage. In the combined cake filtration–standard blocking model (Figure 10b), the available filtration area does not decline over time, as pores are fouled on the inside rather than blocked at the entrance. This model can be useful in the presence of particles smaller than the pore size and much larger ones, as the former will penetrate inside the pores whereas the latter will settle on the membrane surface constituting an additional hydraulic resistance (i.e., cake resistance). As for the complete blocking–cake filtration model, although the two mechanisms are supposed to act independently, they can actually

influence one another. Indeed, the presence of a cake could prevent small particles from permeating inside the pores, while constricted pores could enhance particle deposition on the membrane surface. The other three models involve the combination of intermediate blocking with cake filtration or standard blocking and that of complete with standard blocking. As pointed out by the authors, the five models are less physically detailed than the combined model proposed by Ho and Zydney and their use for the estimation of physical parameters is limited; however, the reduced numerical complexity make them easier to implement [120, 121]. A complete overview of the models' equations in terms of permeate volume as a function of time for constant pressure filtration can be found in Table 2.

More recently, Bolton's complete blocking–cake filtration model was improved by Hou et al. [122]. The authors proposed a new combined model, which considers an initial time interval where complete blocking and cake filtration acted together, followed by a long-term flux decline related to the dominance of the latter. A steady frontal membrane area K (m^2) was introduced, representing the available membrane frontal area left when the fouling mechanism switches from combined complete blocking–cake filtration to individual cake filtration. Moreover, the transition point between the two mechanisms was determined under various process conditions. According to this model, flux decrease as a function of time is expressed by Equation (10):

$$J = \frac{J_0\left((1-K)\exp\left(\frac{-K_b}{K_c{J_0}^2}\left(\left(1+2K_c{J_0}^2t\right)^{1/2}-1\right)\right)+K\right)}{\left(1+2K_c{J_0}^2t\right)^{1/2}} \quad \textbf{(10)}$$

where J_0 is the initial permeate flux ($\mathrm{m^3 m^{-2} s^{-1}}$) while K_b and K_c are the complete blocking ($\mathrm{h^{-1}}$) and cake filtration constant ($\mathrm{h\,m^{-2}}$) of Bolton's combined model.

Table 2. *Bolton's combined models in terms of $V = f(t)$ for constant pressure filtration.*

Filtration Model	Component Mechanisms	Equation
Cake—complete	Cake filtration, complete blocking	$V(t)= \frac{J_0}{K_{CPB}}\left(1-\exp\left(\frac{-K_{CPB}}{K_{CLF}{J_0}^2}\left(\sqrt{1+2K_{CLF}{J_0}^2 t}-1\right)\right)\right)$
Cake—intermediate	Cake filtration, intermediate blocking	$V(t)= \frac{1}{K_{IPB}} ln\left(1+\frac{K_{IPB}}{K_{CLF}J_0}\left(\left(1+2K_{CLF}{J_0}^2 t\right)^{\frac{1}{2}}-1\right)\right)$
Complete—standard	Complete blocking, standard blocking	$V(t)=\frac{J_0}{K_{CPB}}\left(1-\exp\left(\frac{-2K_{CPB}t}{2+K_{SPB}J_0 t}\right)\right)$
Intermediate—standard	Intermediate blocking, standard blocking	$V(t)=\frac{1}{K_{IPB}} ln\left(1+\frac{2K_{IPB}J_0 t}{2+K_{SPB}J_0 t}\right)$
Cake—standard	Cake filtration, standard blocking	$V(t)=\frac{2}{K_{SPB}}\left(\beta\cos\left(\frac{2\pi}{3}-\frac{1}{3}arccos(\alpha)\right)+\frac{1}{3}\right)$, $\alpha=\frac{8}{27\beta^3}+\frac{4K_{SPB}}{3\beta^3 K_{CLF}J_0}-\frac{4{K_{SPB}}^2 t}{3\beta^3 K_{CLF}}$, $\beta=\sqrt{\frac{4}{9}+\frac{4K_{SPB}}{3K_{CLF}J_0}+\frac{2{K_{SPB}}^2 t}{3K_{CLF}}}$

4. Dynamic Investigation Techniques

As previously discussed, fouling evolution is usually monitored through flux and pressure measurements. Despite the fact that mathematical modeling represents a useful approach to characterize the various fouling mechanisms, such parameters only enable an indirect evaluation of all the complex phenomena happening at the microscale, and few pieces of evidence are provided on foulant concentration and distribution over the membrane. In addition, CP and cake compression can affect both permeate flux and transmembrane pressure (TMP), resulting in possible data miscomprehension. The time resolution of conventional methods represents a drawback too: CP layer development, adsorption and pore blocking are indeed very fast processes whose characteristics may not be fully elucidated by simple gravimetric experiments and pressure readings.

It is therefore challenging to assess each stage of the fouling phenomena with such approaches, and new process-oriented methodologies are currently being explored [123]. Specifically, in situ real-time monitoring techniques are very powerful tools to investigate the dynamic development of fouling. In a recent paper, Rudolph et al. reviewed several of such techniques available for the

monitoring of membrane fouling in the biotechnology, biorefinery and food sectors, enlightening their strengths and weaknesses [124]. Applications of in situ techniques to CP monitoring were instead reviewed by Chen, Li and Elimelech [92]. A deeper comprehension of the microscopic events involved in the evolution of fouling has been enabled by the coupling of in situ dynamic monitoring techniques with microfluidics. As a matter of fact, the micro-confined environments provided by the latter allow one to observe phenomena such as pore occlusion and cake growth with high spatial resolution. In the next section, different investigation techniques in which microfluidics represents a potentially valuable tool for the study of the fouling phenomena will be reviewed.

4.1. Direct Microscopic Observation

Direct in situ observation (DO) of foulant deposition on the membrane surface and inside the pores constitutes a simple, non-invasive and low-cost technique for membrane fouling monitoring. DO can be generally classified into two categories: Direct visual observation (DVO) and direct observation through the membrane (DOTM) (Figure 11) [123, 124].

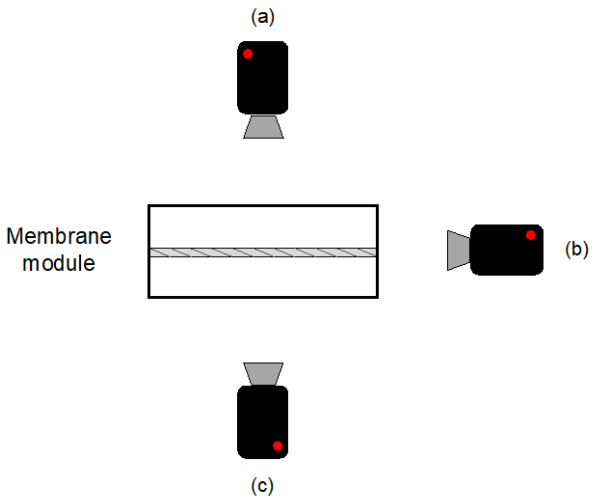

Figure 11. *Schematic of direct visual observation:* ***(a)*** *DOSM;* ***(b)*** *DVO from side view;* ***(c)*** *DOTM.*

In the former, the membrane is observed from above its surface on the feed side, allowing the visualization of fouling as far as the feed current is transparent enough for light to pass; DVO is also known as direct observation of the surface of the membrane (DOSM) and can be performed even observing the membrane from a side view, enabling cake layer thickness measurements and observation of the inside of the pores [125]. On the other side, DOTM are only possible if membranes are transparent under process conditions and are limited to the monitoring of the first stages of the process, after which the formation of an opaque layer of foulants impedes any observation [50].

The use of microscopy as support for DO enables the visualization of the events involved in the fouling phenomena that take place at the microscopic scale. In such a way, it is possible to determine foulant deposition dynamics as well as deposit morphology and how these are affected by process parameters (i.e., TMP, feed flowrate, membrane properties); this information can be thus related to flux and pressure data, allowing a detailed comprehension of the fouling mechanisms. Among the various microscopy techniques, light-microscopy finds extensive usage for in situ real-time DO owing to its versatility [123]. In particular, among the many types of light-based techniques, the coupling of microfluidics with bright-field microscopy, fluorescence microscopy and confocal laser scanning microscopy (CLSM) represents the most used and effective methodologies to investigate the fouling phenomena.

4.1.1. Bright-Field Microscopy

Bright-field microscopy is the most common imaging technique in light microscopy [126]. Modern bright-field microscopes are compound microscopes using multiple lenses systems to form a dark image on a bright background. Indeed, in such apparatus the illuminating beam is a solid cone of light provided by an illuminator located below or above the stage (respectively in upright or

inverted microscopes) and focused on the specimen by a condenser lens to maximize illumination. The final image is produced by the consecutive magnifications of the objective lenses (placed near the specimen) and the ocular and can be viewed directly or captured via a digital camera (e.g., digital video microscopy) [127]. Especially for fouling investigations, high-speed cameras constitute an essential tool to monitor the phenomena happening at very short times, such as foulants deposition and pore clogging [128, 129].

The coupling of bright-field digital video microscopy and microfluidic systems was successfully used by Wyss et al. to study the clogging mechanisms at a single-pore level [130]. In their work, a microfluidic PDMS device consisting of a single wide channel followed by an array of parallel, narrow channels, was employed to analyze the clogging events due to the flow of polystyrene particle suspensions (Figure 12). An additional degree of tortuosity was added by a set of constrictions along the length of each channel. Particle concentration was monitored through image intensity; in fact, the presence of darker regions corresponded to higher particle concentrations and the packing degree of the clogs. Results indicated that neither the feed flowrate nor the particle volume fraction influences the clog formation, which exclusively depends on a critical number of particles flowing through the pore. Moreover, the authors presented a model that accounts for the scaling of such critical particle numbers with the ratio of the pore to particle size. Similar findings were obtained by Dersoir et al., who studied the effects of pore geometry, confinement, hydrodynamic conditions and ionic strength of the solution on the formation of a clog in a single pore [131].

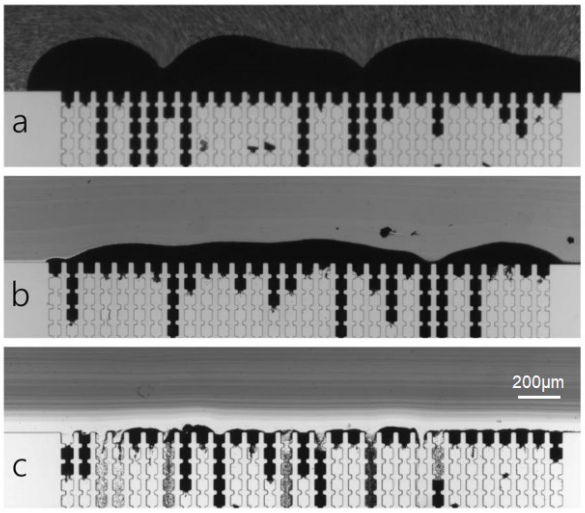

Figure 12. *Cake layer formation during* ***(a)*** *dead-end and crossflow filtration at* $0.219\ mL/min$ *and* $0.395\ mL/min$ ***(b,c)****. Figures clearly show how particle deposition is influenced by the filtration mode. Black regions indicate the presence of a higher particle concentration. Adapted from [83].*

However, it appeared impossible to determine the exact clog position and dimensions through bright-field images, as the particle density was too high. Bright-field microscopy has several drawbacks indeed, among which its maximum resolution of about 0.2 µm, which limits its application to micron-sized or smaller foulants [123, 126].

Many of the works involving the pairing of bright-field microscopy and microfluidics to study the fouling phenomena make use of MMM devices, which, for construction reasons, allow real-time direct observation of the process from a side view [42, 44, 83, 91, 130-132]. An application of DO from above can be found in the work of Warkiani et al., who developed a microfluidic embedded membrane device to study the fouling mechanism of micron-sized particles in isopore filters at a macroscopic level [133].

4.1.3. Fluorescence Microscopy

According to IUPAC, fluorescence is the emission of light that intersects particular substances after the absorption of light or other electromagnetic

radiation [134]. The key property that makes fluorescence such a powerful tool for visual investigations resides in the so-called Stokes shift, that is, the difference between the emitting and exciting radiation wavelengths, the former being generally higher than the latter. Indeed, blocking the exciting light by means of an optic filter, it is possible to observe fluorescent objects on a dark background with very high contrast. Molecules that undergo fluorescence are called fluorophores and are characterized by a small energy difference between their ground and excited state orbitals, so that even low-energy photons can be used to excite the electrons in the outermost orbitals. Although many natural substances (e.g., chlorophyll) are intrinsically fluorescent, synthetic compounds are usually preferred for labeling because of their better performances [126].

Most of the modern fluorescence microscopes rely on an epi-illumination mode, in which microscope objectives not only image and magnify the specimen, but also act as condensers that focus the light illuminating it. As the paths of the exciting and the emitted lights overlap, such microscopes make use of dichroic mirrors to separate the two. Such filters are engineered to transmit longer wavelengths, belonging to the emission spectra, while reflecting the shorter ones that characterize the excitation light. Dichroics are commonly used with two additional filters, the excitation and the barrier ones, which respectively narrow the exciting wavelengths and the ones belonging to the light going from the sample to the detector. As for bright-field ones, fluorescence microscopes can be supported by a digital camera, which besides the previously described advantages, allows better visualization of dimmed images thanks to the possibility of adjusting the exposure time of the sensor [126].

Real-time observations through fluorescence microscopy were performed by Neeves et al., who monitored platelet aggregation in a membrane-based microfluidic device designed to control the flux of platelet agonists into flowing blood [135]. Time-lapse fluorescence video microscopy was instead used by

Dehghani et al. to study pore blocking and adsorption dynamics in a microfluidic device, aimed at the isolation of species such as extracellular vesicles from biological fluids through the so-called tangential flow for analyte capture method (TFAC) [136]. Employing fluorescent particles as model target species to be separated, the authors assessed the efficiency of each stage the TFAC method, namely capturing by crossflow filtration, cleaning with a buffer and releasing via backflushing, for both micro and nanoporous track-etched membranes. Particle deposition in each stage was indeed examined by measuring fluorescence intensity over time (Figure 13).

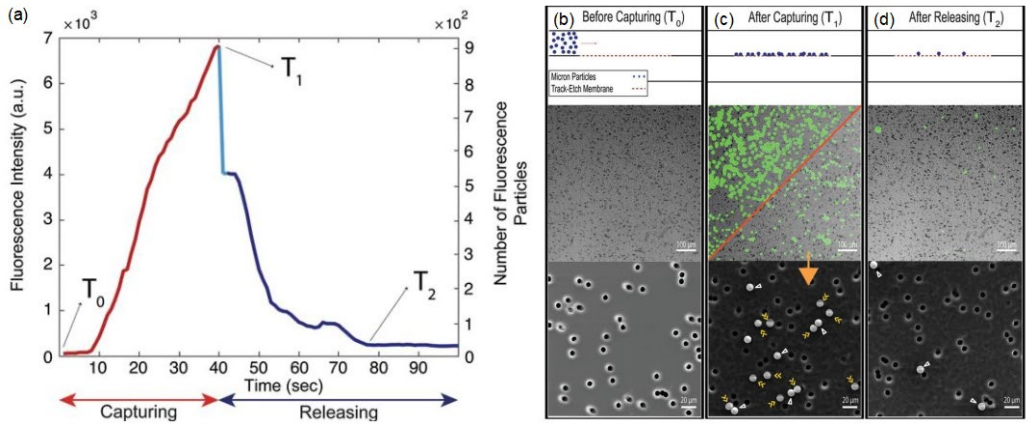

Figure 13. *Results from the microscale experiment carried out by Dehghani et al. on microporous track-etched membranes:* ***(a)*** *Fluorescence intensity and the number of particles against time plot, showing an increase in the intensity signal and the number of particles during the capturing step and a decrease during the releasing one;* ***(b–d)*** *TFAC process stages including fluorescence microscopy images (middle) and SEM images (bottom). Adapted from [136].*

Fluorescence microscopy was demonstrated to be a helpful tool in the investigation of fouling and sorption mechanisms of proteins. Due to their small dimensions, biological macromolecules such as proteins are indeed impossible to observe through bright-field microscopy, whereas with the help of fluorescent labeling, their clusters and even single molecules can be observed or at least their position and concentration on the membrane surface determined [123]. In recent work, Bacchin et al. combined fluorescence and permeability measurements to

study the fouling mechanisms and the adsorption kinetics of bovine serum albumin (BSA) and α-lactalbumin (LALBA) [137].

The real-time in situ observations and flux measurements were allowed by a membrane embedded microfluidic device. Monitoring the changes in fluorescence signal from the retentate side of the membrane surface during filtration showed good agreement between signal and permeate flux values over time. Indeed, the same regimes were observed: The initial flux drop corresponded to a sharp increase in fluorescent signal, while during a second period, a slower flux decline matched with moderate signal variations, eventually reaching steady values. Signal intensity is also correlated to protein concentration, therefore allowing its direct evaluation, useful for sorption kinetic modeling.

Fluorescence tracking during LALBA filtration pointed out one of the main limitations of such microscopy technique, quenching, which is a reversible loss of fluorescence due to noncovalent interactions between a fluorophore and its molecular milieu [138]. As a matter of fact, differently from BSA, LALBA can adopt alternative conformation and remain in a stable, partially denatured state, which can be induced both by flow conditions (e.g., flowrate and TMP) and membrane pore size [139, 140]. The principal drawback of fluorescence microscopy is the bleaching phenomenon. Although, theoretically, fluorophores can be cyclically excited infinite times, their usage is generally limited due to the progressive permanent fade of fluorescent signal. There are several strategies to reduce bleaching. First of all, it is important to keep samples in the dark when not in use and to utilize just the right amount of light needed for observations; moreover, high-quality optical filters can decrease bleaching by providing an efficient passage of the emitted wavelengths. As previously mentioned in Section *2.1. The Pre-Fouling Stage*, fluorescence microscopy also represents a useful method to investigate concentration polarization [71]. The presence of fluorescent

components, indeed, allows the visualization of the concentration gradient across the retentate side, otherwise impossible with bright-field microscopy.

4.1.3. Confocal Laser Scanning Microscopy

Confocal laser scanning microscopy (CLSM) is an optical imaging technique, which allows a high-quality visualization of a three-dimensional specimen at different depths, with better axial resolution and contrast compared to conventional light microscopy techniques. Its performances are accomplished by actively suppressing out-of-focus light thanks to the use of point illumination, provided by lasers, and pinholes [141].

Although, in theory, confocal microscopes can be used for any type of microscopy, their most common application is for fluorescence microscopy [126]. Indeed, in confocal fluorescence microscopes, both excitation and emission light coming from out-of-focus planes is largely blocked respectively by the illumination and the detector pinhole, avoiding image blurring and enhancing contrast with the dark background. Hence, images taken with CLSMs appear as thin optical sections, generating the so-called "optical sectioning" effect. The position of the planes in which the pinholes and the specimen are located is what relates such a microscopy technique to the term confocal, as they all are conjugate planes; consequently, the image of the illumination pinhole is in focus at both the specimen plane and the detector one. It is important to note that, differently from the previously described microscopy techniques, image acquisition in confocal microscopes happens in series, as only a single point in the object is illuminated, and a scan of the specimen is required to obtain a complete image [142]. Laser scanning characterizes CLSM, which is the most used method for confocal microscopy [126, 142].

Besides the higher resolution and contrast, CLSM has the advantage of enabling a 3D reconstruction of the specimen by combining images taken at different axial

levels with the help of dedicated software. This represents a key aspect for the study of the fouling phenomena as, even observing the membrane from above, it is possible to reconstruct the fouling layers and analyze their structure. This feature was exploited by Di et al. for the dynamic visualization and quantification of latex particles deposition in a microfluidic filtration system specifically designed for CLSM coupling (Figure 14a) [143]. From 2D images, it was possible to observe that varying salt concentration in the particle suspension affected the initial stages of the deposition process with a higher presence of large aggregates at higher KCl concentrations. On the other side, 3D images clearly showed that particles formed a monolayer independently of the KCl concentration of the solution, suggesting that the growth of the aggregates happened parallel to the membrane surface rather than perpendicularly. In a subsequent study, the same microfluidic filtration setup was used for a detailed study on the dependance of particle fouling from pH, ionic strength and salt concentration in the feed. Once again, the combination of 2D and 3D images allowed to distinguish between different fouling dynamics, e.g., the preferential formation of aggregates at lower pH, that are directly correlated to particle–particle and particle–membrane interactions (Figure 14a). Together with fluorescence microscopy, CLSM can also take advantage of the use of different fluorophores to better investigate fouling dynamics in presence of more foulant species. This helped Marty et al., in their already mentioned work, to distinguish the presence of EPS all around the bacteria forming streamers and conclude that such structures were indeed formed by the contribution of both the foulants [108]. Multiple stains were also used by Mukherjee et al. to study the influence of EPS on biofouling in FO (Figure 14b) [144].

Specifically, the authors developed a CLSM-compatible membrane-embedded microfluidic flow cell to investigate biofouling nondestructively and showed that,

despite the long-term biofilm dispersal, permeate flux did not increase due to the presence of EPS, which irreversibly blocked membrane pores.

Nevertheless, CLSM has some drawbacks too. First of all, the scanning process can represent a problem for dynamic observations. In fact, the first stages of the fouling phenomenon occur within very short times, which may not be sufficient for the microscope to acquire an image. Moreover, the tangential flux of fluorescent foulants over the membrane can result in blurred and noisy images, if the concentration is too high. The objectives' working distance can be an issue as well, although microfluidic systems can usually be visualized with common commercial confocal objectives.

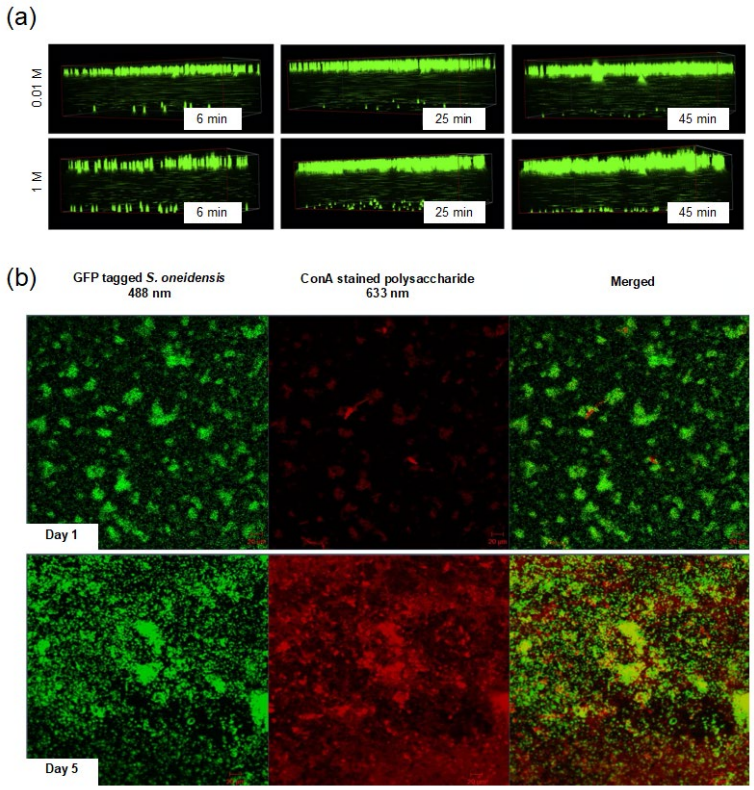

Figure 14. *(**a**) Three-dimensional CLSM images of the microfluidic filtration device developed by Di et al. at different filtration times. Experiments were performed at two different KCl concentrations to account for the effects of ionic strength on the fouling process. Channel depth* 25 ± 2 *μm. (**b**) CLSM images of multiple stained samples: GFP-tagged S. oneidensis cells (green) and ConA-stained extracellular polysaccharides (red) on a FO membrane after 1 and 5 days of processing. Adapted from [143, 144].*

4.2. Optical Coherence Tomography

Optical coherence tomography (OCT) is an interferometric technique that enables 3D visualization of inhomogeneous samples, such as a fouled membrane, through the progressive acquisition of high-resolution cross-sectional images [145, 146]. It is a non-invasive technology based on light interference where a near-infrared light beam is split to follow two different paths. The former travels axially through the sample and is partially reflected every time there is a change in the refractive index, e.g., in the presence of a cake layer on the membrane surface. The other beam crosses the so-called reference arm, which is equipped with a mirror and whose length is precisely determined. Due to reflections caused by the specimen's heterogeneity, the sample beam travels a path of different length compared to the reference one, therefore generating a series of interferences when the two are combined. The associated variations in light intensity are measured by a detector and the resulting interferograms are processed to obtain a final 2D image. It is important to note that in order for interference to be observed, light has to be coherent, or rather the phase difference between the waves of two beams has to be constant. OCT makes use of broadband low-coherence light, for which phase differences remain constant only within a short length usually in the order of micrometers [146].

In its early development, the cross-sectional scan of the specimen was performed modulating the reference arm length for each depth by moving the reference mirror. In this mode, called time-domain OCT (TD-OCT), 2D images are acquired by scanning the sample point-by-point first alongside its depth (A-Scan) and then moving laterally across the width of its section (B-Scan). 3D images can be obtained by the composition of several B-Scans. TD-OCT has currently been replaced by Fourier domain OCT (FD-OCT), characterized by the absence of moving parts. In FD-OCT, the intensity signal is recorded as a function of

frequency, rather than distance, and A-Scans are then computed via Fourier transformation; in doing so, a single scan provides information about the whole depth of the sample, resulting in a higher imaging speed [147]. Compared to CLSM, in which samples are optically sectioned too, OCT has a higher penetration depth owing to the long-wavelength light sources [148, 149]. However its spatial resolution is very limited, and due to the absence of any stain, it is impossible to distinguish between different species, making such a technique not suitable to investigate the interplay of multiple foulants at once [147].

OCT is an already-established technique in the biomedical field, where it is used for tissue diagnosis when a biopsy is not applicable and represents a high-potential technique for in situ real-time monitoring of the fouling phenomena thanks to the possibility of monitoring foulant accumulation, distribution and morphology. FD-OCT application to biofouling monitoring is very common since such methodology allows one to investigate biofilm formation in situ over long times and without stressing the microorganisms. Park et al. used OCT to monitor biofouling in an RO filtration cell over 50 days, clearly observing the various stages characterizing such phenomena [150]. Specifically, 2D images showed no changes in the membrane surface for the first 11 days, during which the conditioning stage was taking place. Due to colonization and growth, a considerable increase in the thickness of the biofilm was instead observed from day 20 to 35, after which no increases were recorded, implying an equilibrium between the rate of growth and detachment. The authors also underline the importance of a 3D representation, as the use of single 2D cross-sectional images for biovolume quantification is highly affected by uncertainty.

Biofilm development was also investigated by Quian et al., who developed a tortuous microfluidic device to study the role of biofouling in irrigation devices, and by Weiss et al., who used Doppler optical coherence tomography (DOCT) to monitor local hydrodynamics in a single microfluidic channel [151, 152]. DOCT

exploits the Doppler effect—i.e., the frequency shift experienced by the waves reflected from a moving object—and allows quantitative imaging of fluid flow, thus giving supporting information to the structural ones provided by FD-OCT, without the need of additional independent measurements [145]. In such a way, it was possible to directly observe the dynamic deformation of the biofilm surface due to the shear stresses exerted by the fluid [152]. OCT and DOCT were also used by Gao et al. to study the formation of a cake layer of bentonite particles during a FO process and the influence of a membrane spacer on the fouling layer growth [153].

4.3. Nuclear Magnetic Resonance Imaging

Nuclear magnetic resonance (NMR) imaging—also known as magnetic resonance imaging (MRI)—is a non-invasive investigation technique that takes advantage of the intrinsic magnetic properties of protons in atomic nuclei and allows to access the membrane module inner structure even in cases of opaque or non-transparent units [154-157]. In an NMR experiment, the sample is firstly placed in a static magnetic field that triggers the magnetization of the specimen protons to align with or against the direction of the field, depending on the energy level. Indeed, due to their magnetic moment, atomic nuclei behave similarly to microscopic bar magnets, which, in the absence of any external magnetic field, are randomly oriented. The excitation step is thus realized by means of a second external oscillating magnetic field generated by radiofrequency coils; such a field is meant to provide an exact quantum of energy to induce an energy level transition in the protons, i.e., the spin flip. In the subsequent relaxation step, as soon as the oscillating field is shut off, protons spontaneously return in their equilibrium state, releasing the previously absorbed energy and thus emitting a signal, which can be recorded and translated to create spectra or images representing variations within the sample.

One of the most important concepts on which NMR imaging relies is nuclear shielding [154]. Atoms in the specimen are surrounded by electron clouds, which orbit the nuclei influencing the magnetic field experienced by the latter; changes in the chemical environment of the atom affects the energy level of the nucleus resulting in different radio frequency required during the excitation step. Owing to nuclear shielding, NMR not only enables a structural characterization of the sample, but also a chemical one. Moreover, through the use of gradient coils, which linearly vary the applied magnetic field, NMR can also provide information regarding the local position and velocity in flowing samples, such as feed and permeate currents in a membrane module [158]. As showed by Wiese et al., this information is of crucial importance especially for the design of efficient membrane filtration modules [159]. With the help of MRI, the authors investigated the flow field and the development of a fouling layer made of colloidal silica in a commercial sterile membrane filter (Figure 15a). Quantifying the local flux distribution and visualizing particle deposition over time, it was possible to correlate the evolution of fouling to the feed flow and evaluate the active membrane area inside the module, thus showing all the critical design aspects affecting filtration performances.

Despite the latest technological advances regarding NMR systems, the application of this technique to microfluidics still represents a challenge. Conventional MRI spatial resolution is indeed limited by an inherent low signal-to-noise ratio, which is further aggravated by the small fluid volumes typical of microfluidic devices. This leads to very low-intensity signals hardly detectable even with high-field magnets and optimized radio frequency circuits [160]. Several works have focused on the implementation of novel approaches aimed at improving MRI resolution for microfluidic applications. McDonnel et al. and Paulsen et al. enhanced MRI sensitivity using remote detection, that is, physically separating the signal detection from the other steps of the experiment [161-163]; a nominal

isotropic spatial resolution of 2.8 μm was instead obtained for the first time by Chen and Tycko, who exploited low temperatures (28 K) where NMR signals are boosted by factors such as lower thermal noise [160].

NMR imaging was demonstrated to be a powerful technique to study the fouling phenomena in hollow fiber membranes, commercially available with diameters down to 100 μm [75]. Via NMR imaging, Çulfaz et al. investigated the influence of particle dimension on the evolution of fouling in a single hollow fiber, observing that while larger particles formed a highly concentrated cake layer on the membrane surface, smaller ones produced a thicker yet less-concentrated CP layer, resulting in lower resistance against permeate flux, compared to the previous case [164]. In the work of Arndt et al., MRI enabled the in situ observation of fouling development due to alginate deposition and the influence of Ca^{2+} on this process [165]. Namely, in the absence of ions, it was possible to observe an unstructured CP layer, which resulted in lower NRM intensity areas. MRI also allowed to study the effect of fouling on the flow distribution inside the feed channel of the membrane, obtaining 2D, spatially resolved velocity profiles at the center of the membrane lumen by saturation stripes (Figure 15b). Due to the diameter, the hollow fiber membranes examined in these studies can be more appropriately classified as millifluidic, rather than microfluidic; however, they represent an important step for the implementation of NMR imaging to investigate the fouling phenomena in microfluidic systems.

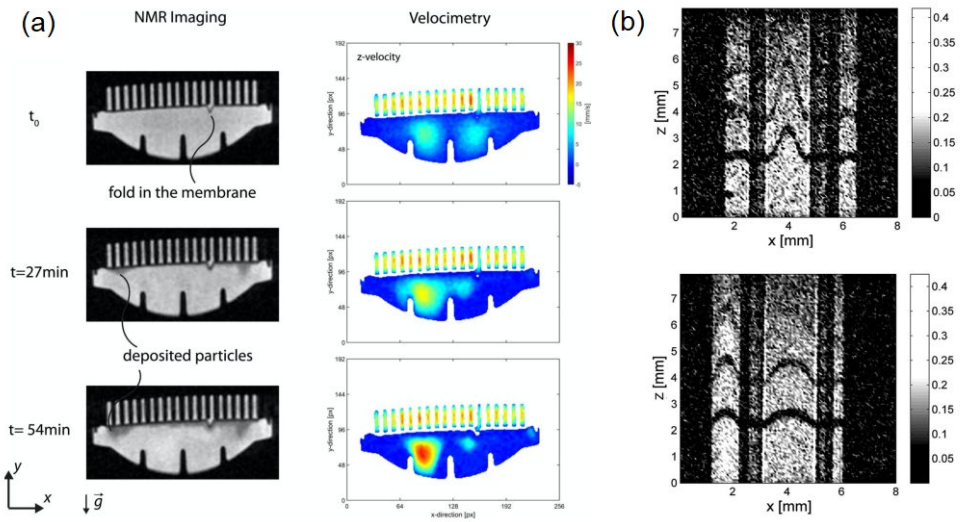

Figure 15. *(**a**) MRI and flow-MRI of the commercial filtration module investigated by Wiese et al. NMR imaging clearly shows the presence of a cake layer after 54 min of filtration (darker areas). (**b**) MRI saturation stripes indicating axial velocity inside and outside a single hollow fiber membrane. Images show the effects of the absence (top) and presence (bottom) of Ca^{2+} ions on fouling development due to alginate deposition after 22 and 21 min [159, 165].*

4.4. Other Emerging Techniques

In the previously described approaches, microfluidics represented an essential tool to study fouling at the microscale. Nevertheless, there are many other techniques suitable for the dynamic investigation of such phenomena, which have been implemented for microfluidic applications and are currently adopted on a macroscopic level, yet scarce or no application can be found regarding their use to study fouling in microfluidic systems.

4.4.1. Raman Spectroscopy

Raman spectroscopy (RS) is a vibrational spectroscopy method that allows one to obtain the chemical fingerprint of material by assessing vibrations and rotations of the functional groups of its molecules. Such a technique can thus be used to characterize different species with a high detection sensitivity, making it especially suitable for the investigation of the early stages of fouling [166-168]. The key principle of RS is the Raman shift, that is, the change in wavelength of a

photon scattered by a molecule in the sample. Indeed, in RS, the specimen is shined with a laser of a definite wavelength, whose light will mostly be scattered without any wavelength change, i.e., elastically (Rayleigh scattering); only 1 in 10^5–10^7 photons will be subject to inelastic scattering (Raman scattering), experiencing the Raman shift characteristic of the molecules the light interacts with [169].

The reduced number of photons undergoing inelastic scattering constitutes the main drawback of Raman spectroscopy; in fact, the weak intensity of the Raman scattering makes it difficult to distinguish the Raman peaks from the background noise generated by the environment surrounding the sample. Signal intensity can be enhanced by modifying the surface of interest with metallic nanoparticles as in surface-enhanced Raman spectroscopy (SERS) [170], the most common technique used to study membrane fouling [124]. Thanks to the confined environment provided by chips and capillaries, microfluidics represents a high-potential tool to overcome the main limitations of SERS applied to membrane filtration, namely the probability of detachment of nanoparticles due to high cross-flow velocity and the disturbances generated by high pressures and vibration in a macroscopic membrane module [171]. The immobilization of nanoparticles, however, can also affect membrane performances as particles might act as foulants, blocking or narrowing pores.

To the best of our knowledge, there are not any studies concerning the application of RS to study fouling in microfluidic devices; however, some researchers have recently exploited the advantages of membrane separation to further improve molecular detection via RS. A microfluidic implementation of SERS was proposed by Chang et al., who developed a detection device equipped with a membrane whose purpose was to concentrate a bacterial suspension and separate metabolites for the subsequent SERS aimed to the determination of antibiotic susceptibility [172]. In another study, Krafft et al. set up a microfluidic chip

equipped with a membrane, which fulfilled two functions at the same time, namely enriching the liquid sample and hosting the nanoparticles necessary for the SERS detection [173].

4.4.2. Fourier Transform Infrared Spectroscopy

Fourier transform infrared (FT-IR) spectroscopy is an absorption-based spectroscopy technique in which a sample is exposed to infrared radiation (IR), whose absorption results in an increase of the vibrational and rotational energy of the sample molecules [174]. FT-IR spectroscopy makes use of an interferometer to scan all the frequencies in the IR region generated by the source and Fourier transform is used to convert the interferogram from the time domain to the frequency one. Each species converts the absorbed radiation in a unique way, thus FT-IR spectroscopy is able to identify and characterize the composition of a material with high specificity [175].

Compared to other investigation techniques such as fluorescence microscopy, FT-IR spectroscopy does not need any labeling agent, which makes it suitable especially in the study of biofouling, as the addition of a fluorophore might potentially affect system physiology [176]. In addition, differently from RS, FT-IR spectroscopy is characterized by higher signal yields relative to the incident power. The application of FT-IR spectroscopy to real-time monitoring of fouling in filtration devices is nonetheless limited by the interference arising from the broad O-H vibration bands of water. A strategy to overcome such a problem can be the use of microfluidics [177]. Indeed, the low volumes processed in microfluidic chips allow one to obtain a very thin layer of water between the sample and the path of the incident radiation, thus containing the detrimental effects of water absorption. Holman et al. combined FT-IR spectroscopy with open channel microfluidics to study biofilm growth in different geometries and monitor the biochemical response of the system over time [178]. With such a

system, it was possible to correlate the growth dynamics to the presence of the principal components of the EPS.

In order to be used for FT-IR spectroscopy, microfluidic devices have to be made of IR transparent materials, which can be expensive and hard to craft compared to glass and polymeric materials such as PDMS or polycarbonate. Chan et al. proposed a versatile approach for the prototyping of reusable microfluidic devices compatible with FT-IR spectroscopy [179]. Device manufacturing consisted of the printing of wax on the surface of an IR transparent substrate, followed by the positioning of a second layer to generate closed channels of desired thickness. This methodology was subsequently exploited for live imaging of single cells [180].

4.4.3. Ellipsometry

Ellipsometry is a spectroscopy technique based on light polarization commonly employed to characterize materials surfaces. In an ellipsometry measurement, a monochromatic light beam illuminates the surface of the specimen with equal parallel and perpendicular polarization components; due to the interaction with the surface, reflected light is elliptically polarized. The signal detected from a photodetector is subsequently processed and compared to a specific mathematical model, whose selection depends on the expected numbers of layers within the sample itself. This constitutes a limiting factor especially when dealing with complex and heterogeneous materials such as fouled membranes [181]. Among the information one could gather using ellipsometry (e.g., surface roughness, crystalline nature, electrical conductivity, refractive index), this optical technique is particularly effective in the real-time investigation of adsorption processes on various surfaces and its most popular application involves the thickness measurements of films and layers, with a definition down to the nanometer scale [181, 182].

The number of studies involving ellipsometry to investigate the fouling phenomena in microfluidics is limited. However, the coupling of this technique and confined environments could have a positive impact especially on the study of the early stages of fouling. Indeed, these phases are characterized by adsorption reactions at the liquid–solid interface between the feed and the membrane, whose investigation requires small volumes in order to minimize light dispersion [183, 184]. Huber et al. exploited ellipsometry to investigate the performances of a polymeric coating capable of adsorbing or releasing proteins as a function of temperature [185]. Although adsorption/release tests were performed in a microfluidic chip equipped with several micro heaters, the thickness of the protein layer was only measured ex situ. Another application of ellipsometry for antifouling coatings can be found in the work of Peterson et al., who studied PDMS biocompatibility, proving how the adsorption of proteins such as fibrinogen can hinder coating antifouling effects, allowing the proliferation of cell colonies during incubation experiments [186]. The design of a microfluidic optical cell for in situ ellipsometry was proposed by Kondoh et al., who significantly reduced the cell volume, compared to typical trapezoidal flow cells, by using a commercial glass slide functioning as a cover for the fluid space and a transparent window for measurements [183].

4.4.4. X-ray Microimaging

X-ray microimaging (XMI) is a non-invasive in situ imaging technique, which relies on the penetration of high-energy electromagnetic radiation into a material, whose refractive index influences both the amplitude and the phase of the x-rays [203]. Aided by synchrotron radiation, XMI can reach spatial resolutions up to 1 μm, thus having the potential to provide quantitative data in terms of pore blocking, cake thickness and also membrane morphology, since it allows to investigate membrane's inner structure. In addition, 3D reconstructions of a sample can be performed [204].

The first application of XMI to membrane processes observation was proposed by Yeo et al. [205]. Using such an imaging technique, the authors were able to study iron hydroxide particles deposition both inside the pores and on the lumen surface of a single hollow fiber of 600 µm inner diameter (Figure 16). In addition, images evidenced the presence of air bubbles, proving the possible application of XMI to the identification of two phases phenomena [206]. In a recent study, XMI was applied to directly visualize water droplet spreading and penetration inside a membrane in an oily environment [207].

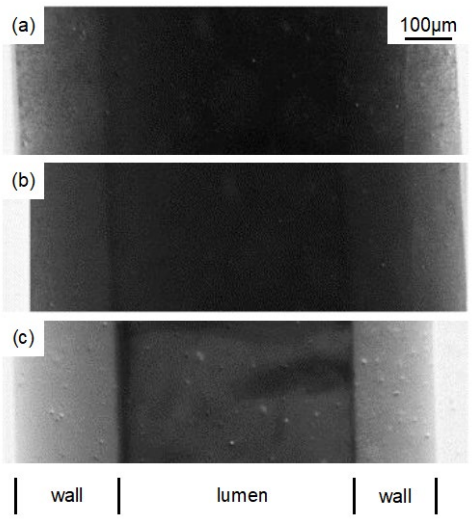

Figure 16. *XMI of a membrane fiber during progressive deposition of ferric hydroxide on the lumen wall after* ***(a)*** *0 min,* ***(b)*** *5 min and* ***(c)*** *30 min of operation. The absorptive contrast on the wall gradually increases as the deposition becomes thicker. Adapted from [187].*

Despite being a powerful investigation technique for fouling investigation, the application of XMI to microfluidic systems is mainly related to the field of flow measurements and velocimetry [188-190].

5. Experimental Study on the Effect of Pumping Systems on Fouling Evolution

A consequence of the complex nature of fouling is that a multitude of factors may impact on its evolution, along with feed solution chemistry and foulant nature or morphology. Firstly, fouling is affected by the way the feed solution laps the membrane. Filtration operations can be performed in dead-end (DE) or crossflow (CF) modes; in the former, the feed solution is flowed normally to the membrane surface, therefore the whole volume is filtered at the end of the process. On the other hand, in crossflow operations, the feed current flows tangentially to the membrane surface, thus determining the presence of two outlet streams, i.e., the permeate and the retentate, the inlet fraction which has not flowed through the membrane. Depending on the need to optimize productivity rather than operational costs one can choose the most suitable mode [164]. CF is often used for heavily fouling feeds, as the tangential flow generates lift forces which mitigate solute deposition, whereas the more economic DE filtration is very common for low fouling potential solutions as in such mode the retained particles constantly accumulate on the membrane surface. The effect of filtration modality on the properties of the cake layer were examined by Xu-Jiang et al., who related its higher observed porosity and compressibility in CF microfiltration experiments to the formation process of the cake itself [191]. Indeed, in DE filtration all the filtered particles approach the membrane surface normally, whereas the characteristic acute impact angle of CF mode leads to the formation of an open and more permeable deposit. Moreover, the shear forces exerted on the cake surface in CF filtration influences the deposited particle size distribution by removing larger deposits. Several studies have focused on the impact of hydrodynamic conditions, e.g., mean transmembrane pressure ($\overline{TMP}$) and crossflow velocity [29, 192, 193]. According to the work of She et al. [192],

increasing applied pressure negatively impacts on process performances, since, due to the higher initial fluxes, a greater amount of solutes is brought to the membrane surface. Experimental results also confirmed the positive effect of CF velocity – or rather shear forces – on material deposition owing to the enhanced back transport, the reduced concentration polarization (CP) and the higher degree of foulant removal.

Less studied is the effect of the pumping system used to process the feed solution on fouling, especially when dealing with protein solutions. Haberkamp et al. [194], by employing both a gear and a rotary pump observed a significant influence of shear forces on the molecular structure of bovine serum albumin (BSA) in aqueous solutions undergoing ultrafiltration, which upon stress-induced denaturation can form lower molecular weight fragments that easily access pores, causing blockage rather than the buildup of a cake layer. The effect of an oscillatory flow has been investigated by several authors [195-197]. The characteristic pressure fluctuations associated with the pumping system improve permeation efficiency firstly by acting on the initial stages of foulants deposition, mostly dominated by the detrimental effects of CP [30, 195]. The hydrodynamic instabilities caused by pressure oscillations also loosen deposit layer structure, enhancing its permeability [197]. The pumping system not only plays a role on cluster formation or disintegration, but also on flux distribution and most importantly on $\overline{\mathrm{TMP}}$, which can be tuned to positively affect filtration efficiency [197]. In addition, it is relevant for the design of the filtration modules. For example, DE filtration modules can be very different from their CF counterpart, with direct consequences on the hydrodynamics of the system. Indeed, local flux inhomogeneities critically affect deposition and process performances in terms of active filtration area, as shown by Wiese et al. [159]. Although these studies have provided some important qualitative insight, a systematic investigation of the effect of the pumping system on fouling in microfiltration is still lacking in the

literature. In particular, the complex interplay between the pumping system and the aforementioned variables which are known to affect fouling, such as filtration mode, $\overline{\mathrm{TMP}}$ and membrane porosity, has not been fully elucidated.

In the following sections, the focus will be on the role played by the pumping system on fouling of bovine serum albumin (BSA) aqueous solutions undergoing microfiltration in an originally designed multi-purpose microfluidic filtration module. The latter hosts a small flat sheet membrane and allows to implement dead-end and crossflow configurations. Based on this modular design, a quantitative analysis and systematic comparisons were developed between peristaltic, syringe and pressure driven (i.e., a pressure based microfluidic flow controller) pumping systems as a function of membrane pore size and $\overline{\mathrm{TMP}}$ in different filtration modes. Results include constant-pressure flux data, BSA concentration and scanning electron microscopy (SEM) images of the membranes. Flux data have been further compared with predictions from literature models to provide a mechanistic interpretation as well.

5.1 Experimental

5.1.1. Filtration Module Design and Development

The concept of a multi-purpose device led to the development of the microfluidic filtration module, whose design was implemented using a 3D CAD software which enables precise prototyping and can be easily interfaced with numerical control machines.

The filtration module is made up of two aluminum (Anticorodal 6082) parts, namely a core and an external case (Figure 17a). The two sections of the core are aimed at tightly holding a flat sheet membrane in between with the help of four countersunk screws, constituting thereby the heart of the system. Here a rounded edges slot (20×4 mm with 2 mm radius rounding on the short sides) provides

an active filtration area of $75.6\ mm^2$. The depth of the filtration chamber above and below the membrane surface is defined by the thickness of each core section, i.e. $2.5\ mm$. The communication between the filtration area and the feed, retentate and permeate currents is enabled by the presence of a channel on each of the outer sides of the core parts whose section measures $4 \times 1\ mm$ and is $64\ mm$ long (Figure 17b). The rationale behind the choice of the shape and dimensions of the core's channels was dictated by the need for a simple geometry, by the precision of the numerical control machines employed for its construction and by the mechanical resistance of the employed material. Indeed, the implementation of a smaller cross section might have led to the deformation of the aluminum slab constituting each core section. Besides the advantages coming from the reduced dimensions of the channels, such as the reduced reagent consumption typical of microfluidic systems, the implementation of a central core separated from the external case enables possible future modifications on the channel path without substantial variations of the global design of the module.

The system's core is enclosed by the two case sections, each one equipped with a $45 \times 20\ mm$ polycarbonate inspection window (Schilder Himmel, Germany). The function of these structures is to ensure module sealing, allow visual observation of the filtration process and host the inlet/outlet connectors, two on each case section. To prevent any leakage a $\emptyset 1$ O-ring was positioned between the core sections in an appropriate groove, whereas two $1\ mm$ thick custom shaped gasket sheets were used to properly separate the internal parts from the external case. The presence of the latter increases the total height of both the inlet/outlet channels and of the filtration chambers respectively to 2 and $3.5\ mm$.

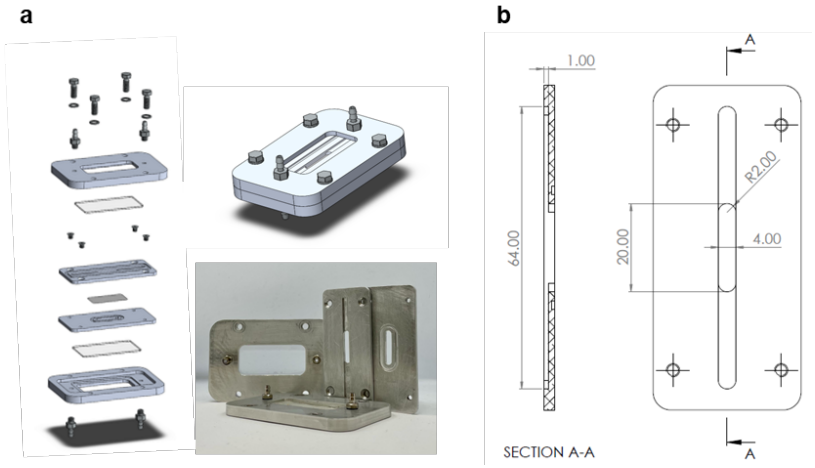

Figure 17. ***(a)*** *Microfluidic filtration module assembly;* ***(b)*** *central core schematic drawing. Quotes are expressed in mm.*

The resulting structure of the device is made of a membrane flat sheet sandwiched between the two core parts, which define the filtration chamber and both the retentate and permeate sides, and the case. Thanks to the presence of four accesses, each one functioning as inlet or outlet, a single module can be operated for different filtration modalities. By using just one inlet and one outlet, dead-end filtration can be performed; instead, using an inlet and two outlets – for the retentate and permeate currents, respectively – crossflow mode can be achieved. Finally, an additional inlet can be used if a secondary current on the permeate side is required; a similar configuration is of particular interest in applications such as forward osmosis, where concentration gradients constitute the main driving force [198, 199].

5.1.2. Materials

Two different commercially available polyethersulfone (PES) membranes (Sterlitech, USA) were used in this work, characterized by a mean pore size ($\bar{d}_p$) of 0.45 (PES452005) and 0.2 µm (PES022005) and a nominal thickness of $110 - 150$ µm. According to manufacturer's specification, PES membranes are endowed with an asymmetric pore structure, i.e. pore dimension varies along the

thickness of the membrane; as a consequence, larger pores occur on one side, while smaller ones are present the opposite side. Filtration experiments were all performed with the smaller pores side of the membrane facing the feed solution.

Aqueous protein solutions were prepared at a concentration of $100\ \mathrm{mg\ mL^{-1}}$ from bovine serum albumin (BSA, from MICROGEM, Italy) and double distilled water.

5.1.3. Membrane Fouling Monitoring Setup and Operation

Constant pressure experiments were carried out by means of three different pumping systems, both dead-end and crossflow filtration modalities were realized (Figure 18) . Specifically, a micropump system based on a pressure-driven flow controller (PDFC) (MFCSTM-FLEX, Fluigent, USA) was adopted for DE tests, in which the desired pressure was directly imposed. Such pressure controller can supply a pressure of up to $1000\ \mathrm{mbar}$ and was controlled via a dedicated software (MAESFLO). On the other hand, the CF filtration configurations were implemented by using either a syringe pump (Pump 33 DDS, Harvard Apparatus, USA), equipped with a $60\ \mathrm{mL}$ syringe (Becton Dickinson, USA), or a peristaltic pump (Masterflex L/S with an Easy-Load II pumping head, Antylia Scientific, USA), therefore imposing in both cases a constant feed flowrate. The latter was also used to perform CF filtration tests with an auxiliary current flowing on the permeate side, which was operated with a second peristaltic pump. To obtain the desired mean transmembrane pressure values in CF filtration experiments, roller clamps were placed on the retentate and permeate outflow tubing. The adjustable pressure drop created in such a manner across the filtration module was monitored every $0.2\ \mathrm{s}$ using two microfluidic pressure sensors (QuickStart Pressure sensor, IDEX Health and Science, USA) placed right before each roller clamp and connected to a dedicated software (QuickStart Sensor Software, IDEX Health and Science, USA).

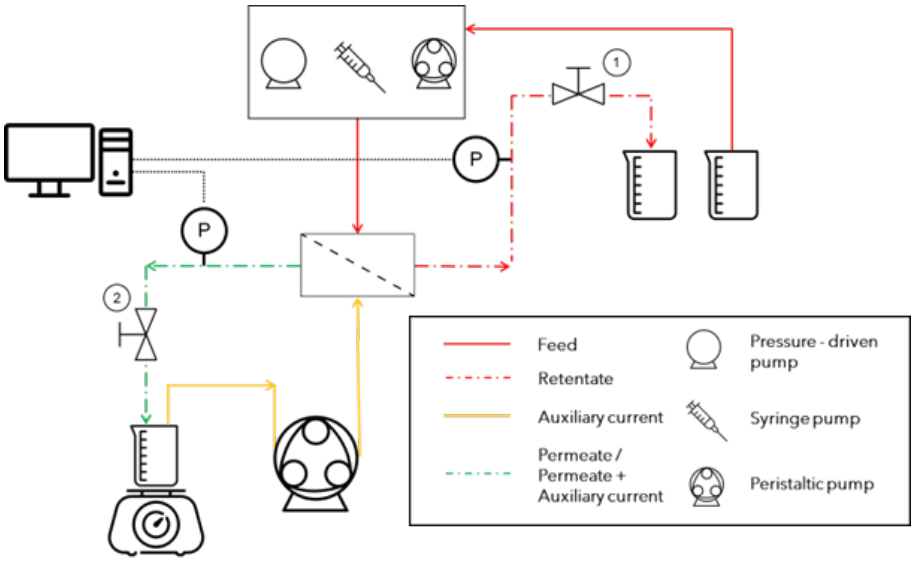

Figure 18. *Schematic diagram of the microfiltration apparatus. The different adopted pumping systems are shown together with the position of the clamps and the pressure sensors. 1 and 2 refer to the roller clamps.*

Prior to every trial, membranes were opportunely conditioned according to the following procedures. In DE tests, the filtration module was filled with deionized water using two pressure controllers for the feed and the permeate side separately. A 20 mbar pressure drop was applied on both sides, in order to achieve null $\overline{TMP}$. After around 10 min, the pressure controller on the permeate side was switched off, while the feed one was set at the required value to achieve the desired $\overline{TMP}$. It is worth to note that the applied pressure was slightly higher than the one required for a set $\overline{TMP}$ value, due to the pressure drop occurring across the pumping system tubing. The described conditions were maintained for a minimum of 10 min and until no relevant change in the measured $\overline{TMP}$ was observed. The conditioning procedure for CF filtration experiments was conducted in a similar fashion. Two syringes were employed with the syringe pump, whereas a second peristaltic pump was used for the related tests. In both cases, the desired flowrate was imposed during the module filling process keeping the roller clamps fully open. Afterwards, the permeate side pump was stopped and the desired pressure value was reached by carefully tightening the retentate side

clamp. As far as it concerns the CF with auxiliary current experiments, both peristaltic pumps were kept working during the second step, where the desired $\overline{\mathrm{TMP}}$ was applied.

Two transmembrane pressures were explored in this study, namely 20 and $120\ \mathrm{mbar}$. To achieve such values in CF filtration experiments, applied flow rates of 2 and $5\ \mathrm{mL\ min^{-1}}$ were used, respectively. The same flow rate was used for both inlet streams in the CF with auxiliary current tests.

For each test, permeated mass was monitored for 25 to $30\ \mathrm{min}$ with a sampling rate of $30\ s$ via a precision balance (Pioneer Plus Precision PA2202, OHAUS, USA, $0.01\ \mathrm{g}$ precision), linked to a data connection software (SPDC Data Connection, OHAUS, USA). Permeate fluxes were subsequently obtained by processing the raw data using Matlab. Filtration experiments were performed at least twice to ensure good reproducibility.

Scanning electron microscopy (SEM) analysis was performed on both virgin and fouled membranes (FEI INSPECT S, Thermo Fischer Scientific, USA). In order to image membrane section, samples were subject to direct freeze fracture ensuring little to no delamination [200]. Dried membrane sheets were fully submerged in liquid nitrogen and then cracked with the help of two pairs of stainless steel tweezers.

5.1.4. Chemical Analysis

BSA concentration in retentate and permeate streams was determined by spectrophotometry (UV-1700, Shimadzu, Japan). For each experiment, a calibration curve of protein concentration as a function of absorbance was computed using five samples with known concentration obtained by diluting the feed $100\ \mathrm{mg\ mL^{-1}}$ BSA solution. For all the calibration curves, the R^2 coefficient was higher than 0.99 in the application range.

5.1.5. Mathematical modeling

Flux decrease in constant pressure filtration tests was modeled by means of the previously described blocking filtration laws and cake filtration model (Table 1). Parameter estimation for each model was performed using MATLAB according to the nonlinear least squares method using the trust-region algorithm implemented in the software curve fitting tool. Goodness of fit was expressed in terms of R^2.

5.2. Results and discussion

5.2.1. Effect of the pumping system in different filtration modes

The effect of three different pumping systems on fouling evolution, namely a pressure-driven flow-controller, a syringe pump and a peristaltic pump, was investigated at a constant $\overline{TMP}$ of 20 mbar with 0.45 µm mean pore size membranes.

Prior to BSA fouling evaluation, the effects of the pumping systems on pure water flux (J_w) was investigated. Such measurements are essential to assess differences in the flow conditions, which could affect permeate fluxes. The data of J_w for the different experimental conditions in Table 3 show that higher permeate flux values are achieved by employing a peristaltic pump. The desired flowrate is indeed delivered by a set of rotating cylinders which repeatedly squeeze the inlet tubing generating a pulsating flux and thus oscillations of the $\overline{TMP}$, whose peaks are responsible for the enhanced transport across the membrane. The presence of an auxiliary current on the permeate side, still supplied by a peristaltic pump, slightly improves the beneficial effects of the oscillating $\overline{TMP}$. Despite the more stable flux provided by the syringe pump, dissimilarities are observable comparing CF and DE test, the latter carried out with the PDFC. Results can be explained considering the hydrodynamic differences between CF and DE

filtration modalities. In DE filtration the whole feed stream is processed through the membrane, which is almost homogeneously exposed to the desired transmembrane pressure; conversely, the presence of the retentate in CF mode implies a pressure drop along the membrane surface which can be accounted as the main cause of the higher pure water flux.

Table 3. *Pure water flux values at different* $\overline{TMP}$ *for* 0.45 μm *and* 0.2 μm *mean pore size membranes. DE: dead end; CF: crossflow; CF (aux): crossflow with auxiliary current on the permeate side. PDFC indicates the Pressure Driven Flow Controller.*

Filtration test	DE PDFC 0.45 µm 20 mbar	CF Syringe 0.45 µm 20 mbar	CF Peristaltic 0.45 µm 20 mbar	CF (aux) Peristaltic 0.45 µm 20 mbar	DE PDFC 0.2 µm 20 mbar	CF Peristaltic 0.2 µm 20 mbar	DE PDFC 0.2 µm 120 mbar	CF Peristaltic 0.2 µm 120 mbar
$\mathbf{J_w}$, **mm s^{-1}**	0.171 ±0.034	0.212 ± 0.010	0.354 ± 0.004	0.379 ± 0.012	0.128 ± 0.003	0.164 ± 0.004	0.560 ± 0.048	0.528 ± 0.018

After running the above described preliminary tests on water, we turned our attention to the filtration of the BSA aqueous solution to study the effect of fouling on the permeate flux J_p, as shown in Figure 19. The latter was determined as the time derivative of the permeate mass data which are plotted in the inset of Figure 19. Regardless of the pumping system and filtration mode, all curves of permeate flux J_p vs time exhibit a decreasing trend associated with the onset of the fouling phenomena. The time evolution of the permeate flux can be divided into three zones. The first one is characterized by a steep flux decline at the very beginning of the filtration tests, where foulants are convectively transported towards the membrane and start accumulating due to mechanical rejection. After this initial rapid build-up, a second zone corresponding to a slower flux decline can be observed, where the rate of solute deposition decreases. Eventually, in the third zone flux variations reduce till a quasi-steady state value is reached, likely due to a dynamic equilibrium between solute transport and deposition depending on the pumping system and the filtration mode.

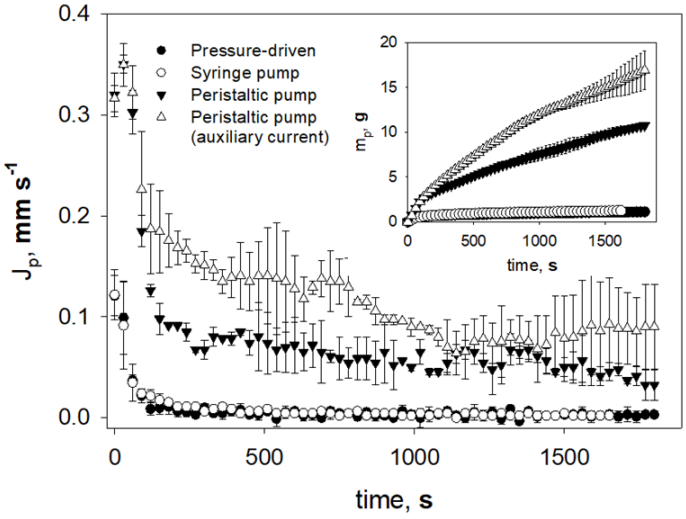

Figure 19. *Effect of the pumping system and filtration mode on the permeate flux at 20 mbar for* 0.45 *µm mean pore diameter membranes.*

Concerning the pumping systems, data of syringe, peristaltic and pressure-driven pumps are all plotted in Figure 19. Both syringe (open circles) and peristaltic pumps (full triangles) were used in CF filtration tests, and marked differences between these two systems were found in terms of flux trend over time. Indeed, despite the same $\overline{TMP}$ and membrane characteristics, higher initial and stationary fluxes – J_0 and J^* respectively – can be achieved by means of a peristaltic pump flowing the feed solution; a less steep decline can be observed as well, indicating a slower development of the fouling dynamics. In addition, larger J_p fluctuations are found for the peristaltic system as compared to the syringe pump. The main reason of this difference can be attributed to the pulsating $\overline{TMP}$ which is typical of peristaltic pumping. Flux data also point out how the presence of a countercurrent auxiliary stream on the permeate side (open triangles) enables higher quasi-stationary fluxes and an even slower fouling development compared to standard peristaltic pumping (without the auxiliary current, full triangles). The higher fluxes can be related to the combined effects of a peristaltic flux acting on both sides of the membrane, which enhances local pressure oscillations. Finally,

the effect of pressure-driven pumping was investigated in the dead-end filtration mode (full circles). Here, flux decline appears to be comparable with the one obtained using a syringe pump in CF mode, with quite slight differences at the very beginning of fouling development and equivalent stationary fluxes.

As described in the Materials and Methods section, the BSA concentration in all the experiments was measured by spectrophotometry. Table 4 shows BSA concentration in the retentate and in the permeate at the end of each test for the experimental conditions of interest. BSA concentration in all the retentate currents is close to the nominal value of initial concentration ($100\ \mathrm{mg\ mL^{-1}}$), whereas it is at least 10 times lower in the permeate. Such result shows that most of the albumin in the feed solution remains in the retentate current and does not pass through the membrane, in spite of the large size difference between the nominal membrane pores ($0.45\ \mu\mathrm{m}$) and the albumin molecule (Stokes radius of $3.5\ \mathrm{nm}$). Furthermore, the BSA concentration in the permeate current is strongly influenced by the pumping system: the values of BSA permeate concentration are much higher in the peristaltic CF tests than those in the pressure-driven DE and syringe CF ones ($85 \pm 3\ \mathrm{mg\ mL^{-1}}$ *vs* a concentration $< 1\ \mathrm{mg\ mL^{-1}}$ for the syringe pump). The difference between BSA concentration in the peristaltic CF with and without auxiliary current (85 *vs* $30\ \mathrm{mg\ mL^{-1}}$) can be explained by some dilution which is introduced by the presence of the auxiliary current itself. It can be pointed out that the vanishing value of BSA concentration in DE tests is quite striking and not really expected. In fact, in the DE filtration mode there is no retentate current and all the volume processed in the test must flow across the membrane. It can be concluded that all the BSA present in the feed should be somehow retained by the membrane.

Table 4. *BSA concentration (mean and standard deviation) in the retentate and permeate outlets for the different pumping systems, at different $\overline{TMP}$ and mean pore size. Quasi-steady state permeate fluxes are reported as well.*

Filtration test	$[\mathbf{BSA}]^{\mathbf{ret}}_{\mathbf{t=25\ min}}$, $\mathbf{mg\ mL^{-1}}$	$[\mathbf{BSA}]^{\mathbf{perm}}_{\mathbf{end}}$, $\mathbf{mg\ mL^{-1}}$
DE – PDFC 0.45 µm – 20 mbar $J^* = 0.003$ mm s^{-1}	–	< 1
CF – Syringe 0.45 µm – 20 mbar $J^* = 0.002$ mm s^{-1}	100 ± 1	< 1
CF – Peristaltic 0.45 µm – 20 mbar $J^* = 0.038$ mm s^{-1}	96 ± 1	85 ± 3
CF (aux) – Peristaltic 0.45 µm – 20 mbar $J^* = 0.081$ mm s^{-1}	100 ± 4	30 ± 9
DE - PDFC 0.2 µm - 20 mbar $J^* = 0.003$ mm s^{-1}	–	< 1
CF - Peristaltic 0.2 µm - 20 mbar $J^* = 0.002$ mm s^{-1}	100 ± 2	< 1
DE - PDFC 0.2 µm - 120 mbar $J^* < 0.001$ mm s^{-1}	–	22 ± 1
CF - Peristaltic 0.2 µm - 120 mbar $J^* = 0.004$ mm s^{-1}	100 ± 1	26 ± 4

To check this finding and, more in general, to look at the microstructure of BSA deposits in the membrane SEM observations were carried out on samples corresponding to the different experimental conditions. Images of both pristine and fouled membranes sections obtained by freeze fracture were collected. Some

representative micrographs are shown in Figure 21. The pristine membrane (Figure 21a) is characterized by the asymmetric structure of the commercial PES membranes used in this work, where a thin, dense layer made of fine pores can be seen on the top surface, while a sponge-like, heterogenous network with larger porosity can be observed inside the membrane. The fouled DE membrane (Figure 21b) exhibits a top surface layer of about 2 mm thickness and a pronounced accumulation of the deposits inside the porous structure of the membrane, which appears to be made of thicker fibers compared to the pristine membrane, confirming therefore the presence of internal fouling. The fouled CF-syringe pump membrane (Figure 21c) is characterized by the presence of some large deposits (see the arrow) on the top surface, which otherwise looks similar, if not slightly thicker, to the one of the pristine membrane. The membrane interior displays a sponge-like structure with thickened fibers as compared to the pristine membrane. The fouled CF-peristaltic pump (Figure 21d) shows a thick cake layer of $5-6$ µm on the top of the membrane surface, whereas the microstructure of the inner part looks similar to that of the fouled CF-syringe pump membrane.

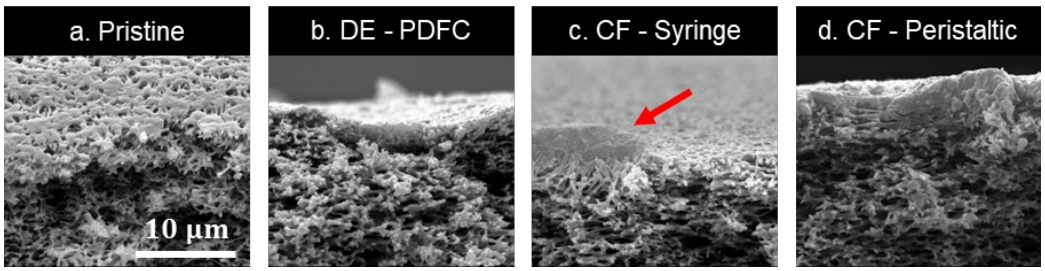

Figure 20. *SEM micrographs of 0.45 µm mean pore diameter membranes section:* ***(a)*** *pristine ;* ***(b)*** *DE ;* ***(c)*** *CF - Syringe pump ;* ***(d)*** *CF – Peristaltic pump.*

The results described so far show a remarkable effect of the pumping system on the outcome of microfiltration tests under the same conditions of transmembrane pressure, membrane type and porosity. The pumping system affects even the pure water fluxes J_w, which are about twice as large with the peristaltic pump as compared to the syringe one in CF filtration. A larger value of J_w is also found

when comparing the peristaltic pump in CF filtration with the pressure driven one in DE mode.

The effect of the pumping system becomes even more important in the filtration of albumin aqueous solution when fouling takes place. In this case, as already pointed out, initial permeate fluxes with peristaltic pumps are about 3 times as large as the ones with syringe pump in CF mode. Such a difference is still present at later times, when permeate flux declines towards a quasi-stationary state, reaching a value of an order of magnitude at the end of the experiment. It can be concluded that the pumping system per se has a strong influence on the fouling process and thus on filtration throughput.

The fouling process due to albumin can be described in terms of the following general features. Having a much smaller dimension compared to the pore size, albumin molecules should theoretically be free to flow through the membrane structure, however adsorption and denaturation processes force them to deposit often irreversibly [86, 113, 201]. As a matter of fact, single proteins accumulate on the membrane surface and inside the pores under the influence of hydrophobic interactions, drastically reducing pore diameter and consequently lowering membrane permeability. Pre-existing aggregates, whose formation is caused by protein denaturation, can also deposit and shield pore entrances, hindering the permeate flow [202]. This picture of albumin fouling can explain the results obtained in the DE filtration mode, such as the time decrease of J_p and the presence both of a cake layer on the membrane surface and of internal fouling. The latter, however, does not lead to complete clogging of the membrane, since a porous microstructure is still visible in the SEM images (see Figure 21b). In fact, a small, but nonzero value of permeate flux is still found at the end of the experiment (see Table 4). Therefore, it can be speculated that the longer residence time inside the membrane caused by the slowing down of permeate flux, which is

likely due to the formation of the cake, promotes albumin adsorption inside the membrane. Hence, essentially no albumin is found in the permeate current.

Concerning the results of CF peristaltic pumping, we observe a thick cake layer on the membrane surface and some internal fouling, although less than what is found for DE filtration. These observations, together with the fact that albumin concentration in the permeate is just slightly lower than that in the retentate, can be interpreted by hypothesizing that the cake layer is quite porous, thus allowing the passage of albumin molecules. This hypothesis is consistent with the finding that permeate flux in the CF peristaltic mode is much larger than the one in the DE mode. Hence, the residence time of albumin inside the membrane is much lower in the CF peristaltic mode as compared to the one in the DE mode, giving less time to albumin molecules to bind to the membrane inner pores. On the other side, as compared to the peristaltic mode, when a syringe pump is used for CF filtration, a thinner cake layer can be observed (Figure 21c), the permeate flux is much lower and the albumin concentration is close to zero. These results are similar to the ones found for DE filtration, thus showing that the CF alone cannot explain the differences with respect to the peristaltic pumping. The role played by the oscillating nature of peristaltic flow was also described by Weinberger et al., who studied the performance of alternating crossflow filtration on the processing of a cell and protein mixture [196].

5.2.2. Effect of the mean pore size

In the following two subsections, we explore the effects of membrane pore size and transmembrane pressure to further confirm the results presented so far. Concerning the former, a $\bar{d}_p = 0.2\ \mu m$ membrane was employed. Constant pressure filtration tests were performed at the same value of $\overline{TMP} = 20\ mbar$ in both dead-end and crossflow modes, the latter by using a peristaltic pump. Results

were compared to those obtained in the same conditions with 0.45 µm mean pore diameter membranes.

Starting with the flow of pure water, the permeate flux J_w, both in DE and CF, is lower as compared to the one through the membranes of 0.45 µm (0.172 *vs* 0.138 mm s^{-1} for DE and 0.357 *vs* 0.159 mm s^{-1} for CF), as reported in Table 3. These findings suggest that, despite the different mean pore diameter, the two PES commercial membranes may be characterized by overlapping pore size distributions, which result in similar pure water flux values. The effect of the different pumping system is more evident in CF tests carried out with peristaltic pumps, where much lower permeate flux differences are found between 0.45 and 0.2 µm membranes, presumably because the positive effects of the $\overline{TMP}$ oscillations play a major role on wider pores.

Going now to the case of albumin solutions, which is shown in Figure 22, the time evolution of permeate flux is quite similar in DE filtration tests with pore size of 0.2 and 0.45 µm, to the point that little distinction can be made between the two membranes.

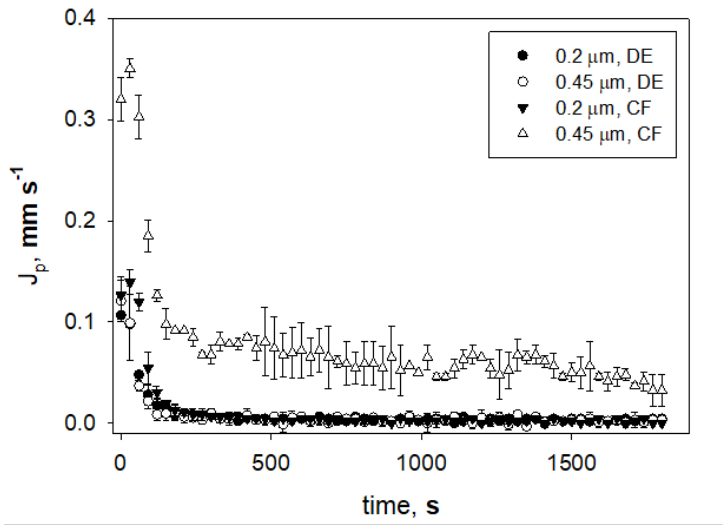

***Figure 21**. Influence of the mean pore size on the permeate flux at 20 mbar for dead-end and crossflow filtration modes.*

Comparable solute rejection is observed as well, with a BSA concentration in the permeate lower than $1\ \mathrm{mg\ mL^{-1}}$ for each DE mode test. In spite of being both affected by internal fouling, different deposit morphologies characterize the two fouled membranes. As shown in Figure 24b and e, corresponding to 0.2 and $0.45\ \mu\mathrm{m}$ mean pore size membranes cross-section, respectively, denser structures are observed in the former, with foulant deposits clogging the inner porous matrix blending with superficial agglomerates. This behavior is consistent with the already mentioned hypothesis that clogging in DE mode is mostly affected by the residence time of the BSA water solution, in turn depending on membrane morphology. The growth of BSA deposits tends to attenuate the difference in the membrane internal morphologies, with larger pores being restricted and smaller pores almost blocked by BSA fouling. The consequence is a rapid decline of permeate flux, which tends to vanish at around $400\ \mathrm{s}$.

Significant differences characterize CF filtration experiments instead. Here, much lower initial and long-term fluxes are observed for $\bar{d}_p = 0.2\ \mu\mathrm{m}$ membranes, together with a steeper flux decline throughout the whole filtration test. A much lower protein concentration in the permeate was measured as well ($85 \pm 3\ \mathrm{mg\ mL^{-1}}$ for $0.45\ \mu\mathrm{m}$ *vs* values $< 1\ \mathrm{mg\ mL^{-1}}$ for $0.2\ \mu\mathrm{m}$ membranes). These findings indicate a stronger impact of fouling on the $0.2\ \mu\mathrm{m}$ membranes regardless of the presence of a peristaltic flow on the feed side, also suggesting a shift towards a predominantly internal deposition. No further benefit is thus brought by the mitigating effects associated with $\overline{\mathrm{TMP}}$ oscillations as observed for $0.45\ \mu\mathrm{m}$ mean pore size membranes. SEM micrograph of $\bar{d}_p = 0.2\ \mu\mathrm{m}$ CF fouled membranes cross-sections (Figure 24c) confirm the presence of internal BSA deposits; a thinner fouling layer on the membrane surface is also observed, compared to the one which characterizes the $\bar{d}_p = 0.45\ \mu\mathrm{m}$ CF fouled membrane shown in Figure 24f.

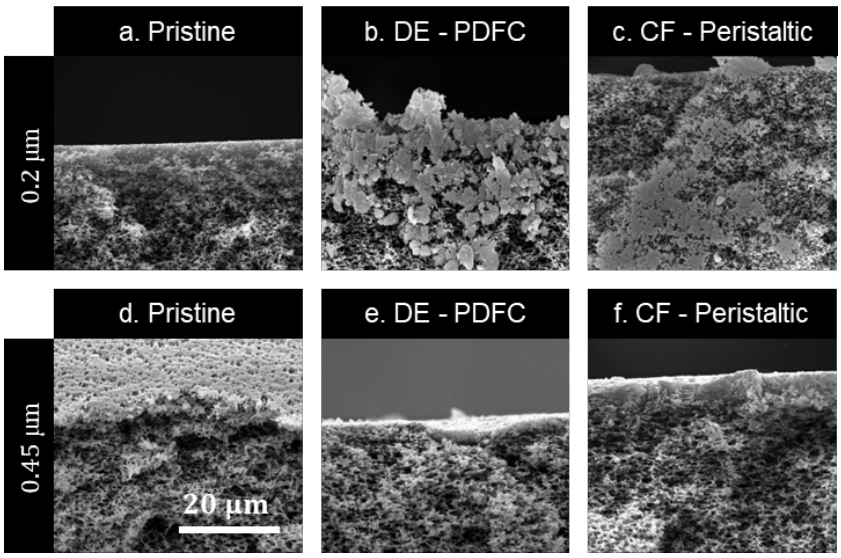

Figure 22. *SEM micrographs of membranes section: (**a**) pristine 0.2 µm; (**b**) 0.2 µm DE; (**c**) 0.2 µm CF - Peristaltic pump; (**d**) pristine 0.45 µm; (**e**) 0.2 µm DE; (**f**) 0.45 µm CF - Peristaltic pump.*

5.2.3. Effect of the Mean Transmembrane Pressure

The influence of the mean transmembrane pressure on protein fouling dynamics was assessed employing $\bar{d}_p = 0.2$ µm membranes. Both dead-end and crossflow modes were investigated, the latter realized using a peristaltic pump. Two $\overline{TMP}$ were explored, namely 20 and 120 mbar. As shown in Table 3, no difference of the water flux J_w is found between DE PDFC and CF peristaltic modes at a $\overline{TMP}$ of 120 mbar. Thus, under this transmembrane pressure no improvement is brought by peristaltic pumping.

Concerning the BSA water solution, a higher $\overline{TMP}$ results in the enhancement of the initial flux J_0 in both DE and CF filtration modes, especially for the latter, as shown in Table 4. Owing to the higher $\overline{TMP}$, a longer time was also necessary to reach the stationary flux value J^*; as a consequence, higher flux values are observed in the second region of the curves where flux decline begins to occur. However, the quasi steady state fluxes are close to the ones at $\overline{TMP} = 20$ mbar, suggesting that at long time permeation is primarily controlled by the deposited

foulant layer regardless of the imposed driving force, or rather transmembrane pressure. Despite the comparable stationary fluxes between the two values of $\overline{\mathrm{TMP}}$, a much higher BSA permeation was observed for $\overline{\mathrm{TMP}} = 120\ \mathrm{mbar}$ tests ($22 \pm 1\ \mathrm{mg\ mL^{-1}}$ at $120\ \mathrm{mbar}$ *vs* values $< 1\ \mathrm{mg\ mL^{-1}}$ at $20\ \mathrm{mbar}$ for DE, $26 \pm 4\ \mathrm{mg\ mL^{-1}}$ at $120\ \mathrm{mbar}$ *vs* values $< 1\ \mathrm{mg\ mL^{-1}}$ at $20\ \mathrm{mbar}$ for CF). The sharper solute permeation across the membrane is a direct consequence of the enhanced convective transport caused by the higher $\overline{\mathrm{TMP}}$. An overlook at the fluxes trend over time clarifies the detrimental effects coming from an increase of the $\overline{\mathrm{TMP}}$ in terms of fouling enhancement; as a matter of fact, comparing J_0 and J^* between the low and high pressure tests for both DE and CF modes, a heavier flux decline is clearly observed. It is worth to note that in order to achieve a $\overline{\mathrm{TMP}} = 120\ \mathrm{mbar}$ in CF mode by means of a peristaltic pump, a feed flowrate $Q_F = 5\ \mathrm{mL\ min^{-1}}$ had to be set. The impact of crossflow velocity on fouling inhibition was considered negligible compared to the $\overline{\mathrm{TMP}}$ one.

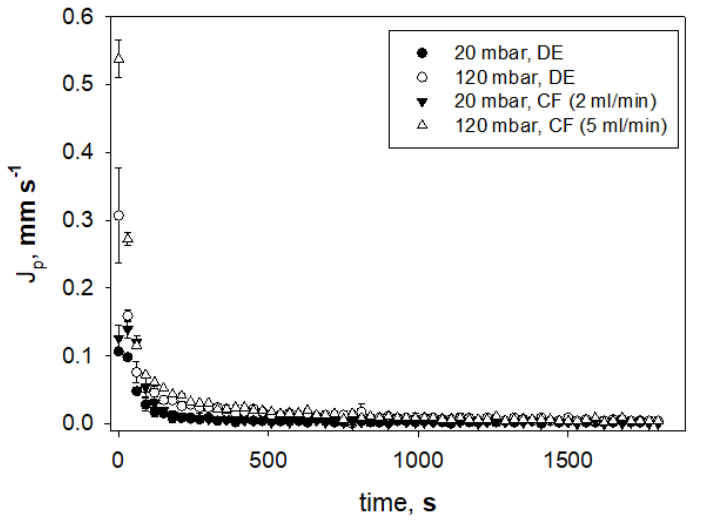

Figure 23. *Effect of the $\overline{TMP}$ on the permeate flux for* 0.2 *μm mean pore diameter membranes in both dead-end and crossflow filtration modes.*

SEM micrographs confirm the presence of internal BSA deposits for both DE and CF tests at $\overline{\mathrm{TMP}}$ of $120\ \mathrm{mbar}$. Similarly to what observed for lower pressure tests,

inner deposits connect to the ones on the surface, forming complex structures which completely clog the pores. It can be observed that at 120 mbar a more diffuse clogging patterns is present, both for CF (Figure 27b) and DE (Figure 27d).

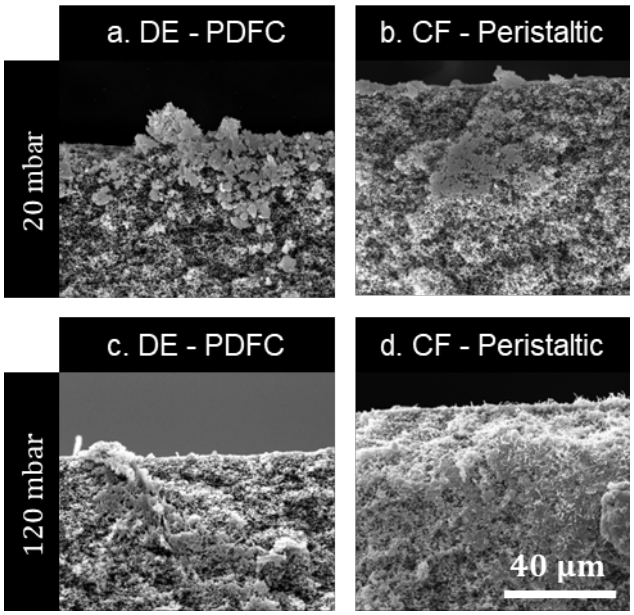

Figure 24. *SEM micrographs of* $\bar{d}_p = 0.2\ \mu m$ *membranes section:* ***(a)*** $20\ mbar$ *DE;* ***(b)*** $20\ mbar$ *CF - Peristaltic;* ***(c)*** $120\ mbar$ *DE;* ***(d)*** $120\ mbar$ *CF - Peristaltic.*

5.2.4. Fouling Mechanism Interpretation

Figure 28 shows permeate flux prediction according to Hermia's models for all the constant pressure filtration tests performed varying the pumping system (and filtration mode consequentially), the mean pore size and the TMP. For each dataset and model, fitting accuracy was estimated by analyzing residual plots and evaluating the coefficient of determination (R^2). Model parameters and related R^2 are summarized in Table 5.

Despite the relatively high R^2 values for most of the filtration tests, the complete blocking model often overpredicts the initial flux decline while underestimating the long-term variations (Figure 28c, e, f, g). A heavier impact of fouling is thus

expected according to this model, which best suits CF filtration tests using a syringe pump or a peristaltic pump respectively with 0.45 and 0.2 µm mean pore diameter membranes at 20 mbar.

Almost none of the performed experiments appear to be fairly interpreted by the standard blocking model, whose R^2 values are however very close to the complete blocking or intermediate blocking ones in several cases. Apparently, BSA fouling does not proceed mainly by reducing pore diameter from the inside, although such event can be assumed to take place in the tests where the model goodly fits experimental data.

The intermediate pore blocking model is on average the best fitting one among the others, with the highest R^2 value (0.999) for the CF test using a peristaltic pump, 0.2 µm membranes and a TMP of 120 mbar. As it also considers the probability that a new foulant particle can interact with already present ones, this model considers a higher complexity level in the interpretation of fouling which potentially explains BSA deposition very well.

As the low – or even negative – R^2 values show, the cake filtration model is not suitable for the interpretation of BSA fouling in the presented filtration tests. Despite fitting the steady-state flux values, this model highly overpredicts the initial fluxes especially in CF experiments, where it often numerically infinite (indicated as a dash in Table 4). Higher goodness of fit can be observed in DE test, where the formation of an actual permeable cake is more frequent due to the absence of any shear force or mixing action as in CF mode happens.

Apart from the cake filtration model, all the Hermia's pore blocking laws give a fair interpretation of the presented experimental data, making it difficult to directly assess the dominating fouling mechanism. Two reasons can be found behind the absence of a best fitting model. Firstly, Hermia's models consider both foulants and the membrane in a simplified way, hiding in the K and n coefficients

information like membrane morphology and foulant size distribution. In addition, directly using models' particularized equations forces the whole experimental data set to follow a certain model, as n values are not supposed to be different from the presented ones. The adoption of combined models represents a possible solution to the interpretation of fouling with complex solutes such as proteins [30].

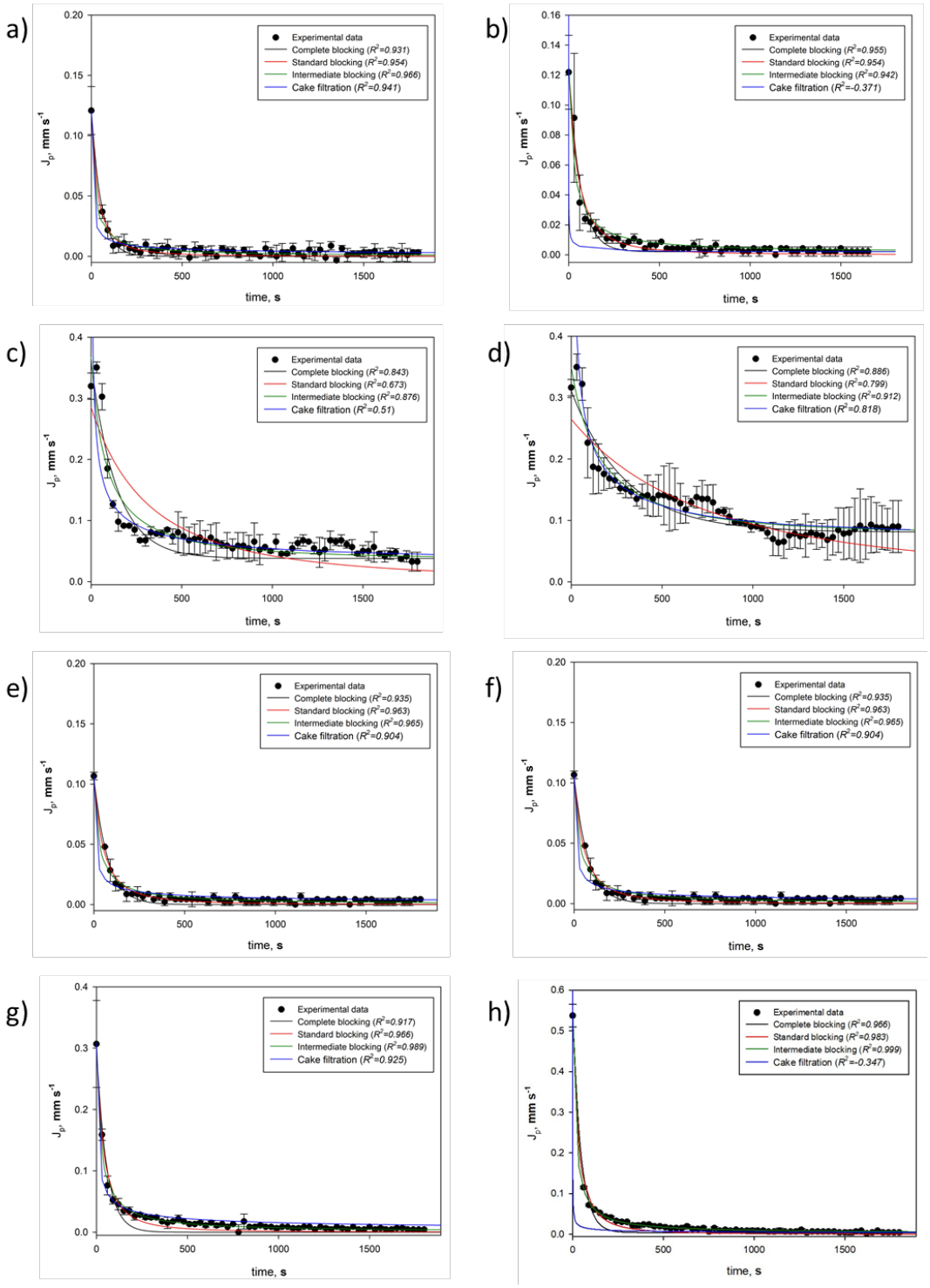

Figure 25**. Permeate flux predictions according to Hermia's models for constant pressure filtration.* ***a) *DE,* 20 *mbar,* 0.45 *μm;* ***b)*** *CF (syringe pump),* 20 *mbar,* 0.45 *μm;* ***c)*** *CF (peristaltic pump),* 20 *mbar,* 0.45 *μm;* ***d)*** *CF (peristaltic pump and auxiliary current),* 20 *mbar,* 0.45 *μm;* ***e)*** *DE,* 20 *mbar,* 0.2 *μm;* ***f)*** *CF (peristaltic pump),* 20 *mbar,* 0.2 *μm;* ***g)*** *DE,* 120 *mbar,* 0.2 *μm;* ***h)*** *CF (peristaltic pump),* 120 *mbar,* 0.2 *μm. Goodness of fit is expressed in terms of* R^2 *for each model in brackets.*

Table 5. *Summary of the model parameters predicted by the Hermia's models and related correlation coefficient (R^2). DE: dead end; CF: crossflow; CF (aux): crossflow with auxiliary current on the permeate side.*

Constant pressure filtration test	Complete blocking			Standard blocking			Intermediate blocking			Cake filtration		
	R^2	K_{CPB}	J_0	R^2	K_{SPB}	J_0	R^2	K_{IPB}	J_0	R^2	K_{CLF}	J_0
DE – PDFC 0.45 µm – 20 mbar $J^* = 0.003$ mm s^{-1}	0.931	0.018	0.12	0.954	0.041	0.121	0.966	0.439	0.121	0.941	26.98	0.121
CF – Syringe 0.45 µm – 20 mbar $J^* = 0.002$ mm s^{-1}	0.955	0.127	0.124	0.954	0.029	0.125	0.942	0.283	0.127	-0.371	757	-
CF – Peristaltic 0.45 µm – 20 mbar $J^* = 0.038$ mm s^{-1}	0.843	0.02	0.357	0.673	0.003	0.285	0.867	0.035	0.367	0.510	0.698	-
CF (aux) – Peristaltic 0.45 µm – 20 mbar $J^* = 0.081$ mm s^{-1}	0.886	0.011	0.311	0.799	0.001	0.265	0.912	0.019	0.349	0.818	0.246	-
DE - PDFC 0.2 µm - 20 mbar $J^* = 0.003$ mm s^{-1}	0.935	0.013	0.105	0.963	0.03	0.107	0.965	0.325	0.108	0.904	17.54	0.107
CF - Peristaltic 0.2 µm - 20 mbar $J^* = 0.002$ mm s^{-1}	0.922	0.068	0.153	0.882	0.018	0.153	0.798	0.158	0.150	-0.392	433	-
DE - PDFC 0.2 µm - 120 mbar $J^* < 0.001$ mm s^{-1}	0.917	0.018	0.296	0.966	0.023	0.302	0.989	0.136	0.309	0.925	2.045	0.308
CF - Peristaltic 0.2 µm - 120 mbar $J^* = 0.004$ mm s^{-1}	0.966	0.041	0.532	0.983	0.022	0.534	0.999	0.125	0.538	-0.347	74.79	-

6. Conclusions

Due to the advantages offered by the characteristic micro-confined environments, the use of microfluidics for the investigation of fouling represents a high potential strategy for the comprehension of all the complex phenomena taking place during filtration processes.

In this chapter the state of the art concerning fouling and microfluidics was explored. The various stages characterizing the evolution of fouling were discussed, enlightening the developments enabled by the adoption of a microfluidic approach. The interpretation of fouling via a mathematical approach was then investigated and various models, based on flux and pressure data, were examined assessing their principal advantages and drawbacks. Afterwards, several dynamic *in situ* investigation techniques in which microfluidics covers a key role were reviewed. Such methodologies represent a possible solution to the limitations related to the study of fouling by means of measuring permeate fluxes or TMP variations, as they allow direct visualization of all the phenomena taking place at the microscale with unprecedented time and spatial resolutions.

An experimental study on the effect of pumping systems on fouling from aqueous BSA solutions was then presented. By means of a microfluidic filtration module, the evolution of fouling under the effect of three different pumping systems (i.e. a peristaltic pump, a syringe pump and a pressure driven flow controller) was explored as a function of membrane pore size and $\overline{\mathrm{TMP}}$ in different filtration modes. Results pointed out the crucial role of foulant residence time inside the membrane on both fouling propensity and deposit morphology, showing a significant influence of the pumping system which in some cases can actually alleviate flux decrease. As a matter of fact, the use of a peristaltic pump, at the lower pressure and for 0.45 μm membranes, resulted in higher permeate fluxes throughout the whole filtration time, with an almost twelve-fold higher quasi-

steady state flux compared to the PDFC and syringe pump cases. Reduced differences were observed in the other examined cases, underlining the role played by the membrane pore size, the transmembrane pressure and the pumping system on the residence time inside the membrane. Fouling was also modeled by means of the Hermia models; it was not possible, however, to individuate a single mechanism governing the foulants' deposition.

As shown, the implementation of microfluidics constitutes a great scientific opportunity for the elucidation of the still debated aspects of the fouling phenomena.

References

[1] N. Epstein, Thinking about heat transfer fouling: a 5× 5 matrix, Heat transfer engineering 4(1) (1983) 43-56.
[2] M. Awais, A.A. Bhuiyan, Recent advancements in impedance of fouling resistance and particulate depositions in heat exchangers, International Journal of Heat and Mass Transfer 141 (2019) 580-603.
[3] R.D. Noble, S.A. Stern, Membrane separations technology: principles and applications, Elsevier1995.
[4] W. Guo, H.H. Ngo, J. Li, A mini-review on membrane fouling, Bioresource Technology 122 (2012) 27--34. https://doi.org/10.1016/j.biortech.2012.04.089.
[5] S. Yiantsios, A. Karabelas, The effect of colloid stability on membrane fouling, Desalination 118(1-3) (1998) 143-152.
[6] A. Lim, R. Bai, Membrane fouling and cleaning in microfiltration of activated sludge wastewater, Journal of membrane science 216(1-2) (2003) 279-290.
[7] A.M.T.R. Committee, Committee report: recent advances and research needs in membrane fouling, Journal-American Water Works Association 97(8) (2005) 79-89.
[8] F.L. Santamaria, S. Macchietto, Integration of Optimal Cleaning Scheduling and Flow Split Control for Crude Oil Fouling Mitigation in the Operation of Refinery Heat Exchanger Networks, Computer Aided Chemical Engineering, Elsevier2018, pp. 1087-1092.
[9] E. Diaz-Bejarano, E. Behranvand, F. Coletti, M. Mozdianfard, S. Macchietto, Organic and inorganic fouling in heat exchangers–Industrial case study: Analysis of fouling state, Applied energy 206 (2017) 1250-1266.
[10] J. Taborek, Fouling: The major unsolved problem in heat transfer, Chem. Eng. Prog. 68 (1972) 59-67.
[11] F. Coletti, H. Joshi, S. Macchietto, G. Hewitt, Introduction to crude oil fouling, Crude Oil Fouling: Deposit Characterization, Measurements, and Modeling (2014) 1-22.
[12] L.A. Vandewalle, D.J. Van Cauwenberge, J.N. Dedeyne, K.M. Van Geem, G.B. Marin, Dynamic simulation of fouling in steam cracking reactors using CFD, Chemical Engineering Journal 329 (2017) 77-87.
[13] A.s.E. Muñoz Gandarillas, K.M. Van Geem, M.-F.o. Reyniers, G.B. Marin, Influence of the reactor material composition on coke formation during ethane steam cracking, Industrial & Engineering Chemistry Research 53(15) (2014) 6358-6371.
[14] M.A. Al Mamun, M. Sadrzadeh, R. Chatterjee, S. Bhattacharjee, S. De, Colloidal fouling of nanofiltration membranes: A novel transient electrokinetic model and experimental study, Chemical Engineering Science 138 (2015) 153-163.
[15] Membrane filtration technologies tackle water reuse and purification, Membrane Technology 2007(1) (2007) 9 - 11. https://doi.org/https://doi.org/10.1016/S0958-2118(07)70020-4.

[16] O.T. Iorhemen, R.A. Hamza, J.H. Tay, Membrane bioreactor (Mbr) technology for wastewater treatment and reclamation: Membrane fouling, Membranes 6(2) (2016) 13--16. https://doi.org/10.3390/membranes6020033.
[17] B.T. Konvensional, A review of oilfield wastewater treatment using membrane filtration over conventional technology, Malays. J. Anal. Sci 21 (2017) 643-658.
[18] B.R. Gonçalves, A.E. Machado, A.G. Trovó, Treatment of a biodiesel effluent by coupling coagulation-flocculation, membrane filtration and Fenton reactions, Journal of Cleaner Production 142 (2017) 1918-1921.
[19] G. Daufin, J.P. Escudier, H. Carrere, S. Bérot, L. Fillaudeau, M. Decloux, Recent and emerging applications of membrane processes in the food and dairy industry, Food and Bioproducts Processing: Transactions of the Institution of of Chemical Engineers, Part C 79 (2001) 89-102. https://doi.org/10.1016/S0960-3085(01)70244-1.
[20] C.Y. Tang, Z. Yang, H. Guo, J.J. Wen, L.D. Nghiem, E. Cornelissen, Potable water reuse through advanced membrane technology, ACS Publications, 2018.
[21] D.F. Stamatialis, B.J. Papenburg, M. Girons, S. Saiful, S.N.M. Bettahalli, S. Schmitmeier, M. Wessling, Medical applications of membranes: Drug delivery, artificial organs and tissue engineering, Journal of Membrane Science 308(1-2) (2008) 1--34. https://doi.org/10.1016/j.memsci.2007.09.059.
[22] T.A. Crowley, V. Pizziconi, Isolation of plasma from whole blood using planar microfilters for lab-on-a-chip applications, Lab on a Chip 5(9) (2005) 922--929. https://doi.org/10.1039/b502930a.
[23] M.-Y. Jaffrin, C.G. Caro, Biological flows, Springer1995.
[24] H. Strathmann, L. Giorno, E. Drioli, Introduction to membrane science and technology, Wiley-VCH Weinheim, Germany:2011.
[25] R.W. Baker, Membrane technology and applications, John Wiley & Sons2012.
[26] B.G. Choobar, M.A.A. Shahmirzadi, A. Kargari, M. Manouchehri, Fouling mechanism identification and analysis in microfiltration of laundry wastewater, Journal of Environmental Chemical Engineering 7(2) (2019) 103030.
[27] J. Chen, M. Zhang, F. Li, L. Qian, H. Lin, L. Yang, X. Wu, X. Zhou, Y. He, B.-Q. Liao, Membrane fouling in a membrane bioreactor: high filtration resistance of gel layer and its underlying mechanism, Water research 102 (2016) 82-89.
[28] F. Wang, V.V. Tarabara, Pore blocking mechanisms during early stages of membrane fouling by colloids, Journal of Colloid and Interface Science 328 (2008) 464--469.
[29] Y.N. Wang, C.Y. Tang, Protein fouling of nanofiltration, reverse osmosis, and ultrafiltration membranes-The role of hydrodynamic conditions, solution chemistry, and membrane properties, Journal of Membrane Science 376(1-2) (2011) 275--282. https://doi.org/10.1016/j.memsci.2011.04.036.
[30] A.I. Cirillo, G. Tomaiuolo, S. Guido, Membrane Fouling Phenomena in Microfluidic Systems: From Technical Challenges to Scientific Opportunities, Micromachines 12(7) (2021) 820.

[31] S.F. Anis, R. Hashaikeh, N. Hilal, Microfiltration membrane processes: A review of research trends over the past decade, Journal of Water Process Engineering 32(September) (2019). https://doi.org/10.1016/j.jwpe.2019.100941.
[32] B. Dez, R. Rosal, A critical review of membrane modification techniques for fouling and biofouling control in pressure-driven membrane processes, Nanotechnology for Environmental Engineering 5(2) (2020) 1--21. https://doi.org/10.1007/s41204-020-00077-x.
[33] A. Mollahosseini, A. Abdelrasoul, A. Shoker, A critical review of recent advances in hemodialysis membranes hemocompatibility and guidelines for future development, Materials Chemistry and Physics 248(December 2019) (2020) 122911. https://doi.org/10.1016/j.matchemphys.2020.122911.
[34] I.B. Hassan, M. Ennouri, C. Lafforgue, P. Schmitz, A. Ayadi, Experimental study of membrane fouling during crossflow microfiltration of yeast and bacteria suspensions: towards an analysis at the microscopic level, Membranes 3(2) (2013) 44-68.
[35] A. Thekkedath, W.M. Naceur, K. Kecili, M. Sbai, A. Elana, L. Auret, H. Suty, C. Machinal, M. Pontié, Macroscopic and microscopic characterizations of a cellulosic ultrafiltration (UF) membrane fouled by a humic acid cake deposit: First step for intensification of reverse osmosis (RO) pre-treatments, Comptes Rendus Chimie 10(9) (2007) 803-812.
[36] R.C. Lo, Application of microfluidics in chemical engineering, Chem. Eng. Process Tech 1 (2013) 1002-1005.
[37] G.M. Whitesides, The origins and the future of microfluidics, Nature 442(7101) (2006) 368-73. https://doi.org/10.1038/nature05058.
[38] P.K. Panigrahi, Transport phenomena in microfluidic systems, John Wiley & Sons2016.
[39] E. Dressaire, A. Sauret, Clogging of microfluidic systems, Soft Matter 13(1) (2017) 37-48.
[40] D.C. Duffy, J.C. McDonald, O.J. Schueller, G.M. Whitesides, Rapid prototyping of microfluidic systems in poly (dimethylsiloxane), Analytical chemistry 70(23) (1998) 4974-4984.
[41] G.C. Agbangla, É. Climent, P. Bacchin, Experimental investigation of pore clogging by microparticles: Evidence for a critical flux density of particle yielding arches and deposits, Separation and purification technology 101 (2012) 42-48.
[42] P. Bacchin, A. Marty, P. Duru, M. Meireles, P. Aimar, Colloidal surface interactions and membrane fouling: Investigations at pore scale, Advances in colloid and interface science 164(1-2) (2011) 2-11.
[43] N. Debnath, A. Kumar, T. Thundat, M. Sadrzadeh, Investigating fouling at the pore-scale using a microfluidic membrane mimic filtration system, Scientific reports 9(1) (2019) 1-10.

[44] P. Bacchin, Q. Derekx, D. Veyret, K. Glucina, P. Moulin, Clogging of microporous channels networks: role of connectivity and tortuosity, Microfluidics and nanofluidics 17(1) (2014) 85-96.
[45] J.R. Anderson, D.T. Chiu, R.J. Jackman, O. Cherniavskaya, J.C. McDonald, H. Wu, S.H. Whitesides, G.M. Whitesides, Fabrication of topologically complex three-dimensional microfluidic systems in PDMS by rapid prototyping, Analytical chemistry 72(14) (2000) 3158-3164.
[46] R. Rodrigues, R. Lima, H. Gomes, A. Silva, Polymer microfluidic devices: an overview of fabrication methods, U.Porto Journal of Engineering 1 (2017) 67-79. https://doi.org/10.24840/2183-6493_001.001_0007.
[47] I.R. Ausri, E.M. Feygin, C.Q. Cheng, Y. Wang, Z.W. Lin, X.S. Tang, A highly efficient and antifouling microfluidic platform for portable hemodialysis devices, MRS Communications 8(2) (2018) 474-479.
[48] J.-B. Fan, J. Luo, Z. Luo, Y. Song, Z. Wang, J. Meng, B. Wang, S. Zhang, Z. Zheng, X. Chen, Bioinspired microfluidic device by integrating a porous membrane and heterostructured nanoporous particles for biomolecule cleaning, ACS nano 13(7) (2019) 8374-8381.
[49] F. Li, P. Smejkal, N.P. Macdonald, R.M. Guijt, M.C. Breadmore, One-step fabrication of a microfluidic device with an integrated membrane and embedded reagents by multimaterial 3D printing, Analytical chemistry 89(8) (2017) 4701-4707.
[50] I.S. Ngene, R.G. Lammertink, M. Wessling, W. van der Meer, A microfluidic membrane chip for in situ fouling characterization, Journal of membrane science 346(1) (2010) 202-207.
[51] S. Grilli, S. Coppola, V. Vespini, V. Pagliarulo, G. Nasti, C. Carfagna, P. Ferraro, One-step fabrication of free-standing flexible membranes reinforced with self-assembled arrays of carbon nanotubes, Applied Physics Letters 105(15) (2014) 153101.
[52] S. Coppola, G. Nasti, V. Vespini, L. Mecozzi, R. Castaldo, G. Gentile, M. Ventre, P.A. Netti, P. Ferraro, Quick liquid packaging: Encasing water silhouettes by three-dimensional polymer membranes, Science advances 5(5) (2019) eaat5189.
[53] I. Bouhid de Aguiar, K. Schroën, Microfluidics Used as a Tool to Understand and Optimize Membrane Filtration Processes, Membranes 10(11) (2020) 316.
[54] A. Gerami, Y. Alzahid, P. Mostaghimi, N. Kashaninejad, F. Kazemifar, T. Amirian, N. Mosavat, M.E. Warkiani, R.T. Armstrong, Microfluidics for porous systems: fabrication, microscopy and applications, Transport in Porous Media 130(1) (2019) 277-304.
[55] N. Debnath, M. Sadrzadeh, Microfluidic mimic for colloid membrane filtration: a review, Journal of the Indian Institute of Science 98(2) (2018) 137-157.
[56] G.S. Fiorini, D.T. Chiu, Disposable microfluidic devices: fabrication, function, and application, BioTechniques 38(3) (2005) 429-446.

[57] H. Xu, K. Xiao, X. Wang, S. Liang, C. Wei, X. Wen, X. Huang, Outlining the Roles of Membrane-Foulant and Foulant-Foulant Interactions in Organic Fouling During Microfiltration and Ultrafiltration: A Mini-Review, Frontiers in Chemistry 8(June) (2020) 1--14. https://doi.org/10.3389/fchem.2020.00417.
[58] D.J. Kukulka, R. Baier, J. Mollendorf, Factors associated with fouling in the process industry, Heat transfer engineering 25(5) (2004) 23-29.
[59] L. Song, M. Elimelech, Theory of concentration polarization in crossflow filtration, Journal of the Chemical Society, Faraday Transactions 91(19) (1995) 3389-3398.
[60] C. Completo, V. Semiao, V. Geraldes, Efficient CFD-based method for designing cross-flow nanofiltration small devices, Journal of Membrane Science 500 (2016) 190-202.
[61] S. Sablani, M. Goosen, R. Al-Belushi, M. Wilf, Concentration polarization in ultrafiltration and reverse osmosis: a critical review, Desalination 141(3) (2001) 269-289.
[62] J. Zhan, Z. Liu, B. Wang, F. Ding, Modification of a membrane surface charge by a low temperature plasma induced grafting reaction and its application to reduce membrane fouling, Separation science and technology 39(13) (2004) 2977-2995.
[63] H. Cai, H. Fan, L. Zhao, H. Hong, L. Shen, Y. He, H. Lin, J. Chen, Effects of surface charge on interfacial interactions related to membrane fouling in a submerged membrane bioreactor based on thermodynamic analysis, Journal of colloid and interface science 465 (2016) 33-41.
[64] X. You, J. Teng, Y. Chen, Y. Long, G. Yu, L. Shen, H. Lin, New insights into membrane fouling by alginate: Impacts of ionic strength in presence of calcium ions, Chemosphere 246 (2020) 125801.
[65] K. Xiao, X. Wang, X. Huang, T.D. Waite, X. Wen, Combined effect of membrane and foulant hydrophobicity and surface charge on adsorptive fouling during microfiltration, Journal of Membrane Science 373(1-2) (2011) 140-151.
[66] R.M. McDonogh, C.J. Fell, A.G. Fane, Surface charge and permeability in the ultrafiltration of non-flocculating colloids, Journal of Membrane Science 21(3) (1984) 285-294.
[67] J.W. Chew, J. Kilduff, G. Belfort, The behavior of suspensions and macromolecular solutions in crossflow microfiltration: An update, Journal of Membrane Science 601 (2020) 117865.
[68] C. Henry, J.P. Minier, G. Lefvre, Towards a description of particulate fouling: From single particle deposition to clogging, Advances in Colloid and Interface Science 185-186 (2012) 34--76. https://doi.org/10.1016/j.cis.2012.10.001.
[69] X.-M. Wang, X.-Y. Li, A unified model for quantification of concentration polarization (CP) of particles during cross-flow membrane filtration, Colloids and Surfaces A: Physicochemical and Engineering Aspects 407 (2012) 99-107.
[70] G. Gesan-Guiziou, R.J. Wakeman, G. Daufin, Stability of latex crossflow filtration: Cake properties and critical conditions of deposition, Chemical

Engineering Journal 85(1) (2002) 27--34. https://doi.org/10.1016/S1385-8947(01)00149-8.
[71] Y. Jiao, C. Zhao, Y. Kang, C. Yang, Microfluidics-based fundamental characterization of external concentration polarization in forward osmosis, Microfluidics and Nanofluidics 23(3) (2019) 1-10.
[72] R.R. Bhave, Cross-flow filtration, Fermentation and biochemical engineering handbook, Elsevier1996, pp. 271-347.
[73] Y. Kaufman, R. Kasher, R.G. Lammertink, V. Freger, Microfluidic NF/RO separation: Cell design, performance and application, Journal of membrane science 396 (2012) 67-73.
[74] C. Completo, V. Geraldes, V. Semião, M. Mateus, M. Rodrigues, Comparison between microfluidic tangential flow nanofiltration and centrifugal nanofiltration for the concentration of small-volume samples, Journal of Membrane Science 578 (2019) 27-35.
[75] J. De Jong, R.G. Lammertink, M. Wessling, Membranes and microfluidics: a review, Lab on a Chip 6(9) (2006) 1125-1139.
[76] S.Y. Jung, J.E. Park, T.G. Kang, K.H. Ahn, Design optimization for a microfluidic crossflow filtration system incorporating a micromixer, Micromachines 10(12) (2019) 836.
[77] L.J. Zeman, Adsorption effects in rejection of macromolecules by ultrafiltration membranes, Journal of membrane science 15(3) (1983) 213-230.
[78] Y. Xin, M.W. Bligh, A.S. Kinsela, Y. Wang, T.D. Waite, Calcium-mediated polysaccharide gel formation and breakage: Impact on membrane foulant hydraulic properties, Journal of Membrane Science 475 (2015) 395-405.
[79] J.A. Howell, Sub-critical flux operation of microfiltration, Journal of membrane science 107(1-2) (1995) 165-171.
[80] V. Chen, A. Fane, S. Madaeni, I. Wenten, Particle deposition during membrane filtration of colloids: transition between concentration polarization and cake formation, Journal of Membrane Science 125(1) (1997) 109-122.
[81] R.W. Field, D. Wu, J.A. Howell, B.B. Gupta, Critical flux concept for microfiltration fouling, Journal of Membrane Science 100(3) (1995) 259--272. https://doi.org/10.1016/0376-7388(94)00265-Z.
[82] K. Lucas, S.D. Ahmad, M. Dehghani, T. Gaborski, J. McGrath, Critical flux behavior of ultrathin membranes in protein-rich solutions, Separation and Purification Technology 251 (2020) 117342.
[83] R. van Zwieten, T. Van De Laar, J. Sprakel, K. Schroën, From cooperative to uncorrelated clogging in cross-flow microfluidic membranes, Scientific reports 8(1) (2018) 1-10.
[84] D. Chandler, Interfaces and the driving force of hydrophobic assembly, Nature 437(7059) (2005) 640-647.

[85] X. Shi, G. Tal, N.P. Hankins, V. Gitis, Fouling and cleaning of ultrafiltration membranes: A review, Journal of Water Process Engineering 1 (2014) 121--138. https://doi.org/10.1016/j.jwpe.2014.04.003.
[86] J. Hanemaaijer, T. Robbertsen, T. Van den Boomgaard, J. Gunnink, Fouling of ultrafiltration membranes. The role of protein adsorption and salt precipitation, Journal of Membrane Science 40(2) (1989) 199-217.
[87] J. Zheng, Z. Wang, J. Ma, S. Xu, Z. Wu, Development of an electrochemical ceramic membrane filtration system for efficient contaminant removal from waters, Environmental science & technology 52(7) (2018) 4117-4126.
[88] S. Mu, S. Wang, S. Liang, K. Xiao, H. Fan, B. Han, C. Liu, X. Wang, X. Huang, Effect of the relative degree of foulant "hydrophobicity" on membrane fouling, Journal of Membrane Science 570 (2019) 1-8.
[89] C.-C. Ho, A.L. Zydney, Effect of membrane morphology on the initial rate of protein fouling during microfiltration, Journal of Membrane Science 155(2) (1999) 261-275.
[90] S.S. Massenburg, Clogging Mechanisms in Converging Microchannels, 2016.
[91] S.S. Massenburg, E. Amstad, D.A. Weitz, Clogging in parallelized tapered microfluidic channels, Microfluidics and Nanofluidics 20(6) (2016) 1-5.
[92] J.C. Chen, Q. Li, M. Elimelech, In situ monitoring techniques for concentration polarization and fouling phenomena in membrane filtration, Advances in Colloid and Interface Science 107(2-3) (2004) 83-108.
[93] K. Xiao, Y. Shen, X. Huang, An analytical model for membrane fouling evolution associated with gel layer growth during constant pressure stirred dead-end filtration, Journal of membrane science 427 (2013) 139-149.
[94] W. Russel, D. Saville, W. Schowalter, Colloidal Dispersions Cambridge Univ, Press Cambridge, 1989.
[95] Q. Lei, M. Zhang, L. Shen, R. Li, B.-Q. Liao, H. Lin, A novel insight into membrane fouling mechanism regarding gel layer filtration: Flory-Huggins based filtration mechanism, Scientific reports 6(1) (2016) 1-9.
[96] J. Linkhorst, T. Beckmann, D. Go, A.J. Kuehne, M. Wessling, Microfluidic colloid filtration, Scientific reports 6(1) (2016) 1-8.
[97] H. Hong, M. Zhang, Y. He, J. Chen, H. Lin, Fouling mechanisms of gel layer in a submerged membrane bioreactor, Bioresource technology 166 (2014) 295-302.
[98] M.L. Mokrane, T. Desclaux, J.F. Morris, P. Joseph, O. Liot, Microstructure of the near-wall layer of filtration-induced colloidal assembly, Soft Matter 16(42) (2020) 9726-9737.
[99] E. Arkhangelsky, F. Wicaksana, C. Tang, A.A. Al-Rabiah, S.M. Al-Zahrani, R. Wang, Combined organic–inorganic fouling of forward osmosis hollow fiber membranes, water research 46(19) (2012) 6329-6338.
[100] Y. Jeong, Y. Kim, Y. Jin, S. Hong, C. Park, Comparison of filtration and treatment performance between polymeric and ceramic membranes in anaerobic

membrane bioreactor treatment of domestic wastewater, Separation and Purification Technology 199 (2018) 182-188.
[101] T. Headen, S. Clarke, A. Perdigon, G. Meeten, J. Sherwood, M. Aston, Filtration of deformable emulsion droplets, Journal of colloid and interface science 304(2) (2006) 562-565.
[102] B. de Aguiar Izabella, M. Martine, B. Antoine, S. Karin, Microfluidic model systems used to emulate processes occurring during soft particle filtration, Scientific Reports (Nature Publisher Group) 9(1) (2019).
[103] W.G. Characklis, K.E. Cooksey, Biofilms and microbial fouling, Advances in applied microbiology 29 (1983) 93-138.
[104] L.D. Chambers, K.R. Stokes, F.C. Walsh, R.J. Wood, Modern approaches to marine antifouling coatings, Surface and Coatings Technology 201(6) (2006) 3642-3652.
[105] I. Biswas, A. Kumar, M. Sadrzadeh, Microfluidic Membrane Filtration Systems to Study Biofouling, Microfluidics and Nanofluidics (2018) 293.
[106] H.-C. Flemming, Biofouling and me: My Stockholm syndrome with biofilms, Water research 173 (2020) 115576.
[107] P. Stoodley, Z. Lewandowski, J.D. Boyle, H.M. Lappin-Scott, Oscillation characteristics of biofilm streamers in turbulent flowing water as related to drag and pressure drop, Biotechnology and bioengineering 57(5) (1998) 536-544.
[108] A. Marty, C. Roques, C. Causserand, P. Bacchin, Formation of bacterial streamers during filtration in microfluidic systems, Biofouling 28(6) (2012) 551-562.
[109] V. Brião, C. Tavares, Pore blocking mechanism for the recovery of milk solids from dairy wastewater by ultrafiltration, Brazilian Journal of Chemical Engineering 29(2) (2012) 393-407.
[110] H. Darcy, Les fontaines publiques de la ville de Dijon: exposition et application, Victor Dalmont1856.
[111] E.-E. Chang, S.-Y. Yang, C.-P. Huang, C.-H. Liang, P.-C. Chiang, Assessing the fouling mechanisms of high-pressure nanofiltration membrane using the modified Hermia model and the resistance-in-series model, Separation and Purification Technology 79(3) (2011) 329-336.
[112] W. Bowen, J. Calvo, A. Hernandez, Steps of membrane blocking in flux decline during protein microfiltration, Journal of Membrane Science 101(1-2) (1995) 153-165.
[113] E.M. Tracey, R.H. Davis, Protein fouling of track-etched polycarbonate microfiltration membranes, Journal of Colloid and Interface Science 167(1) (1994) 104-116.
[114] E. Iritani, A Review on Modeling of Pore-Blocking Behaviors of Membranes During Pressurized Membrane Filtration, Drying Technology 31(2) (2013) 146--162. https://doi.org/10.1080/07373937.2012.683123.
[115] P. Hermans, Principles of the mathematical treatment of constant-pressure filtration, J. Soc. Chem. Ind. 55 (1936) 1.

[116] H. Grace, Structure and performance of filter media. II. Performance of filter media in liquid service, AIChE Journal 2(3) (1956) 316-336.
[117] J. Hermia, Constant pressure blocking filtration laws: application to power-law non-Newtonian fluids, (1982).
[118] M.C.V. Vela, S.Á. Blanco, J.L. García, E.B. Rodríguez, Analysis of membrane pore blocking models adapted to crossflow ultrafiltration in the ultrafiltration of PEG, Chemical Engineering Journal 149(1-3) (2009) 232-241.
[119] S. Todisco, L. Pena, E. Drioli, P. Tallarico, Analysis of the fouling mechanism in microfiltration of orange juice, Journal of food processing and preservation 20(6) (1996) 453-466.
[120] C.-C. Ho, A.L. Zydney, A combined pore blockage and cake filtration model for protein fouling during microfiltration, Journal of colloid and interface science 232(2) (2000) 389-399.
[121] G. Bolton, D. LaCasse, R. Kuriyel, Combined models of membrane fouling: development and application to microfiltration and ultrafiltration of biological fluids, Journal of Membrane Science 277(1-2) (2006) 75-84.
[122] L. Hou, Z. Wang, P. Song, A precise combined complete blocking and cake filtration model for describing the flux variation in membrane filtration process with BSA solution, 2017, pp. 186--194.
[123] C. Güell, M. Ferrando, F. López, Monitoring and visualizing membrane-based processes, Wiley Online Library2009.
[124] G. Rudolph, T. Virtanen, M. Ferrando, C. Gell, F. Lipnizki, M. Kallioinen, A review of in situ real-time monitoring techniques for membrane fouling in the biotechnology, biorefinery and food sectors, Journal of Membrane Science 588(July) (2019) 117221. https://doi.org/10.1016/j.memsci.2019.117221.
[125] A. Fane, P. Beatson, H. Li, Membrane fouling and its control in environmental applications, Water science and technology 41(10-11) (2000) 303-308.
[126] R.O. Wayne, Light and video microscopy, Academic Press2019.
[127] G. Parker, Encyclopedia of materials: science and technology, (2001).
[128] A. Perazzo, L. Sicignano, G. Tomaiuolo, R. Marotta, R. Andreozzi, S. Guido, Tuning crystal structure in a micro-scale reactive flow, Chemical Engineering Science 207 (2019) 581-587.
[129] L. Sicignano, G. Tomaiuolo, A. Perazzo, S.P. Nolan, P.L. Maffettone, S. Guido, The effect of shear flow on microreactor clogging, Chemical Engineering Journal 341 (2018) 639-647.
[130] H.M. Wyss, D.L. Blair, J.F. Morris, H.A. Stone, D.A. Weitz, Mechanism for clogging of microchannels, Physical review E 74(6) (2006) 061402.
[131] B. Dersoir, M.R. de Saint Vincent, M. Abkarian, H. Tabuteau, Clogging of a single pore by colloidal particles, Microfluidics and Nanofluidics 19(4) (2015) 953-961.

[132] I. Bouhid de Aguiar, M. Meireles, A. Bouchoux, K. Schroën, Microfluidic model systems used to emulate processes occurring during soft particle filtration, Scientific Reports (Nature Publisher Group) 9(1) (2019).
[133] M.E. Warkiani, F. Wicaksana, A.G. Fane, H.-Q. Gong, Investigation of membrane fouling at the microscale using isopore filters, Microfluidics and Nanofluidics 19(2) (2015) 307-315.
[134] A.D. McNaught, A. Wilkinson, Compendium of chemical terminology, Blackwell Science Oxford1997.
[135] K.B. Neeves, S.L. Diamond, A membrane-based microfluidic device for controlling the flux of platelet agonists into flowing blood, Lab on a Chip 8(5) (2008) 701-709.
[136] M. Dehghani, K. Lucas, J. Flax, J. McGrath, T. Gaborski, Tangential flow microfluidics for the capture and release of nanoparticles and extracellular vesicles on conventional and ultrathin membranes, Advanced materials technologies 4(11) (2019) 1900539.
[137] P. Bacchin, D. Snisarenko, D. Stamatialis, P. Aimar, C. Causserand, Combining fluorescence and permeability measurements in a membrane microfluidic device to study protein sorption mechanisms, Journal of Membrane Science 614 (2020) 118485.
[138] J.W. Lichtman, J.-A. Conchello, Fluorescence microscopy, Nature methods 2(12) (2005) 910-919.
[139] L.H. Greene, J.A. Grobler, V.A. Malinovskii, J. Tian, K.R. Acharya, K. Brew, Stability, activity and flexibility in α-lactalbumin, Protein engineering 12(7) (1999) 581-587.
[140] M. Van Audenhaege, S. Pezennec, G. Gesan-Guiziou, Ultrafiltration membrane cut-off impacts structure and functional properties of transmitted proteins: Case study of the metalloprotein α-lactalbumin, Separation and Purification Technology 114 (2013) 73-82.
[141] J. Pawley, Handbook of biological confocal microscopy, Springer Science & Business Media2006.
[142] M. Muller, Introduction to confocal fluorescence microscopy, SPIE press2006.
[143] H. Di, G.J. Martin, D.E. Dunstan, A microfluidic system for studying particle deposition during ultrafiltration, Journal of Membrane Science 532 (2017) 68-75.
[144] M. Mukherjee, N.V. Menon, X. Liu, Y. Kang, B. Cao, Confocal laser scanning microscopy-compatible microfluidic membrane flow cell as a nondestructive tool for studying biofouling dynamics on forward osmosis membranes, Environmental Science & Technology Letters 3(8) (2016) 303-309.
[145] P.H. Tomlins, R.K. Wang, Theory, developments and applications of optical coherence tomography, Journal of Physics D: Applied Physics 38(15) (2005) 2519.
[146] S. Aumann, S. Donner, J. Fischer, F. Müller, Optical coherence tomography (OCT): Principle and technical realization, High Resolution Imaging in Microscopy and Ophthalmology (2019) 59-85.

[147] W. Li, X. Liu, Y.-N. Wang, T.H. Chong, C.Y. Tang, A.G. Fane, Analyzing the evolution of membrane fouling via a novel method based on 3D optical coherence tomography imaging, Environmental science & technology 50(13) (2016) 6930-6939.
[148] C. Haisch, R. Niessner, Visualisation of transient processes in biofilms by optical coherence tomography, Water Research 41(11) (2007) 2467-2472.
[149] C. Dreszer, A.D. Wexler, S. Drusová, T. Overdijk, A. Zwijnenburg, H.-C. Flemming, J.C. Kruithof, J.S. Vrouwenvelder, In-situ biofilm characterization in membrane systems using Optical Coherence Tomography: Formation, structure, detachment and impact of flux change, water research 67 (2014) 243-254.
[150] S. Park, T. Nam, J. Park, S. Kim, Y. Ahn, S. Lee, Y.M. Kim, W. Jung, K.H. Cho, Investigating the influence of organic matter composition on biofilm volumes in reverse osmosis using optical coherence tomography, Desalination 419 (2017) 125-132.
[151] J. Qian, H. Horn, J. Tarchitzky, Y. Chen, S. Katz, M. Wagner, Water quality and daily temperature cycle affect biofilm formation in drip irrigation devices revealed by optical coherence tomography, Biofouling 33(3) (2017) 211-221.
[152] N. Weiss, K.E.T. El Obied, J. Kalkman, R.G. Lammertink, T.G. van Leeuwen, Measurement of biofilm growth and local hydrodynamics using optical coherence tomography, Biomedical optics express 7(9) (2016) 3508-3518.
[153] Y. Gao, S. Haavisto, W. Li, C.Y. Tang, J. Salmela, A.G. Fane, Novel approach to characterizing the growth of a fouling layer during membrane filtration via optical coherence tomography, Environmental science & technology 48(24) (2014) 14273-14281.
[154] J.B. Lambert, E.P. Mazzola, C.D. Ridge, Nuclear magnetic resonance spectroscopy: an introduction to principles, applications, and experimental methods, John Wiley & Sons2019.
[155] B. Hammer, C. Heath, S. Mirer, G. Belfort, Quantitative flow measurements in bioreactors by NMR Imaging, Nature biotechnology 13 (1995) 303-308.
[156] M. Wiese, S. Benders, B. Blümich, M. Wessling, 3D MRI velocimetry of non-transparent 3D-printed staggered herringbone mixers, Chemical Engineering Journal 343 (2018) 54-60.
[157] R.A. Al-Juboori, T. Yusaf, Biofouling in RO system: mechanisms, monitoring and controlling, Desalination 302 (2012) 1-23.
[158] S. Buetehorn, L. Utiu, M. Küppers, B. Blümich, T. Wintgens, M. Wessling, T. Melin, NMR imaging of local cumulative permeate flux and local cake growth in submerged microfiltration processes, Journal of Membrane Science 371(1-2) (2011) 52-64.
[159] M. Wiese, C. Malkomes, B. Krause, M. Wessling, Flow and filtration imaging of single use sterile membrane filters, Journal of Membrane Science 552 (2018) 274-285.

[160] H.-Y. Chen, R. Tycko, Low-temperature magnetic resonance imaging with 2.8 μm isotropic resolution, Journal of Magnetic Resonance 287 (2018) 47-55.
[161] E.E. McDonnell, S. Han, C. Hilty, K.L. Pierce, A. Pines, NMR analysis on microfluidic devices by remote detection, Analytical chemistry 77(24) (2005) 8109-8114.
[162] J. Paulsen, V.S. Bajaj, A. Pines, Compressed sensing of remotely detected MRI velocimetry in microfluidics, Journal of Magnetic Resonance 205(2) (2010) 196-201.
[163] V.S. Bajaj, J. Paulsen, E. Harel, A. Pines, Zooming in on microscopic flow by remotely detected MRI, Science 330(6007) (2010) 1078-1081.
[164] P.Z. Çulfaz, S. Buetehorn, L. Utiu, M. Kueppers, B. Bluemich, T. Melin, M. Wessling, R.G. Lammertink, Fouling behavior of microstructured hollow fiber membranes in dead-end filtrations: critical flux determination and NMR imaging of particle deposition, Langmuir 27(5) (2011) 1643-1652.
[165] F. Arndt, S. Schuhmann, G. Guthausen, S. Schütz, H. Nirschl, In situ MRI of alginate fouling and flow in ceramic hollow fiber membranes, Journal of Membrane Science 524 (2017) 691-699.
[166] L. Cui, M. Yao, B. Ren, K.-S. Zhang, Sensitive and versatile detection of the fouling process and fouling propensity of proteins on polyvinylidene fluoride membranes via surface-enhanced Raman spectroscopy, Analytical chemistry 83(5) (2011) 1709-1716.
[167] T. Virtanen, S.-P. Reinikainen, M. Kögler, M. Mänttäri, T. Viitala, M. Kallioinen, Real-time fouling monitoring with Raman spectroscopy, Journal of Membrane Science 525 (2017) 312-319.
[168] O.D. Supekar, J.J. Brown, A.R. Greenberg, J.T. Gopinath, V.M. Bright, Real-time detection of reverse-osmosis membrane scaling via Raman spectroscopy, Industrial & Engineering Chemistry Research 57(47) (2018) 16021-16026.
[169] J.R. Ferraro, Introductory raman spectroscopy, Elsevier2003.
[170] C. De Rosa, F. Auriemma, C. Diletto, R. Di Girolamo, A. Malafronte, P. Morvillo, G. Zito, G. Rusciano, G. Pesce, A. Sasso, Toward hyperuniform disordered plasmonic nanostructures for reproducible surface-enhanced Raman spectroscopy, Physical Chemistry Chemical Physics 17(12) (2015) 8061-8069.
[171] M. Kögler, B. Zhang, L. Cui, Y. Shi, M. Yliperttula, T. Laaksonen, T. Viitala, K. Zhang, Real-time Raman based approach for identification of biofouling, Sensors and Actuators B: Chemical 230 (2016) 411-421.
[172] K.-W. Chang, H.-W. Cheng, J. Shiue, J.-K. Wang, Y.-L. Wang, N.-T. Huang, Antibiotic susceptibility test with surface-enhanced Raman scattering in a microfluidic system, Analytical chemistry 91(17) (2019) 10988-10995.
[173] B. Krafft, R. Panneerselvam, D. Geissler, D. Belder, A microfluidic device enabling surface-enhanced Raman spectroscopy at chip-integrated multifunctional nanoporous membranes, Analytical and bioanalytical chemistry 412(2) (2020) 267-277.

[174] D. Titus, E.J.J. Samuel, S.M. Roopan, Nanoparticle characterization techniques, Green Synthesis, Characterization and Applications of Nanoparticles, Elsevier2019, pp. 303-319.
[175] M. Taha, M. Hassan, S. Essa, Y. Tartor, Use of Fourier transform infrared spectroscopy (FTIR) spectroscopy for rapid and accurate identification of Yeasts isolated from human and animals, International journal of veterinary science and medicine 1(1) (2013) 15-20.
[176] P.S. Stewart, M.J. Franklin, Physiological heterogeneity in biofilms, Nature Reviews Microbiology 6(3) (2008) 199-210.
[177] S.G. Kazarian, Enhancing high-throughput technology and microfluidics with FTIR spectroscopic imaging, Analytical and bioanalytical chemistry 388(3) (2007) 529-532.
[178] H.-Y.N. Holman, R. Miles, Z. Hao, E. Wozei, L.M. Anderson, H. Yang, Real-time chemical imaging of bacterial activity in biofilms using open-channel microfluidics and synchrotron FTIR spectromicroscopy, Analytical chemistry 81(20) (2009) 8564-8570.
[179] K.A. Chan, X. Niu, A.J. de Mello, S.G. Kazarian, Rapid prototyping of microfluidic devices for integrating with FT-IR spectroscopic imaging, Lab on a Chip 10(16) (2010) 2170-2174.
[180] K.A. Chan, S.G. Kazarian, Aberration-free FTIR spectroscopic imaging of live cells in microfluidic devices, Analyst 138(14) (2013) 4040-4047.
[181] R. Chan, V. Chen, Characterization of protein fouling on membranes: opportunities and challenges, Journal of Membrane Science 242(1-2) (2004) 169-188.
[182] Y. Wyart, G. Georges, C. Deumie, C. Amra, P. Moulin, Membrane characterization by optical methods: Ellipsometry of the scattered field, Journal of Membrane Science 318(1-2) (2008) 145-153.
[183] E. Kondoh, K. Segawa, L. Jin, S. Hamada, S. Shima, H. Hiyama, Flat-shaped microfluidic optical cell for in situ ellipsometry using glass slide as optical window component, Japanese Journal of Applied Physics 57(7S2) (2018) 07MD01.
[184] A. Romanenko, B. Kalas, P. Hermann, O. Hakkel, L. Illés, M.s. Fried, P. Fürjes, G. Gyulai, P. Petrik, Membrane-Based In Situ Mid-Infrared Spectroscopic Ellipsometry: A Study on the Membrane Affinity of Polylactide-co-glycolide Nanoparticulate Systems, Analytical Chemistry (2020).
[185] D.L. Huber, R.P. Manginell, M.A. Samara, B.-I. Kim, B.C. Bunker, Programmed adsorption and release of proteins in a microfluidic device, Science 301(5631) (2003) 352-354.
[186] S.L. Peterson, A. McDonald, P.L. Gourley, D.Y. Sasaki, Poly (dimethylsiloxane) thin films as biocompatible coatings for microfluidic devices: cell culture and flow studies with glial cells, Journal of Biomedical Materials Research Part A: An Official Journal of The Society for Biomaterials, The Japanese

Society for Biomaterials, and The Australian Society for Biomaterials and the Korean Society for Biomaterials 72(1) (2005) 10-18.
[187] A. Yeo, P. Yang, A. Fane, T. White, H. Moser, Non-invasive observation of external and internal deposition during membrane filtration by X-ray microimaging (XMI), Journal of membrane science 250(1-2) (2005) 189-193.
[188] S.-J. Lee, G.B. Kim, Synchrotron microimaging technique for measuring the velocity fields of real blood flows, Journal of Applied Physics 97(6) (2005) 064701.
[189] S.J. Lee, J.K. Huh, G.B. Kim, Measurements of Flow inside Microchannels Using Micro-PIV and X-ray Micro-imaging Techniques, APS Division of Fluid Dynamics Meeting Abstracts, 2001, p. JQ. 006.
[190] S.J. Lee, G. Kim, S. Kim, Y. Kim, H. Yoon, X-ray micro-imaging of flows in opaque conduits, Journal of visualization 10(1) (2007) 29-32.
[191] Y. Xu-Jiang, J. Dodds, D. Leclerc, Cake characteristics in crossflow and dead-end microfiltration, Filtration & separation 32(8) (1995) 795-798.
[192] Q. She, C.Y. Tang, Y.-N. Wang, Z. Zhang, The role of hydrodynamic conditions and solution chemistry on protein fouling during ultrafiltration, Desalination 249(3) (2009) 1079-1087.
[193] B. Boissier, F. Lutin, M. Moutounet, A. Vernhet, Particles deposition during the cross-flow microfiltration of red wines—incidence of the hydrodynamic conditions and of the yeast to fines ratio, Chemical Engineering and Processing: Process Intensification 47(3) (2008) 276-286.
[194] J. Haberkamp, M. Ernst, G. Makdissy, P.M. Huck, M. Jekel, Protein fouling of ultrafiltration membranes—investigation of several factors relevant for tertiary wastewater treatment, Journal of environmental engineering and science 7(6) (2008) 651-660.
[195] K. Abel, Influence of oscillatory flows on protein ultrafiltration, Journal of membrane science 133(1) (1997) 39-55.
[196] M.E. Weinberger, U. Kulozik, On the effect of flow reversal during crossflow microfiltration of a cell and protein mixture, Food and Bioproducts Processing 129 (2021) 24-33.
[197] M.E. Weinberger, U. Kulozik, Pulsatile crossflow improves microfiltration fractionation of cells and proteins, Journal of Membrane Science 629 (2021) 119295.
[198] R. Ouseph, R.A. Ward, Increasing dialysate flow rate increases dialyzer urea mass transfer-area coefficients during clinical use, American journal of kidney diseases 37(2) (2001) 316-320.
[199] R. Jalab, A.M. Awad, M.S. Nasser, J. Minier-Matar, S. Adham, Pilot-scale investigation of flowrate and temperature influence on the performance of hollow fiber forward osmosis membrane in osmotic concentration process, Journal of Environmental Chemical Engineering 8(6) (2020) 104494.
[200] R.R. Ferlita, D. Phipps, J. Safarik, D.H. Yeh, Cryo-snap: A simple modified freeze-fracture method for SEM imaging of membrane cross-sections, Environmental Progress 27(2) (2008) 204-209.

[201] S.T. Kelly, W.S. Opong, A.L. Zydney, The influence of protein aggregates on the fouling of microfiltration membranes during stirred cell filtration, Journal of membrane science 80(1) (1993) 175-187.
[202] W. Wang, C.J. Roberts, Protein aggregation–mechanisms, detection, and control, International journal of pharmaceutics 550(1-2) (2018) 251-268.

Chapter 2

Fouling Mitigation Strategies

Chapter Contents

1. Introduction

Due to the severe impact of fouling on membrane processes throughput, several strategies have been developed to mitigate solutes deposition by acting on the various interactions characterizing fouling itself. Different authors have listed a series of approaches to mitigate membrane fouling. According to Jagannadh et al., concentration polarization and membrane fouling can be mitigated by controlling the boundary layer, inducing turbulence, modifying the membrane or by combined external electric fields, whose application induces electrophoresis, electrolysis and ion migration, improving process performance [1]. Other techniques, such as feed pretreatment, flow manipulation and gas sparging were instead reviewed by Williams et al. [2].

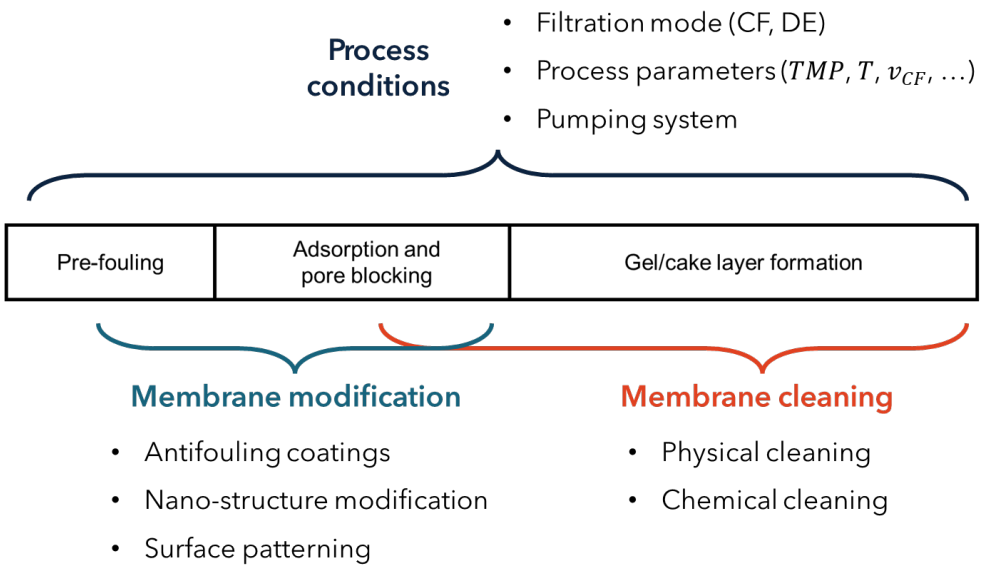

***Figure 1**. Categorization of membrane fouling mitigation strategies based on fouling evolution stages.*

Considering the various fouling stages – i.e., pre-fouling, adsorption and pore blocking and cake formation, mitigation strategies can be conveniently grouped into three main categories, as summarized in Figure 1. The first one concerns the optimization of process conditions such as transmembrane pressure and filtration mode and affects all the stages of fouling evolution. Physical and chemical

membrane cleaning constitute the second category. These two techniques specifically interest the last two stages as solutes are removed and degraded after they have adsorbed and deposited forming a cake layer. The last group concerns the modification of the membrane to prevent fouling by chemically repelling solutes or creating specific flow patterns that reduce deposition extent. In such a manner, membrane modification directly acts on the first two stages of fouling, hindering concentration polarization and adsorption phenomena.

In the following section, the presented categories will be reviewed, with particular attention to membrane functionalization, which was experimentally investigated as a mitigation approach for protein fouling in microfluidic filtration systems.

2. Process Conditions Optimization

The optimization of the process conditions represents one of the most required ways of reducing membrane fouling, owing to the related savings in terms of both capital and maintenance costs.

Fouling mitigation can be first realized by selecting the appropriate filtration mode. While dead-end filtration is preferred for higher process throughput, crossflow filtration is often used for severely fouling feeds. As a matter of fact, the presence of the tangential flow is associated with the generation of lift forces, which are produced by the velocity gradient near the wall [3, 4]. Under such forces, foulants are hydrodynamically carried away from the membrane surface, resulting in reduced concentration polarization and consequentially solutes deposition. The presence of a tangential flow on the membrane surface was also found to affect both cake layer porosity and compressibility, playing a role in the growth of the cake itself [5].

Hydrodynamic conditions, such as transmembrane pressure and crossflow velocity, impact fouling development as well [6-8]. According to the work of She et al. increasing applied pressure negatively impacts on process performances since, due to the higher initial fluxes, a greater amount of solute is brought to the membrane surface. Being the main driving force of filtration processes like micro, ultra and nanofiltration, transmembrane pressure is also intimately related to the concept of *critical flux*, a flux value below which no decline is observed due to a marginal extent of solutes deposition [9, 10]. Operating below the critical flux value allows, therefore, to minimize stops while keeping high throughput.

Temperature is another relevant parameter for the evolution of fouling. Depending on the foulant nature, a higher temperature may result in increased fouling rates or not. Indeed, crystallization and particulate deposition are enhanced at higher process temperatures due to the higher adsorption and growth

reaction rates [11]. Biofouling is instead favored in a temperature range between 30 and 40°C, which represents the best condition for microorganisms to proliferate. Protein fouling is negatively affected by higher temperatures as well, due to the occurrence of denaturation processes which lead to protein aggregation and the formation of clusters that may clog pores [12].

Finally, as described in *Chapter 1: Fouling Phenomena*, fouling evolution can be affected by the pumping system used to process the feed solution, especially when dealing with protein solutions. In fact, the high shear stresses generated by the apparatus mechanics can set off denaturation, which in turn triggers adsorption and clogging processes [13].

3. Membrane Cleaning

3.1. Physical Cleaning

Membrane physical cleaning generally includes pneumatic and hydraulic methods, sonication and mechanical cleaning.

3.1.1. Pneumatic cleaning

Pneumatic cleaning is realized by applying air to directly remove deposits on the membrane or enhance permeate flux and is usually termed as air sparging [14]. Such cleaning approach is based on the generation of turbulence fluctuations, together with shear stresses on the membrane surface from the bubble flow. In particular, the introduction of a shear stress has been proven to be a key parameter, as it mechanically removes attached foulants wearing the deposited layer and thus enhances the overall hydraulic permeability [15].

Together with air sparging, backflushing represents a promising technique, especially for internal fouling and cake compaction mitigation. Such approach is realized by pushing air back into the feed stream, therefore unclogging membrane pores and disrupting the cake structure [16]. One of the main advantages of pneumatic cleaning is the low maintenance costs, the ease of integration on existing systems and the absence of chemicals, however in the case of strongly adsorbed foulants its utility may be marginal.

3.1.2. Hydraulic Cleaning

Hydraulic cleaning is the most used technique for fouling mitigation and includes forward and reverse flushing, backwashing and backpulsing. Forward flushing allows foulants removal by inducing a high degree of turbulence on the membrane surface and is carried out by pumping permeate water through the feed side at high crossflow velocity [17]. Such technique is particularly helpful against

colloidal fouling. In reverse flushing, instead, the direction of the permeate flush is alternated at a frequency optimized for the specific process.

Backwashing is realized by periodically pumping permeate flux back through the membrane in the feed side at a higher pressure. Deposited solutes are therefore lifted off the membrane surface, efficiently recovering flux. Indeed, such approach is particularly useful with strongly adhered deposits and to remove foulants from clogged pores, which are flushed inside out. During CF operations in the presence of a cake layer, backwashing determines an increase in the layer thickness, which is eventually washed out by forward flushing [18]. Effective cleaning can be achieved by optimizing backwash pressure and duration, however the former was proved to have a higher impact [19].

Backpulsing is a cyclic process of forward and reverse filtration, or rather a higher rate backwashing. In such technique backpressure is applied at a rapid pulse, allowing effective foulant removal in a similar fashion to backwashing. Despite the promising findings in terms of flux recovery rate, however, backpulsing was not proven to be necessarily ideal for irreversible fouling mitigation [18].

3.1.3. Sonication

In ultrasonic cleaning, a series of high-frequency compaction and rarefaction sound waves are used to dissolve and remove foulants deposited on the membrane surface. By employing high-energy ultrasonic pulses, it is possible to break adsorbed foulants and loosen bacterial biofilms; in addition, concentration polarization is reduced as well, thanks to the higher degree of mixing induced by the propagating ultrasonic waves.

At sufficiently high power, when the sound wave's lower pressure exceeds the attractive forces of the liquid molecules, ultrasounds also lead to the formation of cavitation bubbles. The collapse of such bubbles is extremely fast and has both

chemical and mechanical effects, since pressures up to 200 MPa and temperatures up to 6000 K can be reached [19].

The cleaning efficiency of sonication depends on several factors, such as frequency, power density, duration, irradiation and orientation. Operating conditions, membrane material and foulant nature play a key role as well [20]. Low frequencies have been reported to be associated with higher cleaning efficiencies [21].

3.1.4. Mechanical Cleaning

Mechanical cleaning strategies make use of external equipment to scrape off adhered material when other approaches are not sufficient to restore membrane flux.

Sponge ball cleaning is accomplished by means of spheres typically made of polyurethane foam whose dimensions are slightly bigger than pore's ones in order to avoid unwanted clogging. It is generally used with tubular membranes, in which balls are forced at high velocity, carried by a pressurized fluid. The cleaning action is realized either by filtering the sponge balls through the membrane and collecting them in the permeate, or pushing them back and forth along the membrane tube [22]. Different types of balls are commercially available, each one designed for specific applications. Expanded life balls, for example, are only applied for mild fouling processes, whereas abrasive balls are particularly effective in the case of hard deposits [23]. The removal efficiency of balls depends on various factors, such as size, number, hardness as well as on the duration of the cleaning and the foulant nature.

Fluidized particles, such as glass or steel beads and granulates, allow fouling mitigation by enhancing the convective flow and generating turbulence in the inlet flow ducts or the membrane tank. A higher degree of mixing of the boundary layer on the membrane surface is also achieved, reducing concentration polarization

and removing deposited foulants. The use of fluidized particles is preferred for viscous feeds due to the lower risk of membrane damage at higher velocities [23].

Rotating and vibrating membranes can also be designed to introduce shear components inside the filtration modules and delay fouling. The first commercial vibrating membranes were produced by New Logic Research, Inc..

3.2. Chemical Cleaning

Chemical cleaning is used when severe fouling occurs and represents the main solution to restore a membrane. It is performed through six main steps: bulk reaction of cleaning chemicals, transportation of chemicals to the membrane interface, penetration into the fouling layer, reaction with the foulants and detachment, transport of the waste to the interface and finally to the bulk solution [19]. Chemical cleaning can be carried out in different ways [14]. In *cleaning-in-place* procedures fouled membranes are directly immersed in the cleaning solution; on the other side, in *cleaning-out-of-place* procedures, they are soaked in a separate tank containing highly concentrated chemicals. Cleaning agents can also be added in the feed stream (*chemical wash*), or be used synergically with other physical cleaning approaches (*chemical enhanced backwash*).

Five categories of chemical cleaning agents can be found in literature and include acids, bases, oxidants, surfactants and chelates [21, 24]. The use of acids is highly effective in the removal of precipitated salts both from the membrane surface and from the pore and was reported to be an effective and low cost approach [19]. The most used acids for membrane cleaning are oxalic, citric, nitric, hydrochloric, phosphoric and sulfuric acids. In particular, hydrochloric acid is effective in whey removal, citric and oxalic acid in metal io complexation, whereas citric acid represents a low pH damage risk alternative and provides a buffering action as well [21, 25, 26]. Organic foulants can be easily removed at high pH by means of bases such as sodium hydroxide. As a matter of fact, in these conditions proteins

and carbohydrates are hydrolyzed and solubilized into small molecules, whereas oils reacts through saponification forming soluble and easy to remove micelles [27]. Sodium and potassium hydroxide also allow to regulate pH conditions and hinder membrane-foulant interactions by decreasing the number of bonds between the membrane and the deposits [28]. In the presence of organic and biological foulants, the use of oxidants represents the best cleaning alternative. This approach, however, is limited by the production of toxic by-products and by the risk of damaging the membrane. Surfactants and chelating agents are respectively used for fatty and oily deposits and for organic foulants associated with metal ions. Indeed, the former are able to solubilize macromolecules acting on hydrophobic interactions, whereas the latter can form coordinate bonds capable of loosening the cake layer structure by affecting the intermolecular membrane-foulant bridges [27, 29].

Despite the positive effect in terms of foulant removal, chemical cleaning is often dangerous for the process. Indeed, cleaning agents create harsh conditions not only for the foulants, but also for the membrane, whose characteristics can change negatively. Causserand et al. have reported changes in mechanical strength, surface hydrophilicity, and porosity after exposure to various chemicals [30]. In addition, permeate flux recovery and fouling redevelopment of chemically cleaned membranes may differ from pristine ones [24].

4. Membrane Modification

Membrane modification techniques aim to mitigate fouling by tailoring membrane surface physical and chemical properties. Three different approaches may be distinguished, namely surface functionalization via antifouling coatings and grafted molecules, membrane nano-structure modifications and membrane patterning.

4.1. Membrane Functionalization

Chemical modification of membrane surface with antifouling functionalities to effectively alleviate or even prevent fouling, as well as provide mechanical strength and long-term stability of membranes, is a pressing demand in maintaining the filtration performance and tailoring membranes with desirable properties [31]. Many attempts have been made to increase surface hydrophilicity, since hydrophilic surfaces are able to arrange a buffer layer composed of water molecules and prevent foulants from adhering, which leads to a reduced membrane fouling, as well as a stable and higher water flux [32]. To address the above challenges, a variety of modification techniques for polymer membranes were explored, including blending, surface grafting, layer-by-layer deposition, self-assembled monolayers, plasma treatment, UV irradiation, and so forth [33, 34]. Although widely implemented in research, these methods are still limited for widespread practical use, due to their complexity, to the strictness of the reaction conditions and to the lack of general applicability [33, 35].

Recently, polydopamine (PD) coating has received intensive attention as an attractive strategy for membrane surface modification. Because of the unique properties such as self-polymerization, high anchoring capability and the presence of hydrophilic functional groups, polydopamine can remarkably improve surface hydrophilicity by just forming a very thin layer on any substrate surface [32]. Moreover, grafting other functional materials (such as nanoparticles, oligomers

or polymers) on polydopamine layers can lead to a further improvement of membrane hydrophilicity and selectivity by minimizing the deposition of specific foulants [34].

4.1.1. Polydopamine Coatings

Dopamine (DA) is a biological neurotransmitter that widely exists in living organisms [33]. A dopamine molecule consists of a catechol structure (a benzene ring with two hydroxyl side groups) with one amine group attached via an ethyl chain (Figure 2).

Dopamine monomers are able to undergo polymerization, which starts with the self-oxidation of catechol to quinone in the presence of oxygen as an oxidant, under alkaline conditions. During dopamine polymerization, a tightly adherent polydopamine layer is created on the surface of a substrate that is immersed in the dopamine solution for a certain period of time. The interactions between the polydopamine layer and the substrate include covalent and noncovalent interactions, such as hydrogen bonding interactions, $\pi - \pi$ interactions, and electrostatic interactions [33, 36].

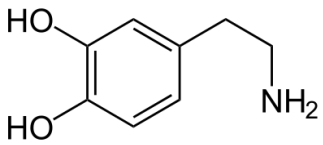

Figure 2. *Dopamine molecule structure*

The use of dopamine as a surface coating stems from research carried out on the composition of the adhesive proteins of mussels, which have a remarkable ability to adhere to any type of surface, organic and inorganic. This adhesive versatility was discovered by investigating the amino acids of the secreted proteins positioned at the plate-substrate interface [35]. This area (Figure 3B and D) is rich in 3,4-dihydroxy-L-phenylanine (DOPA) and lysine (K) amino acids, which together can form a simulative Mefp-5 structure, described in Figure 3D. This compound appears as a powerful building block for the spontaneous deposition

of polymeric films. Therefore, assuming the coexistence of catechol (DOPA) and amine (lysine) groups, present in Mefp-5, dopamine was identified as a compound that contains a double functionality: amino groups and catechol groups (Figure 3E) [35].

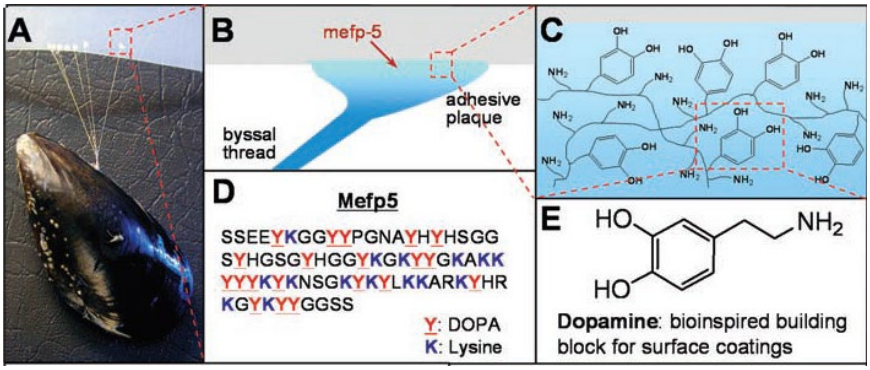

Figure 3. *(**A**) Photograph of a mussel attached to commercial PTFE. (**B** and **C**) Schematic illustrations of the interfacial location of Mefp-5 and a simplified molecular representation of characteristic amine and catechol groups. (**D**) The amino acid sequence of Mefp-5. (**E**) Dopamine contains both amine and catechol functional groups found in Mefp-5 and was used as a molecular building block for polymer coatings [35].*

Polydopamine coating of membrane surfaces is an extremely simple and economical process compared to many other functionalization ones and the introduction on the membrane surface of abundant hydrophilic groups such as hydroxyl, carboxyl and amino is capable of endowing hydrophobic membranes with hydrophilicity, thus mitigating the fouling phenomenon [34]. Furthermore, many studies have shown that the polydopamine layer on polymer surfaces has good stability and durability in various environments, except in strongly alkaline solutions (pH > 13) [33, 35].

In order to maximize the performance of PDA modification, a comprehensive understanding of the dopamine self-polymerization process is essential. A proposed model for the polymerization reaction is shown in Figure 4.

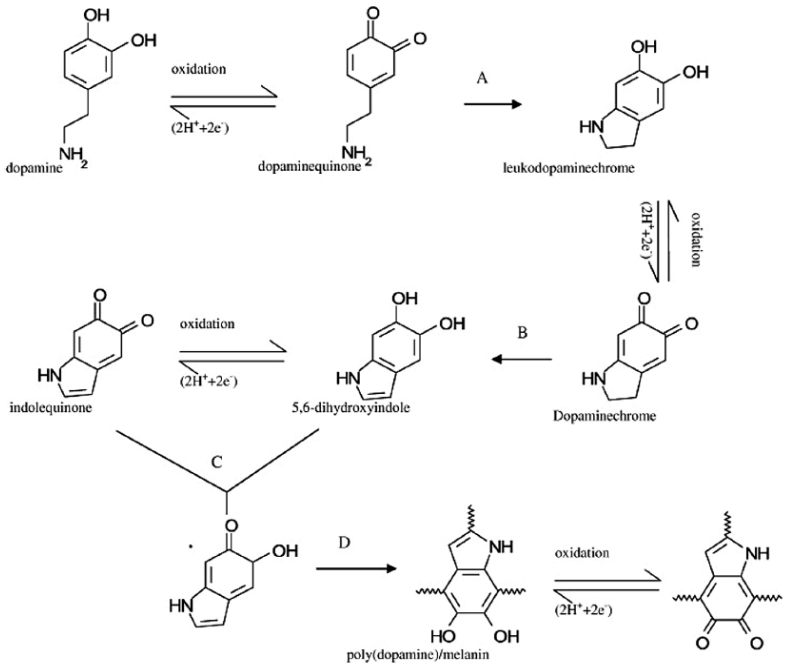

Figure 4. *Hypothesized reaction mechanism of dopamine polymerization [34].*

Dopamine is oxidized to dopaminequinone and then the dopaminequinone rearranges into leucodopaminechrome by intramolecular cyclization. Leucodopaminechrome is then oxidized to dopaminechrome and generates 5,6-dihydroxyindole after rearrangements. 5,6-dihydroxyindole could be oxidized to indolequinone [34]. The reverse dismutation reaction between catechol and 5,6-dihydroxyindole leads to cross-links and to the formation of polydopamine (PDA).

The deposition of PDA increases the hydrophilicity and thus the antifouling performance of the membrane, leading to higher permeate flux. However, the presence of the PDA layer inevitably causes a decrease in the pore size and, under certain conditions, could even lead to pore blocking. As a result, the permeability of the membrane might decrease and the selectivity increase instead. Under these circumstances, hydrophilicity does not predominate on the permeability of the membranes, resulting in flux decline [34]. Consequently, the characterization of the fouling phenomenon via the monitoring of flux decline for dopamine-

functionalized membranes might be interfered with the pore shrinkage caused by the deposition of polydopamine itself.

Therefore, it is required to control the operating conditions of dopamine deposition to obtain an optimal coating thickness that leads to a modest pore size reduction, as well as to a hydrophilicity enhancement. Wang et al. studied the effect of the initial dopamine solution concentration and the PDA deposition time on the thickness of the PDA layer and the average size of the pores [37]. Based on the modeling results, the membrane mean pore radius decreased with increasing initial dopamine concentration or increasing PDA coating time. Commonly chosen dopamine concentration in the initial solution for the functionalization of polymeric membranes is $2\ g\ L^{-1}$, while one to five hours are suggested for the deposition time.

Other parameters that must be controlled to optimize dopamine deposition rates are the solvent pH and the type of oxidants. As regards the pH, a weakly alkaline environment (pH = 8.5) was demonstrated to be the most favorable for dopamine self-polymerization. Phosphate or Tris buffer solution is normally used in simulating natural marine environments' pH in experiments [34], since dopamine self-polymerization is derived from the imitation of the adhesion behavior of marine mussels. In addition, a mild oxidizing agent can increase the rate of dopamine polymerization without damaging the structure of a polymeric membrane. To simplify the modification process without additional contamination, the oxidant should be inexpensive, readily available and environmentally friendly. In this case, oxygen generated by aeration might be a viable choice for lab scale processes [34].

4.1.2. Grafting on the Polydopamine Layer

Catechol groups, primary amines and secondary amines in the polydopamine layer can react with thiols and amines in organic molecules via Michael addition

or Schiff base reactions, thereby creating an inert platform for secondary reactions [38]. Therefore, the polydopamine layer also serves as an interface layer for post-modification and allows the membrane to be further modified by other functional materials [34]. A variety of grafting methods were developed to improve the performance of the modified dopamine-based membrane in terms of hydrophilicity, alleviation of fouling, selectivity towards specific foulants, mechanical properties and stability in various environments.

Furthermore, the presence of o-benzoquinone in the PDA layer adhered on the membrane surface allows for covalent immobilization via Michael addition of bovine serum albumin (BSA), since it owns a terminal amino group [36, 39, 40]. Some medical applications, such as hemoperfusion for hyperbilirubinemia relieving, have taken advantage of the BSA immobilization on the polydopamine layer. Since BSA can bind with many different molecules such as bilirubin, drugs, toxic compounds, and biological molecules, immobilizing BSA on the PDA layer of a membrane allows to remove these harmful substances from the bloodstream [41]. However, in industrial applications such as water and wastewater treatment, energy production and food processing, the immobilization of proteins like BSA on the membrane surface is a detrimental event, as it leads to membrane fouling. From this point of view, the grafting of amino terminal chemicals on the polydopamine layer could lead to partial saturation of the binding sites for the amine group and therefore prevent or mitigate the immobilization of BSA.

Methoxy Polyethylene Glycol Amine ($mPEG - NH_2$)

One of the most extensively studied anti-fouling polymers is methoxy polyethylene glycol amine ($mPEG - NH_2$) (Figure 5), which can be grafted on the polydopamine layer by the coupling between o-benzoquinone of PDA and the $mPEG - NH_2$ amine.

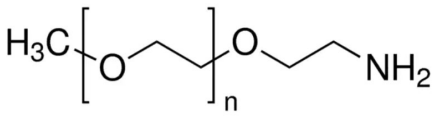

Figure 5. *Methoxy polyethylene glycol amine molecular structure.*

$mPEG-NH_2$ is widely adopted by academic and industrial researchers, since it is a water-soluble polymer with low toxicity and an extensive history of use in medicine and drug delivery [42]. Although the thermodynamic and molecular mechanisms for the protein and cell resistance of surface immobilized $mPEG-NH_2$ are not completely understood, numerous studies have determined that steric hindrance effects, chain length, grafting density, chain conformation and hydrophilicity of the grafted polymer play important roles in resisting protein, cell and bacteria adhesion. Membranes modified by $mPEG-NH_2$ show a 95% reduction in protein adsorption and have a reliable mechanical stability through intensive hydraulic backflushing [32]. Furthermore, with the coverage of a grafted $mPEG-NH_2$ layer, the modified membrane showed better chemical stability to the acid and alkaline solution than the single polydopamine layer one [32].

For all these reasons, $mPEG-NH_2$ coatings are widely used to control fouling of implantable medical device surfaces, contact lenses, surgical tools, biosensors, electrophoresis capillaries for bio-separations and fouling-prone surfaces of water treatment facilities and ship hulls [42].

Tannic Acid (TA)

The polyphenol-based surface engineering, in particular the one based on tannic acid (TA), has received increasing attention for surface manipulation, hydrophilization, and antifouling applications [43].

Tannic acid (TA) is a polyphenol produced by the condensation of a molecule of glucose and five molecules of digallic acid, in turn formed by the esterification of two molecules of gallic acid. Its potential as a membrane coating was first illustrated through simple experiments involving untreated green tea and red wine

[44]. These researches led to the surprising finding that thin polyphenolic coatings spontaneously formed on surfaces exposed to such drinks [44]. Furthermore, it has been found that the TA coating, emulating the natural role of plant polyphenols in biological defense, exhibits strong antibacterial properties and no observable cytotoxicity [44]. Starting from polyphenol-based surface engineering, some researchers hypothesized the grafting mechanism of tannic acid on the polydopamine layer, shown in Figure 6, where the phenol moieties from TA molecules could be partially oxidized into quinone moieties and then covalently bonded with amino groups of polydopamine via Michael addition/Schiff base reactions, under aerobic alkaline conditions [43].

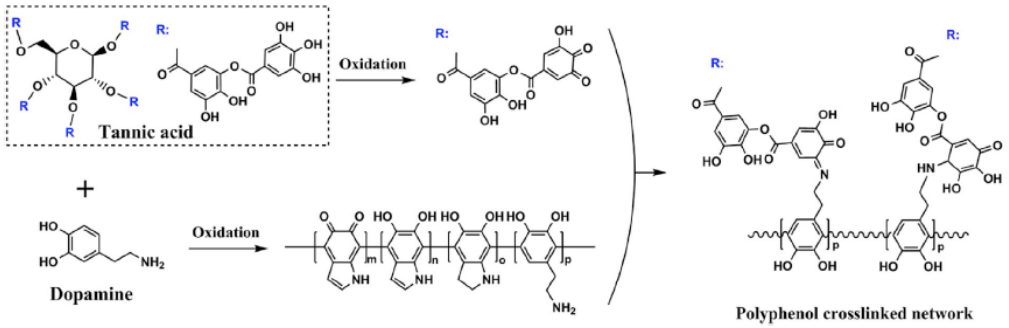

Figure 6. *The possible mechanism illustration for construction of TA grafting on the polydopamine layer [43].*

A different functionalization method based on dopamine and tannic acid consists of carrying out a co-deposition of tannic acid and dopamine, in order to incorporate the tannic acid in the polydopamine layer. Co-deposition methods lead to a more uniform coating layer on the membrane surface and a better adhesion of the polymer on the substrate has been observed [43].

N,N-dimethyl ethylenediamine (DMEDA) for zwitterionic functionalization

N,N-dimethyl ethylenediamine (DMEDA) is a molecule dense of amino groups (Figure 7), therefore able of covalently binding to the o-benzoquinone of polydopamine via Michael's addition.

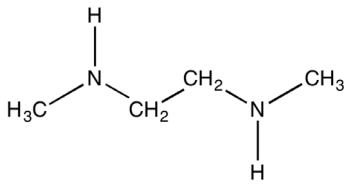

Figure 7. *N,N-dimethyl ethylenediamine (DMEDA) molecular structure.*

Although grafting with DMEDA already shows a good increase in the antifouling properties of the membrane, it is generally used as a precursor of a further functionalization with zwitterionic materials. In fact, zwitterionic materials have recently attracted great interest in the fabrication of antifouling membrane surfaces due to their ultralow fouling properties [45]. Zwitterionic based materials, such as 1,3-propane sultone, can bind water molecules via electrostatically induced hydration, which is stronger compared to the hydrogen bonding induced hydration in PEG based polymers. Consequently, zwitterionic materials have been shown to be highly resistant to nonspecific protein adsorption, bacteria adhesion, and biofilm formation [45].

Plasma-treatment with Oxygen Plasma and APTES

Before carrying out a coating on the membrane surface, the membranes are often pre-treated in order to be integrated within polymer-based microfluidic systems. One of the most common pre-treatments before the polydopamine layer involves the oxygen plasma treatment and a subsequent coating with an aqueous solution of (3-aminopropyl) triethoxylane (APTES). APTES is frequently used in silanization processes, i.e., in the functionalization of surfaces with alkoxysilane molecules. APTES is also used in numerous applications as a binding agent, as a promoter of the adhesion process and as a pretreatment of the coating [46].

4.1.3. Grafting of Zwitterions

Zwitterions (also known as inner salts) are small molecules that contain an equal number of positively- and negatively-charged functional groups, being therefore

neutral on the whole. Many biological molecules such as phospholipids and aminoacids are examples of these molecules and their related polymers (polyzwitterions).

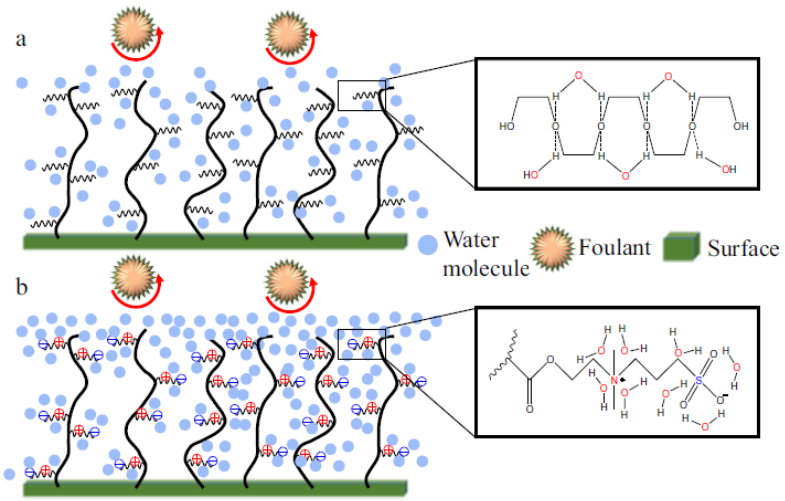

Figure 8. *Formation of the hydration shell for* ***(a)*** *a hydrophilic surface (e.g. functionalized with polyethylene oxide brushes and* ***(b)*** *a polyzwitterion functionalized one [47].*

Owing to their ability to form an electrostatic based hydration layer, zwitterionic polymers have widely been accepted as the next-generation of antifouling materials [48]. In water environments, the antifouling action of such macromolecules is based on two major mechanisms. The former concerns the formation of a hydration shell where water molecules combine with the charged moieties of the zwitterionic tethers through ionic solvation – or rather via electrostatic forces –, forming therefore a barrier preventing the membrane from contacting foulants [49]. The strength of the electrostatic bonds in the hydration layer is much higher than that associated with the hydrogen bonds characterizing hydrophilic surfaces, for this reason a denser and thicker hydration shell forms on zwitterionc functionalized materials, enhancing their antifouling potential. From a thermodynamic standpoint, this translates in a higher maximum of Gibbs free energy, which means that a large amount of energy is needed by foulants to be adsorbed on the membrane surface. The second mechanism is related to steric

hindrance. When solutes come in contact with polyzwitterions, their excluded volume is compressed and mobility reduced, with an associated increase in the Gibbs free energy. In order to recover a lower energy state, chains swell back to their initial state, hindering foulants from getting closer to the membrane surface [47, 48]. Figure 8 summarizes the main differences between hydrophilic and zwitterionic functionalized surfaces in terms of antifouling potential.

The degree of hydration, and thus the antifouling potential, depends on several factors, such as the molecular weight of the polyzwitterion, its chemistry, the density and conformation of the chains and the presence of ions in solution (REF). Indeed, although hydrophilic, polyzwitterions may be insoluble in pure water due to dipole-dipole interactions between the charged groups, which cause the chains to take a collapsed-coil form [50] (Figure 9). The addition of salts counterbalances the electrostatic interchain attraction, allowing each polyzwitterion to be properly solvated and expand in the surrounding aqueous media. Such behavior is known as antipolyelectrolyte effect and represents a key factor for the proper use of zwitterions as a fouling mitigation strategy [51].

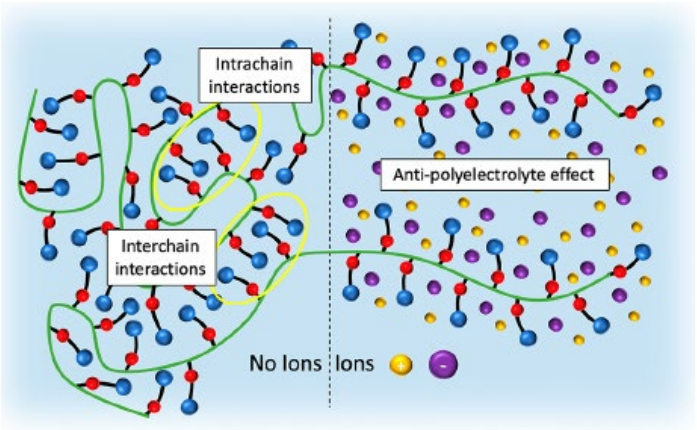

***Figure 9**. Schematic representation of the antipolyelectrolyte effect of the conformation of polyzwitterion chains. On the left, electrostatic interchain interactions force the polymer to take a coiled shape; extended chains can be observed in presence of ions disrupting such attractive forces [49].*

Polyzwitterions are classified into two main groups, polybetaines and polyampholites [52]. Polybetaines are characterized by the presence of both a negative and a positive charge on the same monomer unit of a polyzwitterion and are further divided into sulfobetaines, carboxybetaines and phosphobetaines. Such class of polyzwitterions has the main advantage of presenting two opposite charges on the same monomer, ensuring the total neutrality of the whole molecule. The formation of polyampholites stems from the reaction of two or more monomers carrying opposite charges. Charge distribution uniformity and neutrality are therefore achieved by controlling the monomers' ratio before their polymerization. Compared to polybetaines, the growth of such polyzwitterions presents a higher degree of complexity and the presence of defects, such as multiple adjacent monomers carrying the same charge, may compromise the antifouling action. Figure 10 schematizes the conformational differences between the two classes of polyzwitterions.

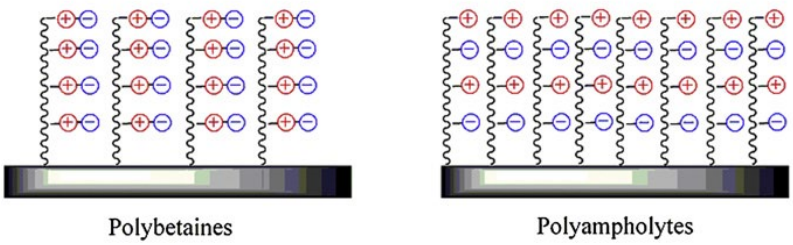

Figure 10. *Illustration of the charge distribution on polybetaines and polyampholites. Adapted from [52].*

Grafting is the most used strategy to incorporate polyzwitterions onto the surface of a membrane via stable and long-lasting chemical bonds. Two approaches can be distinguished, namely "grafting to" and "grafting from" [53]. In the former an already synthesized and previously end-functionalized polyzwitterion is reacted onto the membrane surface; instead, in the "grafting from" process monomers are polymerized directly from the membrane surface. "Grafting from" was reported to be the most common approach due to the easier control of chain density and the better antifouling performance [47].

A versatile method to grow polyzwitterions from the surface of a membrane is surface initiated atom transfer radical polymerization (SI-ATRP). Such polymerization reaction represents one of the most robust controlled radical polymerization techniques and can be used for a wide range of commercially available monomers [54]. Conversely to conventional radical polymerization, characterized by slow initiation, fast propagation and radical termination, SI-ARTP exploits a dynamic equilibrium between the active radicals and the dormant species, which intermittently react with both activators and deactivators in the reaction system. Together with the monomers of interest, SI-ATRP generally involves the presence of ligand-stabilized transition metal complexes acting as activators and of an alkyl halide as an initiator. SI-ATRP reaction mechanism is schematized in Figure 11.

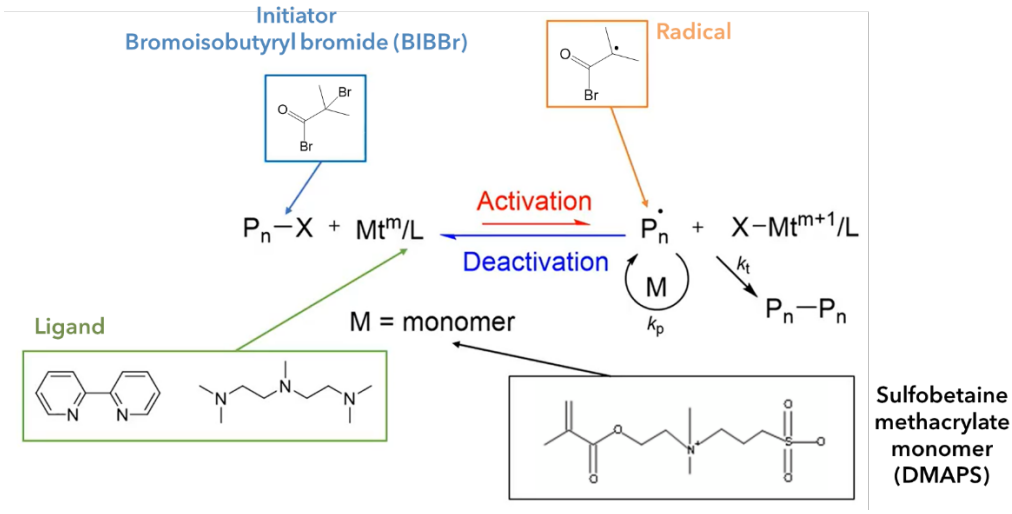

***Figure 11**. SI-ATRP reaction mechanism for the synthesis of polyDMAPS. Bromoisobutyryl bromide (BIBBr) is used as initiator, CuBr and $CuBr_2$ as catalysts and N,N,N', N'', N''-Pentamethyldiethylenetriamine (PMDETA) as ligand.*

SI-ATRP was successfully exploited by Guo et al. for the development of a nanofiltration membrane with tunable antifouling properties [55]. Yue et al. employed SI-ATRP to graft poly(sulphobetaine methacrylate) from polysulfone membranes to improve both membrane biocompatibility and fouling resistance

[56]. Other interesting applications can be found in the works of Sui et al. and Luo et al. [57, 58].

4.2. Membrane Nano-structure Modification

4.2.1. Self-assembled Block Polymers

Despite the high potential of application, membrane coating and subsequent grafting approaches may suffer from non-uniform and incomplete coverage [59]. For this reason, new functionalization approaches have been explored that exploit the chemical nature of the membrane itself, eliminating therefore the need for a coating. These techniques involve surface initiated polymerization reactions, such as reversible addition fragmentation chain transfer polymerization and atom-transfer radical polymerization.

The application of such approaches, however, is limited by the lack of sufficient functional groups for surface polymerization [60]. Modifying the membrane nano-structure to introduce new functional moieties represents, therefore, an interesting research field towards the development of new fouling mitigation strategies. A promising material platform for membrane fabrication, characterized by nearly-limitless chemical composition, is represented by self-assembled block polymers [61].

The main feature that makes self-assembled block polymers so useful as materials for membrane films lays in their equilibrium nano-structure, formed upon the separation of the material microphase. Microphase separation takes place due chemical incompatibility between the covalently-connected constituent moieties of the precursor block polymer. Since the final characteristics of a membrane are intimately related to the nano-structure, the design of the macromolecular architecture of the precursor block polymers is a factor of crucial importance [62]. An essential feature for the selection of the precursor polymers is that the material microphase separates forming ordered structures, which will define the membrane

pores. In order to obtain a specific equilibrium nano-structure, it is thus important to consider all the factors affecting its final order, namely the interactions between polymer blocks of different natures, the overall degree of polymerization and the volume fraction of the functional moieties.

The possibility of tailoring pore wall chemistry in combination with the narrow pore size distribution make self-assembled block polymer membranes suitable for applications where a high selectivity is required for the separation of specific solutes. In such a way, these membranes become similar to reactors characterized by a high density of active sites and low and constant residence time [61, 63]. Functional self-assembled membranes can be obtained in three different ways, summarized in Figure 12. Indeed, functional molecules can be directly incorporated into the membrane precursor, grafted on the pore walls or directly obtained from the pore walls by introducing specific precursors that allow for post-assembly functional modifications.

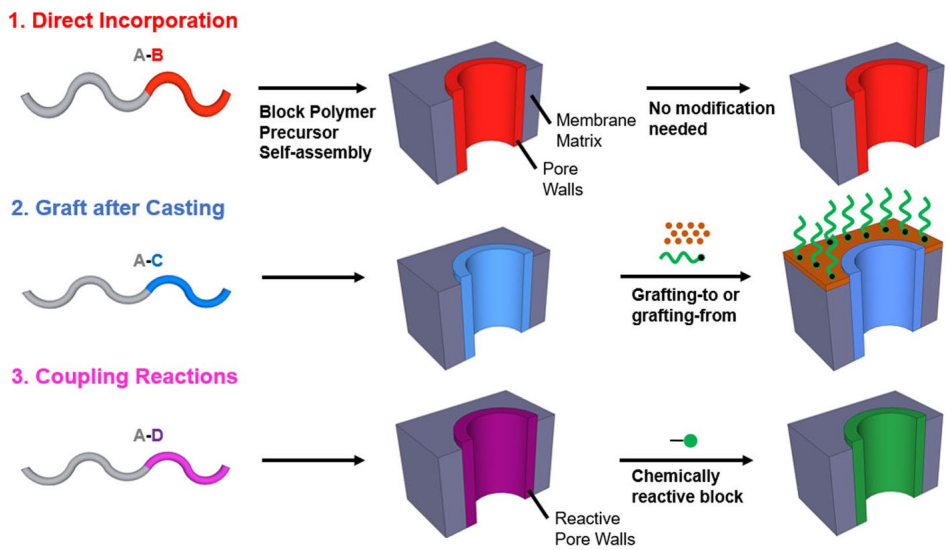

Figure 12. *Functional moieties introduction strategies for self-assembled block polymer membranes [61].*

Dual-functional self-assembled block polymer nanofiltration membranes were developed by Hoffman and Phillip. By means of click reactions (i.e. copper (I)-

catalyzed azide-alkyne cycloaddition, CuAAC) it was possible to create layered domains of distinct functionality along the pore walls, endowing the membrane with both antifouling and ion rejection characteristics [64].

To fabricate actual membranes with useful permeability, however, the self-assembled nano-structure of block polymers has to be supported by an additional layer, usually microporous. A common technique for membrane fabrication is that of self-assembly and nonsolvent induced phase separation.

4.2.2. Nonsolvent Induced Phase Separation

Nonsolvent induced phase separation (NIPS) is a common fabrication method for asymmetric membranes. Such process begins with casting a thin film of a block polymer solution on a substrate (e.g., PVDF) followed by a controlled evaporation of the solvent, which leads to an increase in polymer concentration, causing the formation of ordered nano-structures. Right after the evaporation of the solvent, the film is immersed into a nonsolvent bath, where a rapid exchange between the solvent and the nonsolvent takes place, trapping the self-assembled nano-structure of the polymer layer.

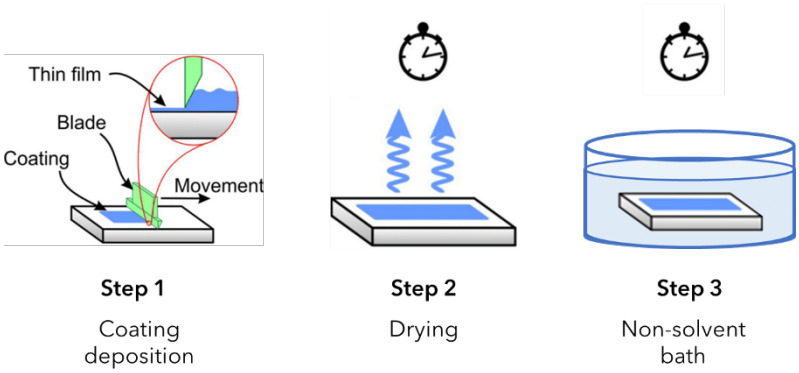

Figure 13. *Nonsolvent induced phase separation steps for asymmetric membranes production from self-assembled block polymers.*

As the solvent evaporates, the surface nanostructure undergoes a state transition from a disordered morphology into various ordered states as a function of polymer concentration [65].

The formation of the porous nano-structure and of an asymmetric cross-section are what guide the selection of the solvent. Indeed, an intimate relationship exists between these structural features and the solvent-polymer interactions, the volatility of the solvent and the rate of exchange between the solvent and the nonsolvent. Selecting the proper nonsolvent is crucial as well, due to the impact on the final morphology of the polymer film [66]. In fact, if the rate of exchange is too high, there won't be enough time for the nano-structure to form properly, leading to the generation of smaller ordered domains or a dense structure, which may result in a damaged final product. In many cases, two subsequent nonsolvent baths may be employed, with the first one characterized by a milder rate of exchange. In such cases, the evaporation time between the two baths, represent a key factor as well for the development of the desired pore distribution [64].

4.3. Membrane Surface Patterning

In surface patterning, fouling is mitigated thanks to the alteration of the membrane surface topography. Indeed, the presence of specific patterns on the membrane surface leads to the generation of eddies which, combined with crossflow velocity, facilitate back-diffusion of foulants to the feed bulk [67]. Moreover, particle deposition can be hindered using pattern designs characterized by the presence of valleys smaller than the particle size [68]. Surface patterning also serves as a turbulence promoter, enhancing the local mixing near the membrane surface and reducing the velocity required for turbulence generation.

Two main surface patterning methods can be distinguished, template-based micromolding and direct printing [69]. The former is carried out using a patterned master mold, which is typically fabricated via lithographic processes, and is divided into solution-based and embossing micromolding.

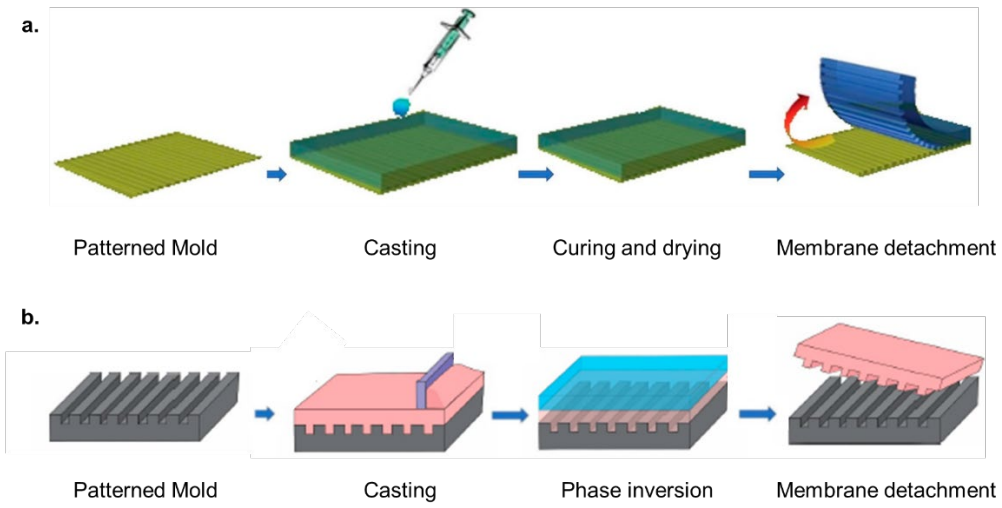

Figure 14. *(**a**) Solution casting micromolding procedure; (**b**) Phase separation micromolding procedure [69].*

Solution-based micromolding techniques make use of phase inversion processes to form a solid membrane from a liquid dope solution, as showed in Figure 14. Such solution can be casted onto a master mold, on which the membrane will solidify following a specific pattern as the solvent evaporates. The formation of the membrane solid matrix upon solidification of the polymer solution can also be achieved by casting the film into a nonsolvent bath, employing, therefore, the so-called nonsolvent induced phase separation (NIPS). On the other side, embossing involved the use of a rigid master mold at high pressure and temperature to stamp the pattern on a polymeric surface.

Direct printing can be realized by ink-jet printing or 3D printing, instead [70, 71]. In the former, computer-designed patterns are created as a consequence of the evaporation of the solvent in structured droplets of a polymer solution. 3D printing is also known as microstereolithography and allows the formation of complex three-dimensional patterns via layer-by-layer deposition of polymeric material. Applications of membrane surface patterning can be found in reverse osmosis processes, membrane bioreactors and membrane distillation operations as well [72-74].

5. Enhancing Membrane Hydrophilicity via Surface Functionalization for Antifouling Purposes

Coating and grafting functional materials on the membrane surface and pore walls can lead to the modification of membrane chemistry and foulant-membrane interactions, aiming to reduce adsorption/adhesion of specific foulants. Research has particularly focused on hydrophilic membrane modifications, which not only increase the membrane flux due to affinity towards water molecules, but also mitigate membrane fouling. The latter occurs through reducing membrane-foulant hydrophobic interactions by attracting a strongly-bound water layer to the membrane surface that acts as a buffer against foulant adhesion [32]. In this area of interest, mussel-bio-inspired dopamine coatings have become a promising solution for membrane surface modification, due to their universality and biocompatibility, therefore representing excellent candidates for bio-applications, such as water purification and hemodiafiltration. Simply immersing membranes into an alkaline dopamine solution can trigger the polymerization of a hydrophilic polydopamine layer on the membrane surface, which enhances both mechanical properties and hydrophilicity [32]. Moreover, the polydopamine layer contains various functional groups, which allows the membrane to be additionally grafted with other functional materials – such as nanoparticles, oligomers, or polymers – which could further improve hydrophilicity and selectivity by hindering the accumulation of specific deposits.

In the following section the effects of dopamine-based coatings on hydrophilicity for antifouling purposes were studied. Two different commercial membranes were investigated, specifically a polyvinylidene fluoride (PVDF) membrane, characterized by marked hydrophobicity, and a polyethersulfone (PES) hydrophilic one. Before use, PVDF membranes are generally soaked in alcohols, such as methanol or ethanol, for a short time to allow for hydration; in this study,

however, such preparation step was not performed purposely, in order to have the most hydrophobic surface possible. Various functional materials were grafted onto the polydopamine layer, namely methoxy polyethylene glycol amine ($mPEG-NH_2$), Tannic Acid (TA) and N,N-dimethyl ethylenediamine (DMEDA), in order to improve hydrophilicity and thus the antifouling potential of the membrane surface. In addition, the effect of surface chemical modifications on the dynamics of protein fouling in microfiltration processes was studied in depth through microfluidics, using bovine serum albumin (BSA) as a model protein foulant.

5.1. Experimental

5.1.1. Materials and Operations

Two different membranes characterized by the same nominal pore size of $0.2\ \mu m$ were used in this study. The former was a hydrophobic polyvinylidene fluoride (PVDF) membranes provided by BIORAD, whereas the latter a hydrophilic polyether sulfone (PES) membranes obtained from Sterlitech, USA. Membrane coating was performed using dopamine hydrochloride (99%) (Sigma Aldrich, USA). Tannic Acid (TA) (Sigma Aldrich, USA), methoxy polyethylene glycol amine ($mPEG-NH_2$) (MW 5000 Da) (Sigma Aldrich, USA), (3-Aminopropyl) triethoxylane (APTES) (99%) (Sigma Aldrich, USA) and (Sigma Aldrich, USA) and N,N-dimethyl ethylenediamine (DMEDA) (Sigma Aldrich, USA) were used for further grafting on coated membranes. Commercial soybean oil was used for under-water oil contact angle measurements. Bovine serum albumin (BSA) (MICROGEM, Italy) was used as a model foulant at a concentration of $10\ mg\ mL^{-1}$. Oxygen plasma pre-treatment was carried out in a plasma oven (Diener Electronic PCCE).

Filtration experiments were carried out using the same setup described in *Chapter 1 – Fouling Phenomena*, section 5: Experimental Study on the Effect of Pumping

Systems on Fouling Evolution. Constant pressure crossflow filtration tests were carried out using a peristaltic pump (Masterflex L/S with an Easy-Load II pumping head, Antylia Scientific, USA) at a feed rate of $2\ \mathrm{mL\ min^{-1}}$ and a $\overline{\mathrm{TMP}} = 20\ \mathrm{mbar}$, kept equal in dead-end tests, performed using pressure driven flow controller (PDFC) (MFCSTM-FLEX, Fluigent, USA).

Contact angle measurements were performed both in air using water and underwater using oil. In the first case, membrane sheets were placed on a horizontal support and a 10 µL droplet of distilled water was dropped onto the membrane surface, using a volume pipette. In the second case, a membrane sheet, previously dried overnight on filter paper, was taped to a support and immersed in a water bath, facing the side of interest downwards. At this point, a syringe released an oil droplet of 5 μl into the water bath. Since oil has a lower density than water, the oil droplet raised upwards, until it touched the membrane surface.

5.1.2. Membrane Functionalization Methods

The first step in the membrane chemical modification process was to build a layer of polydopamine on the membrane surface. The polydopamine coating was carried out simply by immersing small membrane sheets ($3\ \mathrm{x}\ 1.5\ \mathrm{cm^2}$) in an aqueous dopamine solution, which was prepared via Dopamine Hydrochloride ($2\ \mathrm{mg\ mL^{-1}}$) dissolving in TRIS – HCl buffer solution (10 mM, pH 8.7). Before being functionalized, the membrane sheets were observed under an optical microscope to verify surface homogeneity and the absence of imperfections such as holes or lesions. Afterwards, they were subjected to a cleaning procedure that allows the elimination of any impurities. This procedure involves immersion for 10 minutes in a Petri dish containing isopropanol and then rinsing for 20 minutes in distilled water, changing the washing water twice. During the washing procedure, the Petri dishes were placed on a tilting shaker, in order to further promote impurity removal. Subsequently, the cleaned membrane sheets were immersed in a Petri dish containing the previously prepared dopamine solution,

considering that approximately 25 mL of solution are needed for each membrane. Petri dishes were placed on the tilting shaker and left uncovered, so that stirring and aeration speed up the polymerization rate. A reaction time of 1 hour was chosen, as recommended by literature studies, in order to avoid excessive dopamine deposition that might clog the membrane pores [37]. Once the indicated time had elapsed, the functionalized membranes were cleaned, in order to remove residues of uncured dopamine. The cleaning procedure involves washing in ethanol for 10 minutes, followed by rinsing in distilled water for 30 minutes, and changing the washing water three times.

In the second phase, a functional material was grafted onto the polydopamine layer. For this purpose, the membrane sheets – previously functionalized with polydopamine – were alternately immersed in one of the two following aqueous solutions:

- 1mM methoxy polyethylene glycol amine (mPE $-NH_2$) in TRIS-HCl buffer (10mM, pH 8.7);
- 2 mg mL^{-1} Tannic Acid (TA) in 100 mM Bicine buffer, 0.6 M NaCl, pH 7.8.

Moreover, to evaluate the possibility of further increasing their hydrophilicity, the PES hydrophilic membranes were subjected to the following functionalization, summarized in Table 1:

- Polydopamine coating followed by the grafting in an aqueous solution of 2 mg mL^{-1} N,N-dimethyl ethylenediamine (DMEDA) dissolved in TRIS - HCl buffer (10 mM, pH 8.7);
- One-step co-deposition by immersing the membrane sheets in an aqueous solution of Dopamine Hydrochloride (2 mg mL^{-1}) Tannic Acid (2 mg mL^{-1}) dissolved in TRIS-HCl buffer (10 mM, pH 8.7);

- Pre-treatment with oxygen plasma and submersion in an aqueous solution of APTES 5% volume, followed by the grafting in Dopamine Hydrochloride ($2\ \mathrm{mg\ mL^{-1}}$) in TRIS -HCl buffer solution ($10\ \mathrm{mM}$, pH 8.7).

In the first three cases, the grafting solution was stirred for a few minutes at room temperature and then poured into the Petri dishes. The polydopamine-coated membrane sheets were submerged in the graft solution and then stirred on the tilting laboratory shaker overnight (i.e., for about 24h), closing the Petri dishes with a lid, to avoid excessive evaporation of the solution. Subsequently, the membranes were rinsed in distillate water for about 30 minutes, changing the washing water three times.

In the one-step co-deposition case, before being functionalized, PES membrane sheets were observed under an optical microscope to verify the absence of imperfections such as holes or lesions. Then, they were subjected to a cleaning procedure which involves immersion for 10 minutes in a Petri dish containing isopropanol and then rinsing for 20 minutes in distilled water, changing the washing water twice. During the washing procedure, the Petri dishes were placed on a tilting laboratory shaker, in order to further promote the impurity removal. Subsequently, equal volumes of the two coating solutions were poured together in a Petri dish. The cleaned PES membrane sheets were submerged in the coating solution and Petri dishes were placed on the tilting shaker and left uncovered, so that stirring and aeration speed up the polymerization rate. A reaction time of 1 hour was chosen, so that the polydopamine layer had a thickness comparable to that obtained in the previous functionalization. As the indicated time had elapsed, the functionalized membranes were cleaned, in order to remove residues of uncured dopamine and tannic acid. The cleaning procedure involves washing in ethanol for 10 minutes, followed by rinsing in distilled water for 30 minutes, changing the washing water three times.

PES membranes sheet were pre-treated via oxygen plasma for 1 minute on each side according to the following steps: air pumping down for 1 minute, oxygen supply for 1 minute, plasma excitation for 1 minute, final flushing for 10 seconds. Subsequently, an aqueous solution of APTES 5% volume was prepared and poured into a glass Petri dish, closed with a lid to avoid evaporation and placed in an oven at 80°C. After the solution reached the set temperature, the PES membrane sheets, previously treated with oxygen plasma, were immersed in the APTES solution and left in the oven at 80°C for 20 minutes, under mild stirring. Membranes were dried with filter paper before further functionalization. Membrane washing was carried out in ethanol for 10 minutes, followed by distilled water for 30 minutes, changing the washing water three times.

Table 1. *Summary of the membrane chemical functionalization performed in the present work.*

	Membrane	**Coating**	**Grafting**
PVDF (as received)	PVDF	-	-
PVDF-PDA	PVDF	Dopamine (2 mg mL^{-1}) in TRIS-Buffer HCl (10 mM, pH 8.7)	-
PVDF-PDA-PEG	PVDF	Dopamine (2 mg mL^{-1}) in TRIS-Buffer HCl (10 mM, pH 8.7)	mPE $-NH_2$ in Tris-HCl buffer (10 mM, pH 8.7)
PVDF-PDA-TA	PVDF	Dopamine (2 mg mL^{-1}) in TRIS-Buffer HCl (10 mM, pH 8.7)	Tannic acid
PES (as received)	PES	-	-

PES-PDA	PES	Dopamine (2 mg mL^{-1}) in TRIS-Buffer HCl (10 mM, pH 8.7)	-
PES-PDA-PEG	PES	Dopamine (2 mg mL^{-1}) in TRIS-Buffer HCl (10mM, pH 8.7)	mPE $-NH_2$ in TRIS -HCl buffer (10 mM, pH 8.7)
PES-PDA-TA	PES	Dopamine (2 mg mL^{-1}) in TRIS-Buffer HCl (10 mM , pH 8.7)	Tannic Acid (2 mg mL^{-1}) in Bicine buffer (100mM), NaCl (0.6M) pH 7.8
PES-PDA-DMEDA	PES	Dopamine (2 mg mL^{-1}) in TRIS-Buffer HCl (10mM, pH 8.7)	DMEDA (2 mg mL^{-1}) in TRIS -HCl buffer (10mM, pH 8.7).
PES-APTES-DA	PES	APTES 5% volume in water	Dopamine (2 mg mL^{-1}) in TRIS-Buffer HCl (10 mM, pH 8.7)
PES-PDA-TA (co)	PES	Codeposition of Dopamine (2 mg mL^{-1}) and Tannic Acid (2 mg mL^{-1}) pH 8.7	-

5.1.3. Chemical Analysis

BSA concentration in retentate and permeate streams was determined by spectrophotometry (UV-1700, Shimadzu, Japan). For each experiment, a calibration curve of protein concentration as a function of absorbance was computed and for all the calibration curves, the R^2 coefficient was higher than

0.99 in the application range. Attenuated total reflectance spectroscopy (ATR) (Nicolet 5700, Thermo-Fisher) was employed to analyze changes in the functional groups on the membrane surface after modification.

5.2. Results and Discussion

5.2.1. ATR Spectra Analysis

Attenuated total reflectance spectroscopy (ATR) was employed to analyze changes in the functional groups on the membrane surface after modification. By comparing ATR spectra peaks of pristine and functionalized membranes at certain wavenumbers, it was possible to identify the presence of functional materials on the membrane surface and eventually confirm the functionalization was successful. The following figures show the ATR spectra of pristine and functionalized PVDF membranes (Figure 15), and a detail of two wavenumber ranges (Figure 16).

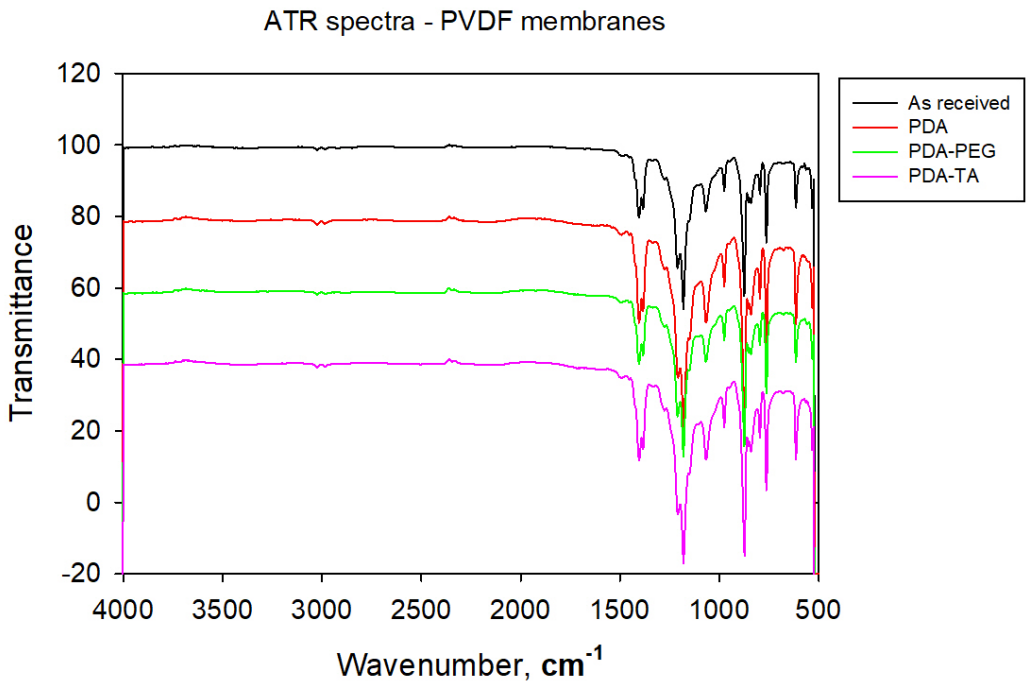

Figure 15. *ATR Spectra of PVDF as received (black) and functionalized PVDF membranes: PVDF-PDA (red), PVDF-PDA-PEG (green), PVDF-PDA-TA (magenta).*

Compared with the ATR spectrum of PVDF pristine membrane, PVDF-PDA membrane spectrum shows two distinct bands at about 1500 and $1645\ \mathrm{cm^{-1}}$ (Figure 16A). These bands were assigned to the overlap of N-H deformation vibration and C=C stretching vibration in polydopamine, respectively, indicating the PDA layer has been successfully fixed onto the PVDF membrane.

The presence of mPEG-NH_2 and Tannic Acid on the membrane surface is generally identified by peaks in the $3100 - 3600\ \mathrm{cm^{-1}}$ band, which corresponds to the hydroxyl groups (O-H) stretching vibrations. However, at these wavenumbers the ATR spectra of PVDF membranes were extremely similar to each other (Figure 16B), possibly due to a combination of factors. First of all, ATR is a bulk technique that allows the spectrometric investigation to a depth of micrometers from the surface [75]. At this depth, the ATR spectrometer may fail to detect the presence of functional materials, since they have been grafted predominantly on the surface of the membranes. Secondly, like tannic acid and PEG, dopamine also has hydroxyl groups, so it also tends to show a peak, albeit slight, in the 3100-3600 $\mathrm{cm^{-1}}$ band [31]. Finally, the presence of atmospheric humidity in the laboratory environment might have slightly moistened the membranes, altering their ATR spectrum in that band. This would explain why the ATR spectra in the band of $3100 - 3600\ \mathrm{cm^{-1}}$ were very similar one to each other.

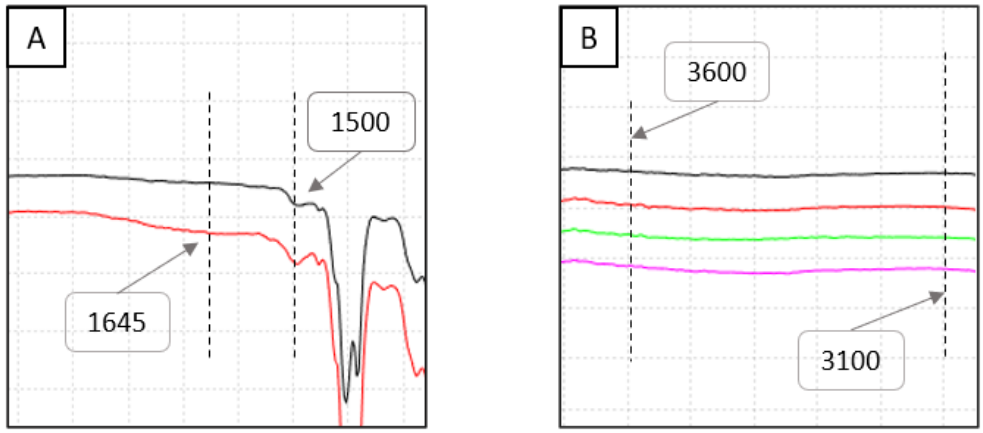

Figure 16. *(**A**) Comparison between peaks at 1500 and 1645* cm^{-1} *of pristine PVDF (black) and PVDF-PDA (red) membranes; (**B**) Comparison between ATR spectra, range (*$3400, 3600$*)* cm^{-1}*, of pristine (black) and functionalized PVDF membranes: PVDF-PDA (red), PVDF-PDA-PEG (green), PVDF-PDA-TA (magenta).*

Figure 17 shows ATR spectra of pristine and functionalized PES membranes, and Figure 18 a detail of the wavenumber bands of interest.

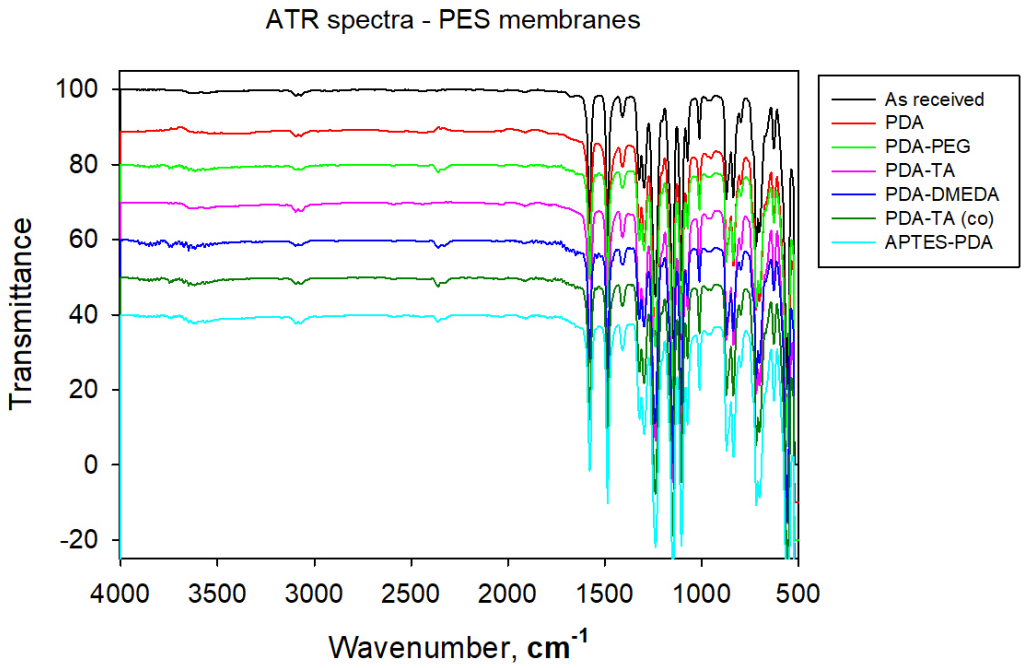

Figure 17*. ATR Spectra of PES as received (black) and functionalized PES membranes: PES-PDA (red), PES-PDA-PEG (green), PES-PDA-TA (magenta), PES-PDA-DMEDA (blue), PES-PDA-TA (co) (dark green), PES-APTES-PDA (cyan).*

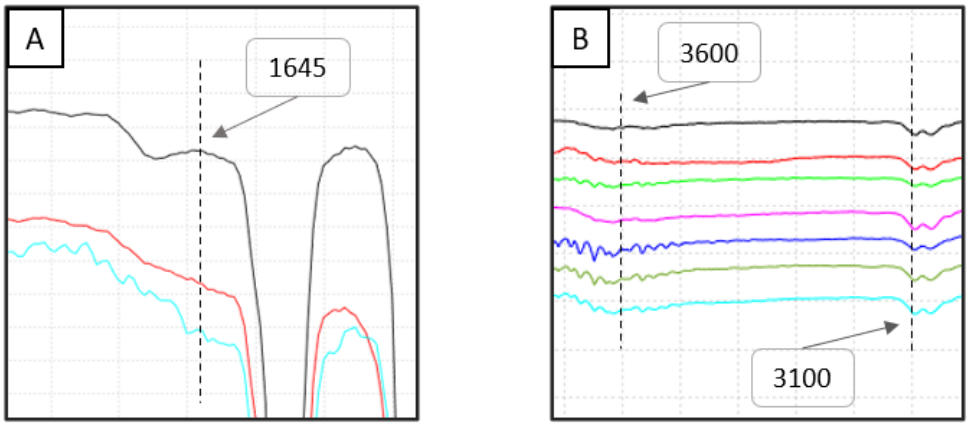

Figure 18. *(**A**) Comparison between peaks at 1645 cm^{-1} of pristine PES (black), PES-PDA (red) and PES-APTES-PDA (cyan) membranes; (**B**) Comparison between ATR spectra, range $(3400, 3600)\ cm^{-1}$, of pristine (black) and functionalized PES membranes: PES-PDA (red), PES-PDA-PEG (green), PES-PDA-TA (magenta), PES-PDA-DMEDA (blue), PES-PDA-TA (co) (dark green), PES-APTES-PDA (cyan).*

To evaluate the success of the dopamine coating procedures, the ATR spectra of the PES-PDA and PES-APTES-PDA membranes were compared with that of the virgin PES membrane (Figure 18A).

Compared with the ATR spectrum of PES pristine membrane, a new band at 1645 cm^{-1} of the PES-PDA and PES-APTES-PDA membranes was assigned to the overlap of C=C stretching vibrations in aromatic ring on dopamine, confirming the PDA coating onto the PES membrane surface. Figure 18B shows the ATR spectra in the band of (3100, 3600) cm^{-1} of all the functionalized PES membranes. Again, ATR spectra in this band were extremely similar, so it was not possible to confirm, by means of such analysis, that the grafting of the functional materials onto the polydopamine layer was successful.

5.2.2. Contact Angles Measurement

Measuring the contact angle (θ) made by a drop of a liquid deposited on the flat horizontal membrane surface is a convenient method to assess the hydrophilicity of the membrane surfaces [31]. While the contact angle of water in air (WCA) indicates the hydration capability of the membrane, the underwater oil contact

angle (UWOCA) stands for the oil repellency (oleophobicity) [76] and therefore indicates the ability to attract a strongly-bound water layer to the membrane surface that acts as a buffer against oil droplets.

The reported contact angle values were calculated by averaging at least three measurements. As shown in and Figure 19, the pristine PVDF membrane was strongly hydrophobic, with an average WCA of $107.75° \pm 2.23°$ and an average UWOCA of $51.80° \pm 1.49°$. After being coated with polydopamine, the WCA decreased to $86.27° \pm 1.29°$, and the UWOCA increased to $138.70° \pm 3.08°$, suggesting that the PDA coating enhanced the hydrophilicity of PVDF membrane surface. After grafting mPE $-NH_2$ and TA on the polydopamine layer, both modified PVDF membranes exhibited a further decrease in WCAs and an increase in UWOCAs. In detail, the increase in hydrophilicity of PVDF-PDA-PEG ($WCA = 66.05° \pm 4.81°$; $UWOCA = 160.73° \pm 3.57°$) appeared to be slightly greater than that of PVDF-PDA-TA ($WCA = 76.53° \pm 3.26°$; $UWOCA = 161.97° \pm 3.56°$).

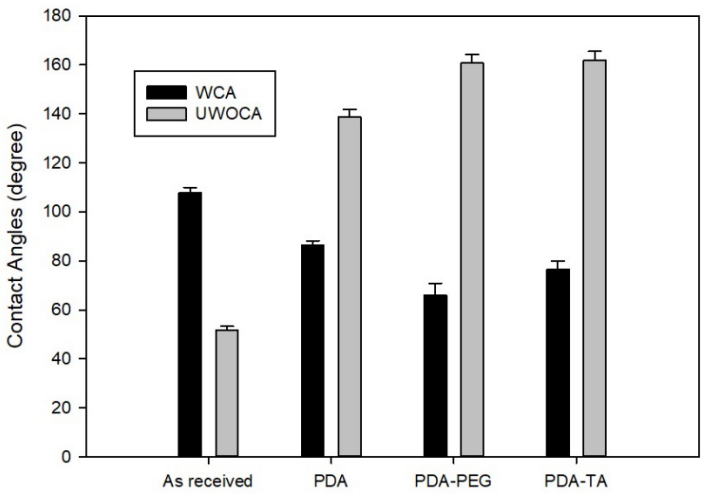

Figure 19. *Water contact angles and underwater oil contact angles of pristine and modified PVDF membranes.*

It is clear that the modified membranes had better hydrophilic properties than the pristine and PDA-coated PVDF membranes, due to the hydroxyl groups on the membrane surfaces originated by the grafting of mPE $-NH_2$ and TA.

Among the objectives of this work, there is the possibility to further increase the hydrophilicity of PES membranes, which as shown in Figure 20, pristine PES membrane was already hydrophilic, with an average WCA of $67.3° \pm 1.13°$ and an average UWOCA of $139.79° \pm 2.64°$. After being coated with dopamine, PES membranes showed a lower WCA ($35.78° \pm 1.45°$) and a higher UWOCA ($154.9° \pm 1.80°$), suggesting that the PDA coating further enhanced the hydrophilicity of PES membrane surface. However, pre-treatment with oxygen plasma and APTES did not lead to a significant increase in hydrophilicity compared to the PES-PDA, since the WCAs are comparable.

After grafting mPE $-NH_2$ and TA on the polydopamine layer, both modified PES membranes exhibited a little improvement in UWOCAs and a further decrease in WCAs. In detail, the increase in hydrophilicity of PES-PDA-PEG ($WCA = 24.61° \pm 0.92°$; $UWOCA = 164.87° \pm 1.29°$) appeared to be slightly greater than that of PVDF-PDA-TA ($WCA = 29.01° \pm 0.33°$; $UWOCA = 160.03° \pm 2.11°$).

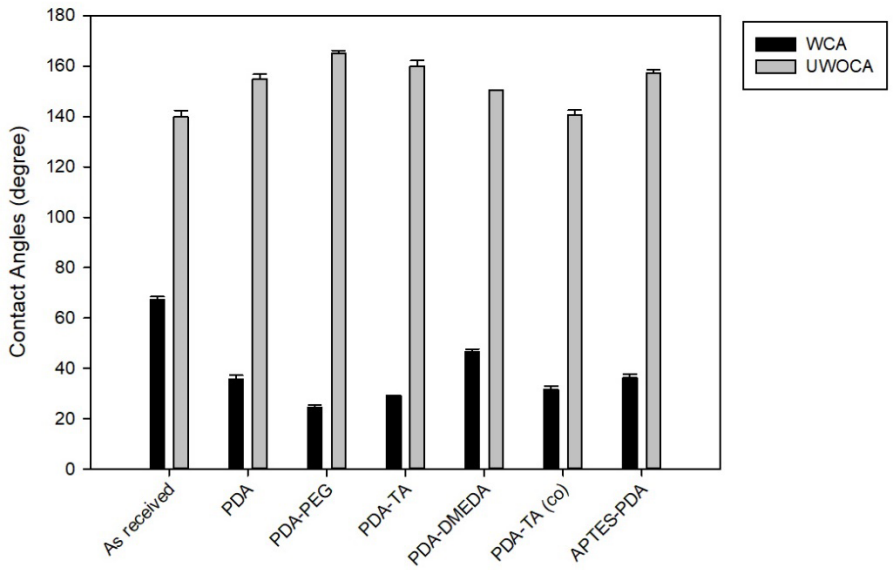

Figure 20. *Water contact angles and underwater oil contact angles of pristine and modified PES membranes.*

However, contrary to expectation, the grafting of DMEDA, and the co-deposition of DA and TA did not lead to an appreciable increase in hydrophilicity. In both cases, these results can be related to a too short dopamine deposition time. Yang et al. found a significant increase in the hydrophilicity of PVDF membranes by carrying out the co-deposition of tannic acid and dopamine for 6 hours [43]. Nayak, Tripathi et al., functionalized microporous polysulfone membranes with a first dopamine layer, obtained by immersing the membranes in a dopamine solution for 24 h, and subsequently grafted DMEDA onto the PDA layer [45, 77]. However, in the present work a deposition time of 1 hour was chosen for the dopamine coating and for the co-deposition of dopamine and tannic acid, in order to obtain a dopamine coating of similar thickness for all the different functionalization performed.

Only membrane functionalization based on PDA, PDA-PEG, PDA-TA, which showed an effective increase in hydrophilicity from the contact angle measurements, were further subjected to filtration experiments.

5.2.3. Effects of Membrane Functionalization on Water Flux

Results of water filtration tests in cross-flow and dead-end modes are summarized in Figure 21 and Figure 22.

PVDF membranes exhibited zero water flux in both CF and DE modes, due to their high hydrophobicity, which prevents water penetration. Coating with polydopamine significantly increased the hydrophilicity of PVDF membranes – as previously seen from the contact angles) and made them permeable to water (Figure 21). On the contrary, PES-PDA membranes showed a decrease in the permeate water flux compared to pristine PES membranes, despite the increase in hydrophilicity. Furthermore, although the grafting of PEG and TA on the polydopamine layer led to a slight increase in membrane hydrophilicity, no noticeable increase in permeability was found (Figure 22).

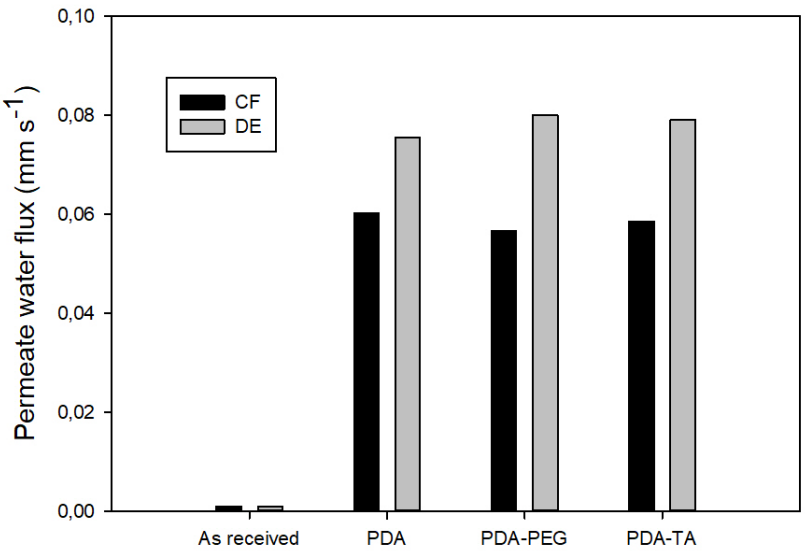

Figure 21. *Permeate water flux (mm s^{-1}) in CF and DE modes, for pristine and modified PVDF membranes.*

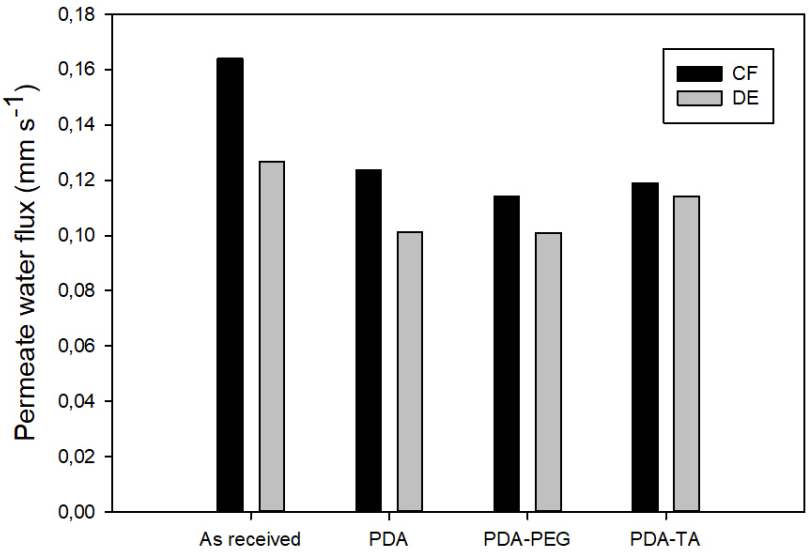

Figure 22. *Permeate water flux (mm/s) in CF and DE modes, for pristine and modified PES membranes.*

The explanation of these results lies in the reduction of the pore diameter caused by the deposition of functional materials onto the membrane surface and within the pores [34]. According to Poiseuille's law, the total permeate flow for a Newtonian fluid is proportional to the square of the pore diameter: $J \propto (\Delta p\, d^2)/(32\, \eta\, l)$, where Δp represents the pressure drop across the membrane and η the viscosity of the permeate. Consequently, even a small reduction in the average pore size could affect the filtering capacity.

5.2.4. Effects of Membrane Functionalization on Antifouling Potential

Antifouling potential of the functionalized membranes towards proteins was evaluated through filtration experiments, both in crossflow and dead-end modes, using water-BSA ($10\ \mathrm{mg\,mL^{-1}}$) as a model fouling solution. It is worth mentioning that a 10 times lower BSA concentration was used, compared to the amount previously employed in *Chapter 1 – Fouling Phenomena*, section 5: Experimental Study on the Effect of Pumping Systems on Fouling Evolution. Such choice was aimed at reducing the possible interactions between the polydopamine layer and the deposited proteins [39].

Since pristine PVDF membrane is not permeable to aqueous solutions, comparing the antifouling potential of pristine and modified PVDF membranes by monitoring the permeate flux decline was not possible. Contrary to expectations, PVDF-PDA, PVDF-PDA-PEG and PVDF-PDA-TA showed similar evolution of permeate flow over time (Figure 23 and Figure 24), therefore, the further increase in hydrophilicity due to the grafting of PEG and TA did not significantly affect the antifouling potential of the modified membranes during the filtration process.

However, several studies have demonstrated that although protein adsorption in the absence of filtration is reduced on very hydrophilic microfiltration membranes [78, 79], the filtrate flux during actual protein filtration is often found to be largely independent of the membrane surface chemistry [80, 81]. Mueller and Davis [81] found very similar flux decline profiles during constant pressure BSA solution filtration through microporous polyethylene membranes both untreated and after hydrophilizing treatments. They found that reduction in protein adsorption on hydrophilic membranes has relatively little effect on the filtrate flux, since protein fouling occurs primarily by the physical deposition on the membrane surface of large protein aggregates formed during the filtration process [82]. Moreover, Mueller and Davis observed that increasing the protein concentration in the filtering solution leads to a higher and faster membrane fouling, since the tendency of proteins to form aggregates becomes greater [81].

Jiang, He, Li et al. used water-BSA $1\ \mathrm{mg\ mL^{-1}}$ as a filtering solution, which is a BSA concentration ten times smaller than that used in the present work. They found visible improvements in the evolution of permeate flow during filtration through dopamine-coated membranes compared to the permeate flux through the pristine hydrophobic membrane [31, 83, 84]. This suggests that membrane hydrophilization acquires greater importance in the prevention of fouling phenomena when the filtering solution has a lower protein concentration, due to the lesser tendency of proteins to aggregate.

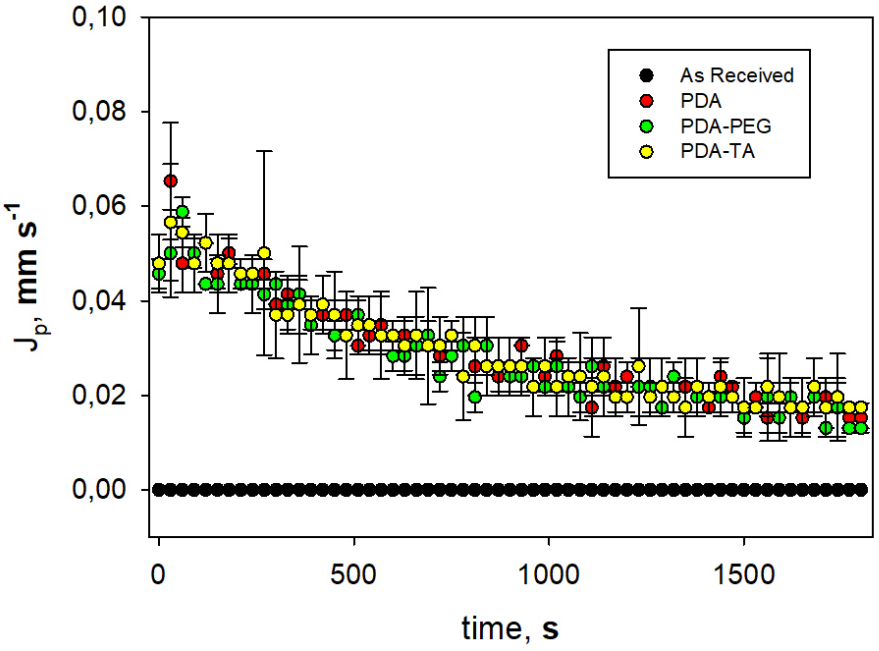

Figure 23. *Evolution of permeate flow over time in crossflow filtration mode through pristine and functionalized PVDF membranes.*

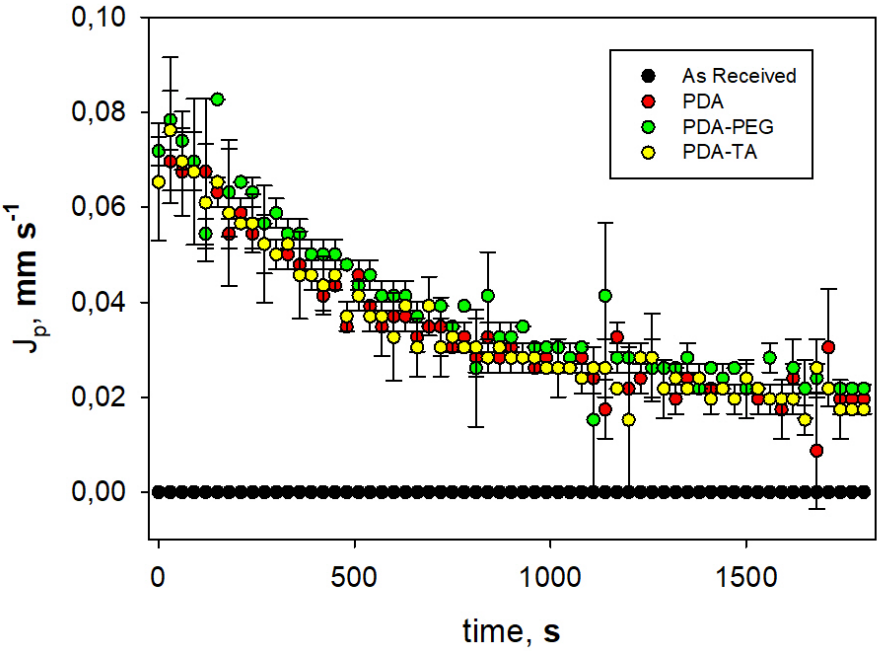

Figure 24. *Evolution of permeate flow over time in dead-end filtration mode through pristine and functionalized PVDF membranes.*

In the first stages of the filtration process, the hydrophilization of the PES membrane by dopamine deposition, combined with the cleaning effect of the crossflow configuration, leads to a higher initial permeate flow than that of the pristine PES membrane (Figure 25). In crossflow filtration mode, the shearing effect of the tangential feed flow reduces the protein aggregation and their physical deposition on the membrane surface that occur during the first stage of protein fouling [80]. Under the lesser presence of protein aggregates, membrane hydrophilization may acquire greater importance in the prevention of fouling phenomena.

However, this improvement is only appreciable in the first phase of the filtration process, after which the permeate flux through the PES-PDA membrane drastically decreases, becoming lower than that of the pristine membrane. Furthermore, during the whole filtration process, the PES-PDA-PEG and PES-PDA-TA membranes exhibited a lower permeate flow compared to that of the pristine membrane, showing no improvement in the antifouling properties. Lower fluxes for the functionalized membranes might be due to the reduction of pore size caused by the functionalization itself. In fact, smaller pores are more easily subject to occlusion by protein aggregates, which are inevitably formed also in the crossflow filtration process, despite the cleaning effect of the tangential feed flow [34].

In the dead-end mode, the pristine and all the functionalized PES membranes exhibit very similar trends of permeate flux over time. These results are consistent with the findings reported previously. In the absence of a tangential flux and under high concentration of the fouling solution, the dead-end filtration mode promotes the formation of large protein aggregates, rapidly leading to membrane fouling, which is largely independent from the membrane surface chemistry [79, 81, 85].

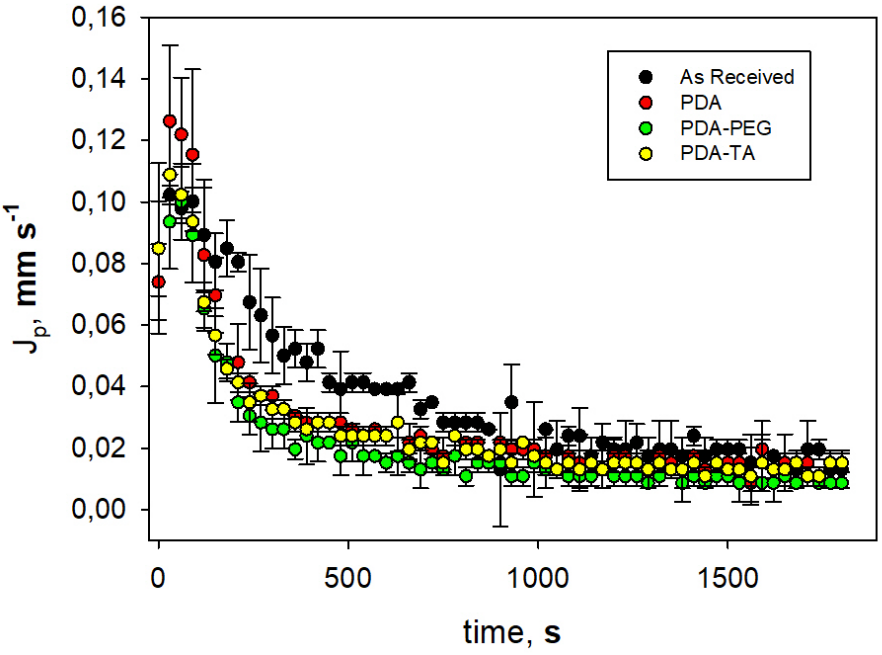

Figure 25. *Evolution of permeate flow over time in crossflow filtration mode through pristine and functionalized PES membranes.*

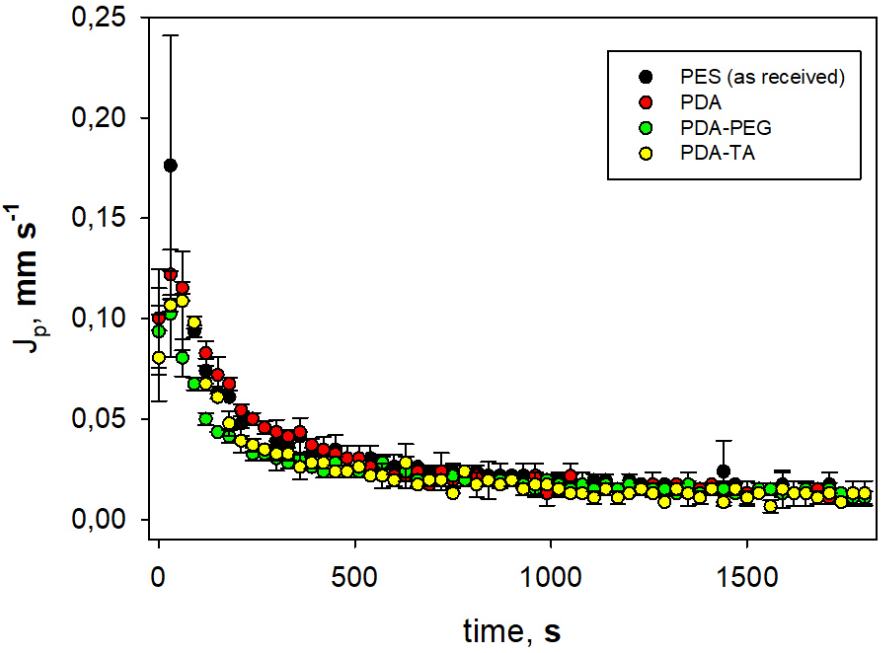

Figure 26. *Evolution of permeate flow over time in dead-end filtration mode through pristine and functionalized PES membranes.*

5.2.4. Effects of Membrane Functionalization on Protein Rejection

As regards the concentration of BSA in the permeate, it is always lower than the feed solution concentration, precisely because of the fouling phenomena. In fact, part of the BSA that has not crossed the membrane, deposited onto the membrane surface and within the pores, causing the observed permeate flow decrease. Furthermore, for all the CF tests, the concentration of BSA in the permeate is higher than that in DE (Figure 27 and Figure 28). These findings are justified by the working principle of the peristaltic pumps employed for the CF filtration mode. Indeed, peristaltic flux is characterized by the cyclic oscillation of the local flowrate resulting in pressure fluctuations, which helps BSA molecules permeation by creating a more loose fouling layer on the membrane surface.

Figure 27 shows that, for PVDF membranes, the grafting of PEG and TA on the polydopamine layer led to a mild increase in the BSA permeate concentration, both in DE and CF modes. However, this increase is so slight that it cannot confirm the improvement in antifouling potential. On the other hand, for PES membranes (Figure 28), the grafting of PEG and TA led to a halving of the BSA concentration in the permeate, both in CF and DE. This indicates a greater tendency to fouling, attributable to the pore size decrease, confirming the results obtained for permeate flux.

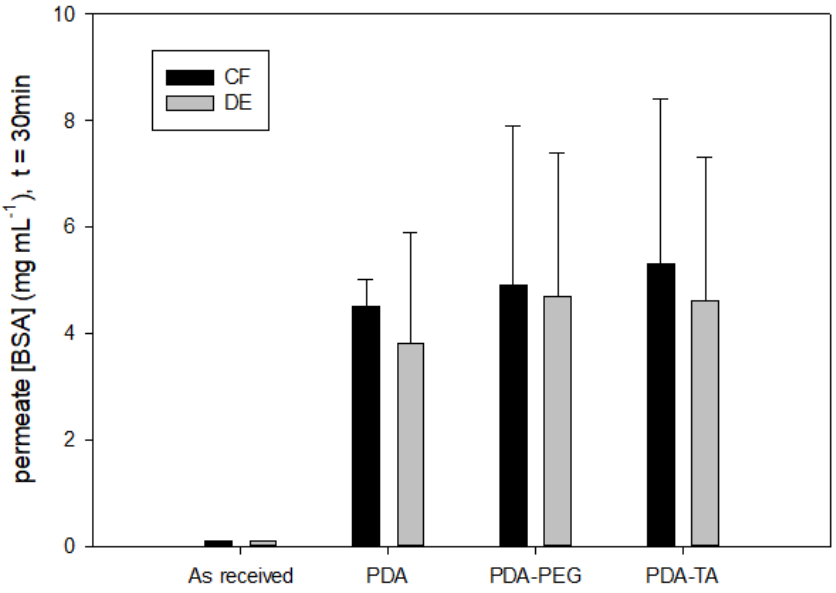

***Figure 27**. BSA concentrations (g mL^{-1}) of permeate and retentate in CF and DE filtration throw pristine and functionalized PVDF membranes.*

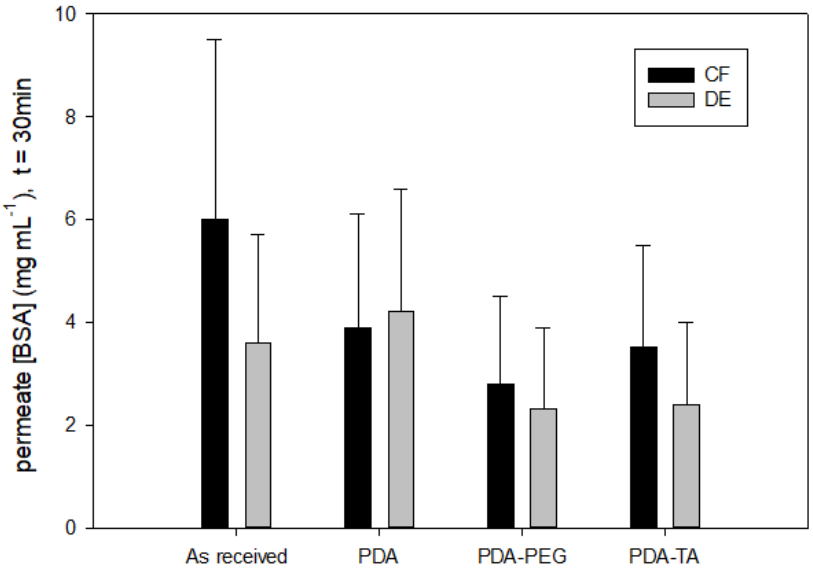

***Figure 28.** BSA concentrations (g mL^{-1}) of permeate and retentate in CF and DE filtration throw pristine and functionalized PES membranes.*

6. Antifouling Membranes: Tailoring the Nanostructure to Improve Fouling Resistance

The following sections are part of a research study carried out at the University of Notre Dame, Indiana, in collaboration with Dr. Phillip's WATER lab. The presented experimental work distances itself from the study of fouling through a microfluidic approach to focus on the development of tailorable membranes suitable for antifouling functionalization, starting from the selection of the polymers which will constitute the structure of the membranes. The use of microfluidics to assess the antifouling performances of the developed membranes represents an interesting future perspective.

6.1 Development and Characterization of Tunable, Solvent Resistant, Nanoporous Membranes Suitable for Antifouling Functionalization via SI-ATRP

Membrane functionalization is a promising approach to fouling mitigation. Indeed, by modifying the structure of the membranes at the nano-scale through the inclusion of antifouling molecules such as polyzwitterions, it is possible to prevent deposition by acting on both the pre-fouling and the adsorption/pore blocking stages. Nevertheless, not all membranes are suitable for functionalization. Modification procedures, such as grafting, often involve the use of solvents which can create harsh environments that degrade the membrane structure; it is therefore essential for a membrane not only to possess the right moieties for antifouling modifications, but also a chemical nature that ensures resistance to solvents.

In the following section, the growth of polyzwitterions via surface initiated atom transfer radical polymerization (SI-ATRP) was selected as a target antifouling functionalization method to develop a set of tunable, solvent resistant, nanoporous

membranes characterized by the presence of moieties that can serve as grafting sites for the initiator (i.e. bromoisobutyryl bromide, BIBBr). To do so, different statistical poly(trifluoroethyl methacrylate-*co*-oligo(ethylene glycol) methyl ether methacrylate-*co*-glycidyl methacrylate-*co*-hydroxyethyl methacrylate) (P(TFEMA-OEGMA-GMA-HEMA)) copolymers were synthesized by varying the relative amounts of GMA and HEMA and membranes were subsequently fabricated via nonsolvent induced phase separation (NIPS) methods.

Owing to the peculiar self-assembled nanostructure of the polymeric membrane, the GMA and HEMA units line the pore walls and are responsible for both resistance to solvents and presence of a functional site. Indeed, the oxirane groups of GMA can be crosslinked via acid catalyzed ring opening reaction, whereas HEMA presents a hydroxy group that can be reacted with BIBBr upon membrane casting. Membranes permeability and neutral solute rejection were thus evaluated and BIBBr was grafted using two different solvents, i.e., toluene and hexane, to investigate the changes in the nanostructure caused by the solvent environment. Finally, SI-ATRP was carried out on the initiator-functionalized membranes using [2-(Methacryloyloxy)ethyl]dimethyl-(3-sulfopropyl)ammonium hydroxide (DMAPS) as a zwitterionic monomer.

6.2. Experimental

6.2.1. Materials

All the chemicals were purchased from Fischer Scientific, USA, unless noted otherwise. Trifluoroethyl methacrylate (TFEMA), oligo(ethylene glycol) methyl ether methacrylate ($M_n = 500\ \mathrm{g\ mol^{-1}}$) (OEGMA), glycidyl methacrylate (GMA) and hydroxyethyl methacrylate (HEMA) were passed through a basic alumina (VWR, USA) column to purify them before the copolymer synthesis. Toluene and dimethylformamide were used as solvents for the free radical polymerization of the parent copolymer. Deionized (DI) water (Milli-Q

Advantage A10, Milli-Q, USA) was employed for the preparation of all the aqueous solutions used for permeability tests, filtration cells rinsing and for the storage of the membranes. A commercial poly(vinylidene fluoride) (PVDF) ultrafiltration membrane (PV400 ultrafiltration membrane, Nanostone Water, Inc., USA) was employed as a support during membrane casting.

α–bromoisobutyryl bromide (BIBBr) and [2-(Methacryloyloxy)ethyl]dimethyl-(3-sulfopropyl)ammonium hydroxide (DMAPS) were respectively used as the initiator and the monomer for SI-ATRP. $CuBr$ and $CuBr_2$ were instead used as catalysts and N,N,N', N", N"-Pentamethyldiethylenetriamine (PMDETA) as the ligand. Toluene, hexane, methanol and water were used in the various stages of the initiator grafting and polyzwitterion growth processes.

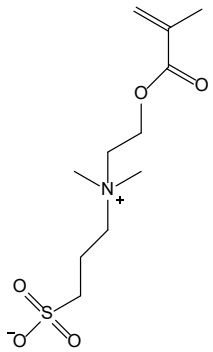

Figure 29. *Structure of [2-(Methacryloyloxy)ethyl]dimethyl-(3-sulfopropyl)ammonium hydroxide (DMAPS) monomer. Opposite charges can be observed on different groups, being DMAPS a zwitterion.*

6.2.2. Polymer Synthesis and Characterization

Poly(trifluoroethyl methacrylate-*co*-oligo(ethylene glycol) methyl ether methacrylate-*co*-glycidyl methacrylate) (P(TFEMA-OEGMA-GMA)), poly(trifluoroethyl methacrylate-*co*-oligo(ethylene glycol) methyl ether methacrylate-*co*-glycidyl methacrylate-*co*-hydroxyethyl methacrylate) (P(TFEMA-OEGMA-GMA-HEMA)) and poly(trifluoroethyl methacrylate-*co*-oligo(ethylene glycol) methyl ether methacrylate-*co*-hydroxyethyl methacrylate) (P(TFEMA-OEGMA-HEMA) were synthesized via free radical polymerization

mechanism. The chemical structure of all the block polymers were confirmed by using ^{1}H nuclear magnetic resonance (^{1}H NMR) spectroscopy (Bruker Avance III 400 automated). Deuterated dimethyl sulfoxide (DMSO-d) was used as the solvent.

6.2.3. Membrane Casting and Functionalization

Self-assembled copolymer membranes were fabricated via nonsolvent induced phase separation (NIPS) method. 2,2,2-Trifluoroethanol was used as the solvent to prepare a 15% polymer solution, whereas isopropyl alcohol, diethyl ether and water were used for the coagulation baths.

Membrane crosslinking was performed by opening the GMA oxirane rings via acid catalyzed ring opening, using sulfuric acid (0.2 M) as the catalyst at different temperatures (e.g. T_{amb}, 40°C, 80°C and a controlled ramp from 60°C to 80°C). Reactions were carried out for 120 to 135 minutes. The degree of crosslinking was evaluated by measuring the amount of precipitated gel in N-Methyl-2-pyrrolidone (NMP) and dimethyl sulfoxide (DMSO).

Polyzwitterions growth via SI-ATRP was carried out by means of a "grafting from" approach. BIBBr was first grafted at different concentrations, e.g., $3\%_{w/v}$ in toluene for 20h at T_{amb} and 0.5, 1 and $5\%_{w/w}$ in hexane for 30 minutes and 20 hours (only $5\%_{w/w}$) at T_{amb}. BIBBr grafting was performed by immersing a casted membrane (or polymeric film) for the desired time in the reactive solution. Cleaning was performed using pure hexane and water. SI-ATRP of DMAPS was carried out as follows, at a molar ratio of the reaction mixture components of [DMAPS]:[$CuBr$]:[$CuBr_2$]:[PMDETA] $= 8:1:0.2:2.4$. 1.788 g of DMAPS, 0.115 g of $CuBr$, 0.036 g of $CuBr_2$ and 276 µl of PMDETA were dissolved in 20 ml of a 1:1 (on volume) water-methanol mixture under nitrogen blanking for at least 20 minutes. Upon complete dissolution, a BIBBr-functionalized membrane (or polymeric film) was immersed in the reaction mixture and the

reaction was carried out at 30°C for 1 or 3 hours under constant nitrogen flow. Cleaning was performed using DI water and methanol separately. All membranes and films were stored in DI water. ^{1}H NMR spectroscopy (Bruker Avance III 400 automated) in deuterated dimethyl sulfoxide was used to characterize polymer films, whereas FT-IR (Bruker) was used to characterize the functionalized membranes.

Permeability and neutral solute rejection tests were performed using polyethylene glycol water solutions (PEG) ($1\ \mathrm{g\ L^{-1}}$) in 10 ml dead-end stirred cells (EMD Millipore, USA). The following PEG molecular weights were employed: $1200\ \mathrm{kg\ mol^{-1}}$, $4000\ \mathrm{kg\ mol^{-1}}$, $9800\ \mathrm{kg\ mol^{-1}}$). Neutral solute concentration was measured via TOC analysis (Shimadzu TOC-L). Tests were performed at least twice to ensure reproducibility.

6.3. Results and Discussion

6.3.1. Synthesis and Characterization of the Parent Copolymers

The design and tunability of the parent copolymers can be described by considering the presence of three essential features for the final membrane, namely a continuous structure, pores and functional sites whose chemical nature is suitable for subsequent modification, i.e., zwitterion grafting and crosslinking.

The first feature is provided by TFEMA monomers, whose hydrophobic nature contributes to the formation of the active layer structure. Indeed, during the solvent-nonsolvent exchange phase of the NIPS process, such units thermodynamically rearrange separating from the other monomeric units to constitute the membrane backbone. During the separation of the microphases, the hydrophilic OEGMA chains parallelly rearrange to face towards the nonsolvent environment, gradually forming what, upon evaporation, will be the membrane pores. It is worth mentioning that nanoporous membranes such as those produced

in this work do not actually present real pores, but voids created by the thermal motion of the polymeric structure of the film itself.

GMA and HEMA units are responsible for the of presence functional sites lining the pore walls. The selection of the proper nature and amount of these units is of crucial importance for the properties of the final membrane. As a matter of fact, by possessing hydroxyl groups, HEMA can be easily reacted with BIBBr during the initiator grafting. Besides, the presence of a single functional moiety on such monomer allows better control of the initiator surface density, playing a key role in the antifouling potential of the functionalized membrane. On the other side, the epoxide rings characterizing GMA monomers cover a two-sided role. Indeed, when opened via acid catalyzed ring opening, such moieties not only allow for the formation of a highly crosslinked network, responsible for the resistance of the membrane to solvents, but also the formation of diols upon nucleophilic attack of water [86]. Modifying HEMA and GMA concentration in the parent copolymer enables, therefore, fine control on both initiator density and crosslinking degree, endowing the membrane of high tunability. Figure 30 shows the synthesized copolymers structures and schematizes the dangling moieties characterizing the pore walls of the casted membranes.

Three different copolymers were synthesized using the same amount of TFEMA and OEGMA but varying the amount of HEMA and GMA, therefore acting only on what will be the functional element of the final membrane. Two copolymers were synthesized by employing only HEMA or GMA as a functional unit in a 2:2:1 mass ratio, whereas the third one is characterized by the same amount of HEMA and GMA in a 4:4:1:1 mass ratio.

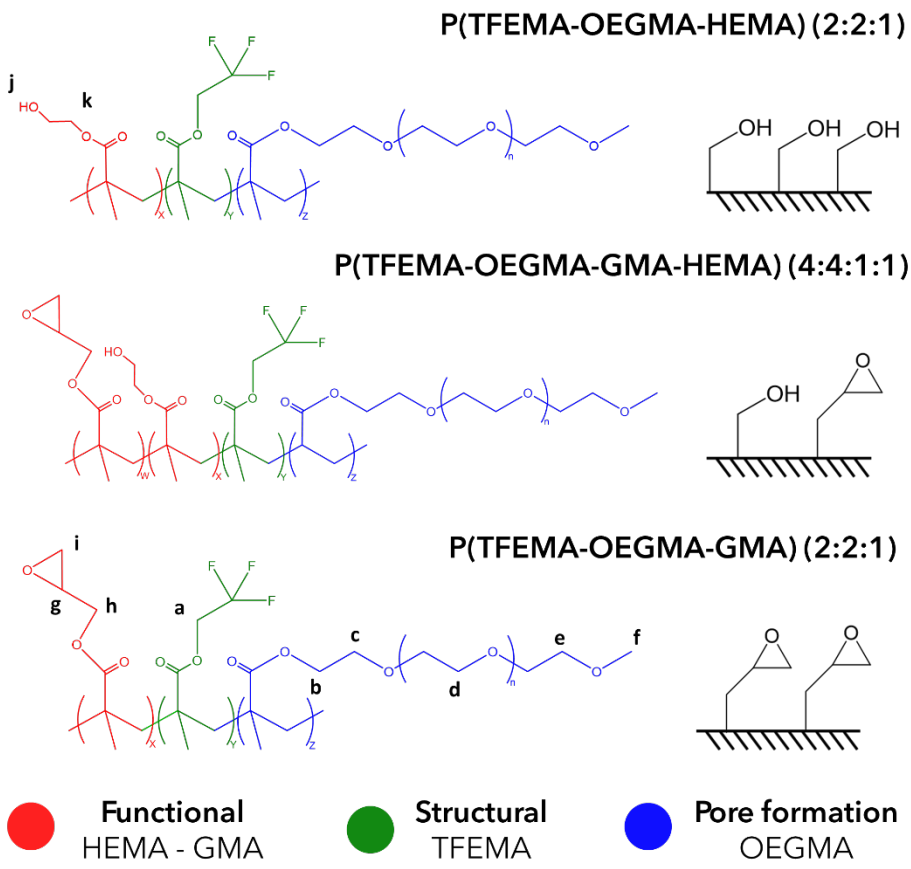

Figure 30. *Parent copolymer structure and schematic representation of the pore walls of a membrane. Letters label the characteristic peaks associated with* ^{1}H *NMR spectra for each component.*

Copolymer synthesis was carried out via free radical polymerization, where the appropriate solvent was to be selected in order to properly meet the constituents' nature and achieve the desired results. Toluene was used in the presence of GMA, whereas when only HEMA was included in the copolymer dimethylformamide was the selected solvent. ^{1}H NMR spectra allowed us to characterize the relative amounts of each monomer in the final copolymer (Figure 31). Clear differences can be observed between the presented spectra, normalized on TFEMA characteristic peak of constant magnitude at 4.65 ppm. Indeed, the presence of HEMA leads to the appearance of a peak at 4.8 ppm, associated with the hydroxyl group proton vibrations, whereas the presence of GMA can be addressed by the

two peaks at 2.65 and 2.8 ppm associated protons on the epoxide ring. In both cases, peak intensity varies with the relative monomer amount. As expected, the peak at 4.02 ppm, associated with OEGMA, is also characterized by constant magnitude, since no variation in the amounts of TFEMA and OEGMA was employed during the synthesis.

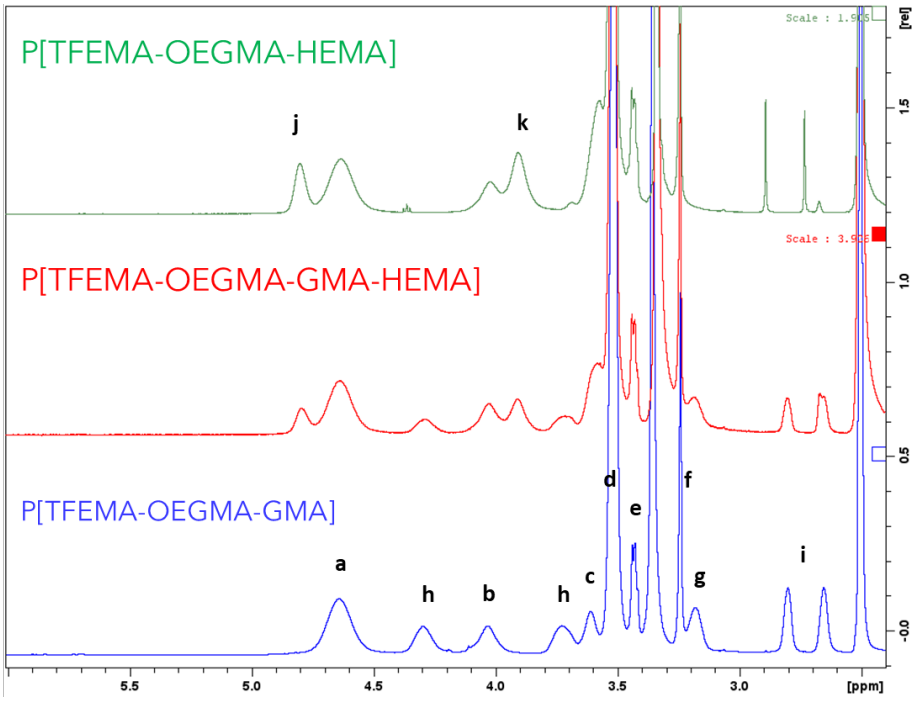

Figure 31. *^{1}H NMR spectra of the parent copolymer in DMSO-d.*

The integration of such characteristic peaks allowed for the quantification of the relative weight percentage of each monomer in the synthesized copolymer. Table 2 summarizes the obtained results. Percentages confirm the successful polymerization of the parent copolymers with slight variations from the theoretical values.

Table 2. *Copolymer %wt composition.*

	P(TFEMA-OEGMA-HEMA)	P(TFEMA-OEGMA-GMA-HEMA)	P(TFEMA-OEGMA-GMA)
TFEMA	25.35%	28.10%	30.14%
OEGMA	45.27%	40.96%	41.88%
HEMA	29.38%	13.09%	-
GMA	-	17.85%	27.98%

6.3.2. Parent and Crosslinked Membranes Characterization

Membranes were fabricated via nonsolvent induced phase separation (NIPS) following a 4 steps procedure. A 63 µm polymer film was first casted using a doctor blade on the PVDF support and let dry for 5 minutes. The dried membrane was thus plunged into the nonsolvent bath for a selected time (t_{bath}). Finally, in the fourth step, a second shorter drying (t_{evap}) was performed before immersing the membrane into a DI water bath. When films were fabricated a slightly different procedure was adopted. A 254 µm polymer film was casted without the need for a support and solvent was let dry for 15 minutes before a DI water bath.

Table 3. *Summary of the NIPS process conditions for the fabricated membranes.*

Copolymer	Membrane	Step 3 Nonsolvent, t_{bath}	Step 4 t_{evap}
P(TFEMA-OEGMA-HEMA)	H2O-H	-	Directly plunged
P(TFEMA-OEGMA-HEMA)	DEE20-H	Diethyl ether $t_{bath} = 90$ min	$t_{evap} = 20$ s
P(TFEMA-OEGMA-HEMA)	IPA2-75-H	Isopropyl alcohol $t_{bath} = 2$ min	$t_{evap} = 20$ s
P(TFEMA-OEGMA-HEMA)	IPA90-75-H	Isopropyl alcohol $t_{bath} = 90$ min	$t_{evap} = 75$ s
P(TFEMA-OEGMA-GMA-HEMA)	DEE20-GH	Diethyl ether $t_{bath} = 90$ min	$t_{evap} = 20$ s
P(TFEMA-OEGMA-GMA-HEMA)	DEE75-GH	Diethyl ether $t_{bath} = 90$ min	$t_{evap} = 75$ s
P(TFEMA-OEGMA-GMA-HEMA)	IPA2-75-GH	Isopropyl alcohol $t_{bath} = 2$ min	$t_{evap} = 75$ s
P(TFEMA-OEGMA-GMA-HEMA)	IPA90-75-GH	Isopropyl alcohol $t_{bath} = 90$ min	$t_{evap} = 75$ s

In order to obtain a membrane suitable for nanofiltration operations, two fundamental parameters of the NIPS process were optimized: the nature of the solvent, responsible for the creation of the membrane structure and the drying time, related to pore size and distribution [66, 87]. Two different nonsolvents were employed, isopropyl alcohol (IPA) and diethyl ether (DEE), respectively used for a coagulation bath time of 90 and 2 minutes and for 90 minutes. After the nonsolvent bath a second evaporation was carried out before plunging the membranes into a final water bath. 75 seconds were used as evaporation time for

the IPA bath, whereas two times were employed in the case of DEE, 75 and 20 seconds. Additionally, only for the P(TFEMA-OEGMA-HEMA) (2:2:1) membranes, the third step of the NIPS process was removed and a direct nonsolvent bath in DI water was used to obtain a very fast solvent-nonsolvent exchange rate. Table 3 summarizes the various conditions used for membrane fabrication.

Solvent stability was achieved by exploiting crosslinking of the epoxide rings. Ring opening was performed on P(TFEMA-OEGMA-GMA) (2:2:1) membranes via acid catalyzed ring opening reaction, which allowed to crosslink rings and generate diols on the membrane surface, therefore obtaining additional hydroxyl groups for the subsequent initiator grafting. Crosslinking was optimized by playing on the reaction time and temperature. Membranes were exposed for 120 minutes to a 0.2 M sulfuric acid solution at T_{amb}, 40°C and 80°C. Besides that, a temperature ramp was also explored, to account for the influence of the temperature on the polymeric film morphology. Indeed, a rapid exposure to a high temperature may lead to glass transition and thus to an altered final morphology of the active layer. In this case, parent membranes were first reacted for 60 minutes at 60°C and then for 75 minutes at 80°C.

Figure 32 shows the FT-IR spectra for the crosslinked P(TFEMA-OEGMA-GMA) membranes. Results show the positive impact of higher temperatures on the epoxide ring opening. Indeed, comparing the unreacted membrane spectra with the one belonging to the 80°C reacted one, the disappearance of the peak at 900 cm^{-1} associated with the -CO vibration in the epoxide ring can be observed, in favor of the appearance of a broad peak at ~3500 cm^{-1} related the presence of hydroxyl groups and thus to the generation of diols. Slight differences are observed between the spectra of the temperature ramp reacted membrane (60°C to 80°C) and the 80°C reacted one, however the former shower a much smoother surface, indicating lesser structural rearrangements. It was therefore selected as

the best candidate for the subsequent functionalization and will be termed as GMA-X from now on.

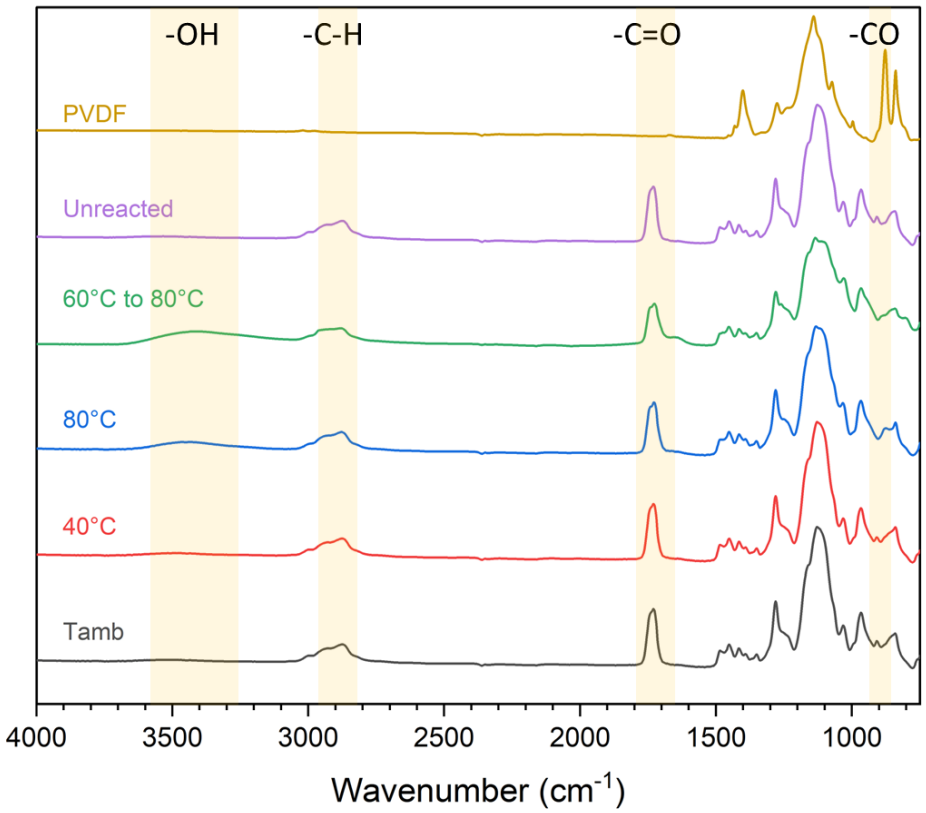

Figure 32. *FT-IR spectra of the crosslinked P(TFEMA-OEGMA-GMA) membranes at various reaction conditions. Spectra of the unreacted membrane and of support are shown for reference.*

To investigate the amount of crosslinked polymer, gel precipitation tests were carried out on films of the most promising candidate in both NMP and DMSO. The whole polymer film appeared to be impossible to dissolve, confirming, together with FT-IR data both a high degree of crosslinking and the presence of diols.

To study the best NIPS conditions and thus the suitability of the fabricated membranes for nanofiltration applications, water permeability measurements (L_p, $\mathrm{LMHbar^{-1}}$) were carried out.

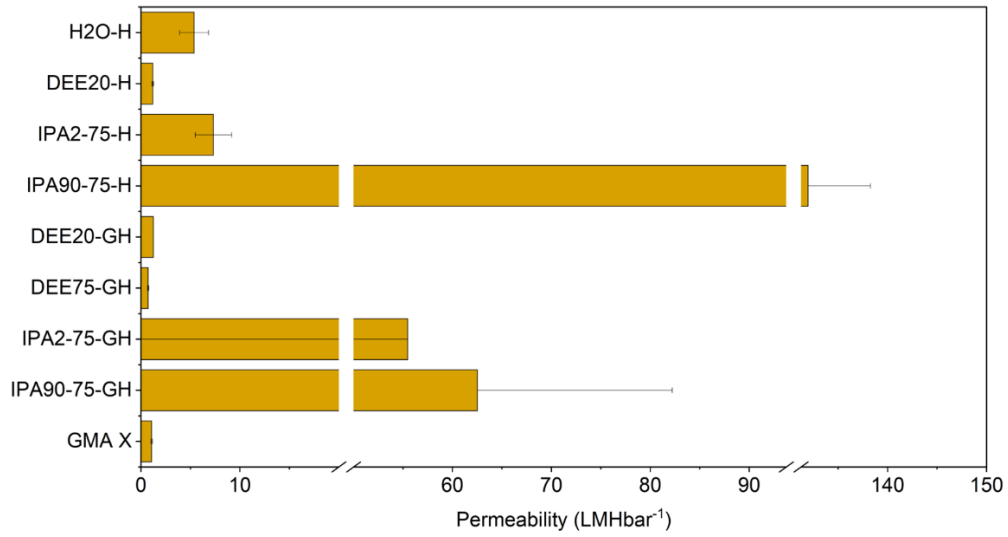

Figure 33. *Water permeability of the different membrane candidates produced via NIPS.*

Figure 33 shows water permeability values for the different fabricated membranes. According to results, the use of DEE for the nonsolvent bath and of an evaporation time of 20 seconds during the fourth step of the NIPS process allow the formation of a proper nanostructure which makes membranes suitable for nanofiltration, the best candidates are therefore the DEE20-H and DEE20-GE. Regarding the GMA-X membranes, the NIPS process was carried out using a 90 minutes IPA bath and an evaporation time of 75 seconds. Such membranes were then crosslinked as previously described and also selected as suitable candidates.

Neutral solute rejection tests were thus performed on the DEE20-H, DEE20-GE and GMA-X membranes, to evaluate the molecular weight cut off (MWCO). Figure 34 better summarizes the L_p values and shows the observed rejection curves for the selected membranes. All the membranes show similar rejection values, with a MWCO slightly below 9800 kDa.

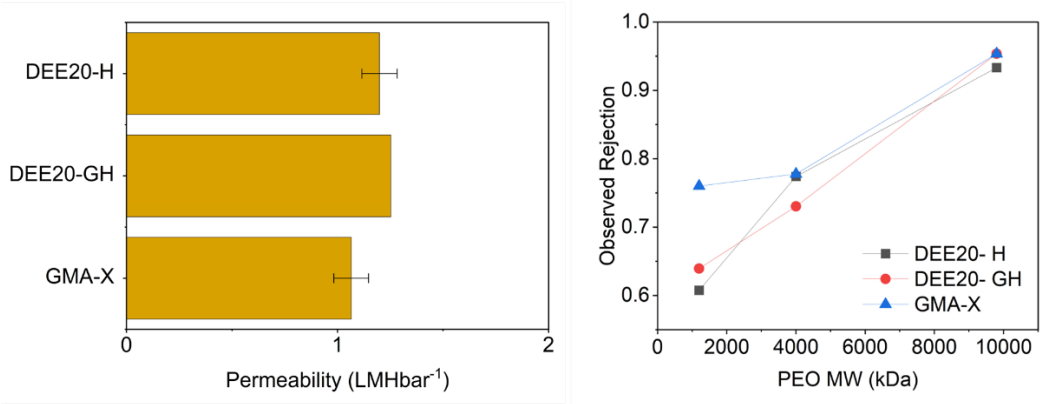

Figure 34. *Permeability and observed rejection values for DEE20-H, DEE20-GH and GMA-X membranes.*

6.3.3. Initiator Grafting and polyDMAPS growth via SI-ATRP

A "grafting from" strategy was adopted to react the BIBBr with the casted membranes. In this way the membrane surface was seeded with a specific amount of initiator, becoming ready for the subsequent growth of polyzwitterions as schematized in Figure 35.

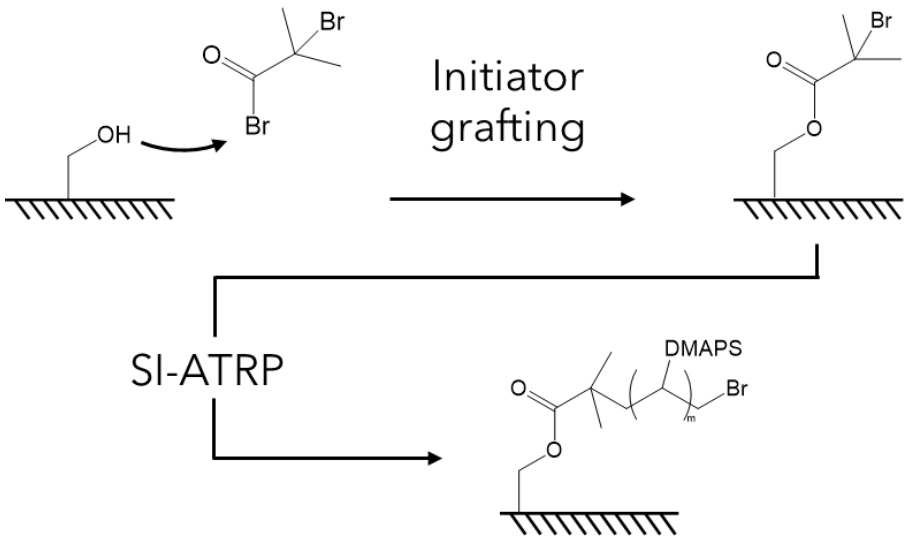

Figure 35. *Schematic representation of the "grafting from" growth of polyDMAPS on the membrane surface.*

Two different protocols were followed for the initiator grafting. In the first one, membranes were reacted in a $3\%_{w/v}$ BIBBr solution in toluene for 20 hours at

T_{amb}. FT-IR spectra of the initiator-functionalized membranes in toluene are shown in Figure 36.

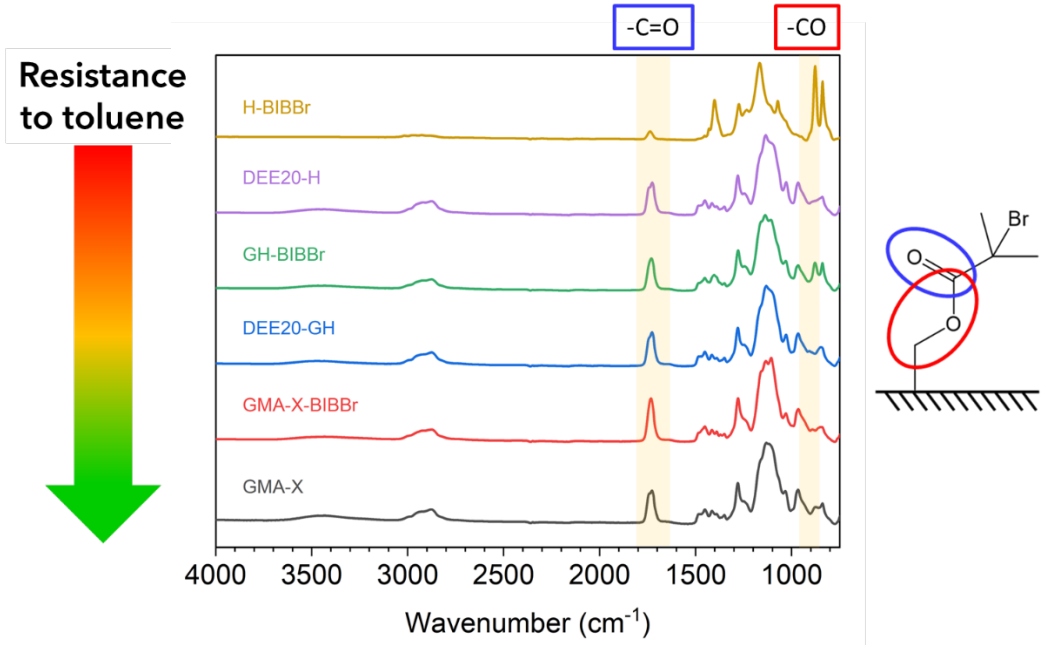

Figure 36. *FT-IR spectra of the initiator-functionalized membranes in toluene. Unreacted membranes spectra are shown for reference as well.*

An increase in toluene resistance can be observed going from the GMA-X to the DEE20-GH and finally to the DEE20-H functionalized membranes, with the H-BIBBr membrane being characterized by the almost complete absence of the active layer. Indeed, for such membrane the spectrum is comparable to the PVDF one showed in Figure 32. Although the characteristic peaks of BIBBr can be observed in the GH-BIBBr spectra, variations were observed analyzing multiple spots on the same sample, proving a modest resistance to toluene of the DEE20-SE membrane. The most successful grafting was obtained with the GMA-X membrane, whose resistance to toluene is directly related to crosslinking. A sharper peak at $\sim 1725\ cm^{-1}$ associated with the carbonyl bond and a peak at $900\ cm^{-1}$ are present in the GMA-X-BIBBr spectra, proving the grafting of the initiator.

Due to their low resistance to toluene, DEE20-H membranes were used for the second functionalization protocol, where three different initiator concentrations, namely 0.5, 1 and $5\%_{w/w}$ in hexane were used to graft BIBBr at T_{amb} for 30 minutes. A longer reaction time of 20 hours was as well at a concentration of $5\%_{w/w}$, with no further improvement. Both polymeric films and membranes were used to study this grafting protocol, the former to perform ^{1}H NMR analysis, the latter for FT-IR.

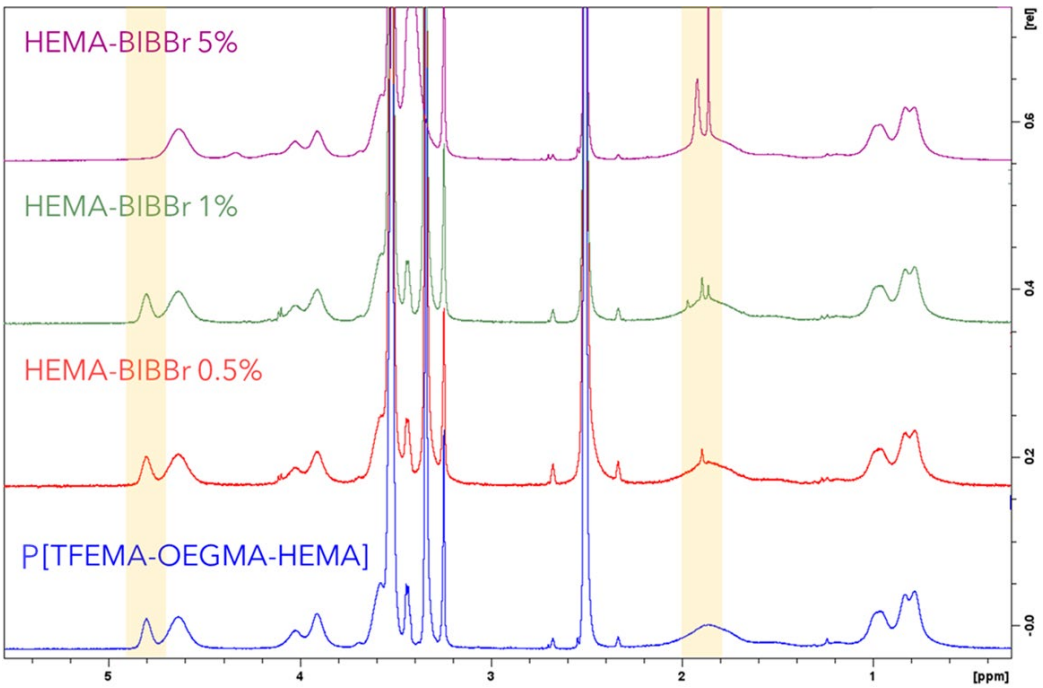

Figure 37. *^{1}H NMR spectra of P(TFEMA-OEGMA-HEMA) initiator-functionalized films at various concentrations and a reaction time of 30 minutes.*

^{1}H NMR spectra clearly show that using a concentration of $5\%_{w/w}$ of BIBBr allows a theoretically complete conversion of all the HEMA hydroxyl groups. Indeed, the characteristic peak of such moiety at 4.8 ppm disappears in favor of the appearance of a sharp peak at 1.8 ppm, associated with the BIBBr hydrogens vibration. Further analysis is needed to quantify the extent of initiator functionalization.

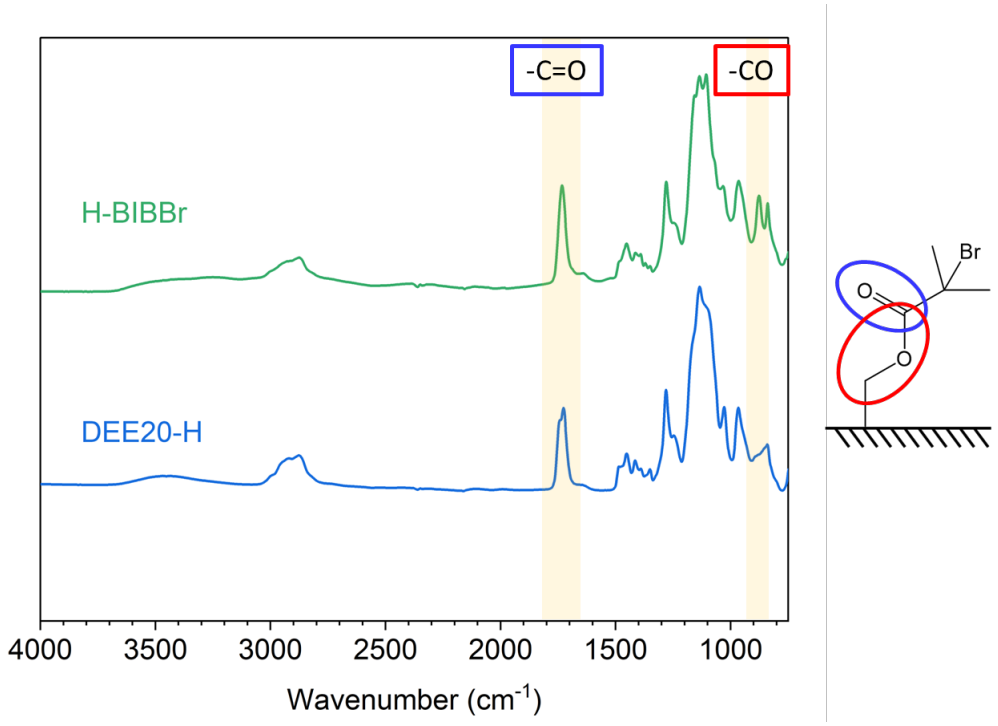

Figure 38. *FT-IR spectra of DEE20-H functionalized with BIBBr at a concentration of* $5\%_{w/w}$ *in hexane.*

FT-IR spectra were collected for the DEE20-H membrane functionalized with a BIBBr concentration of $5\%_{w/w}$in hexane (Figure 38). Spectra clearly show the presence of the characteristic peaks associated with the initiator and prove the resistance of the membrane to the employed solvent, besides the successful functionalization process. H-BIBBr membranes were therefore selected for the subsequent growth of polyDMAPS.

PolyDMAPS was polymerized on the initiator-functionalized membrane surface via SI-ATRP exploring two different reaction times, namely 1 and 3 hours, to investigate the effect of the polymer chain length. FT-IR spectra of polyDMAPS functionalized membranes demonstrate SI-ATRP was correctly carried out for the growth of polyzwitterion on the membrane surface (Figure 39). Indeed, a peak at $\sim 1725\ \mathrm{cm}^{-1}$ associated with the -C=O bond vibrations and one at $\sim 1125\ \mathrm{cm}^{-1}$ related to the -S=O bond can be observed, both belonging to the DMAPS monomers.

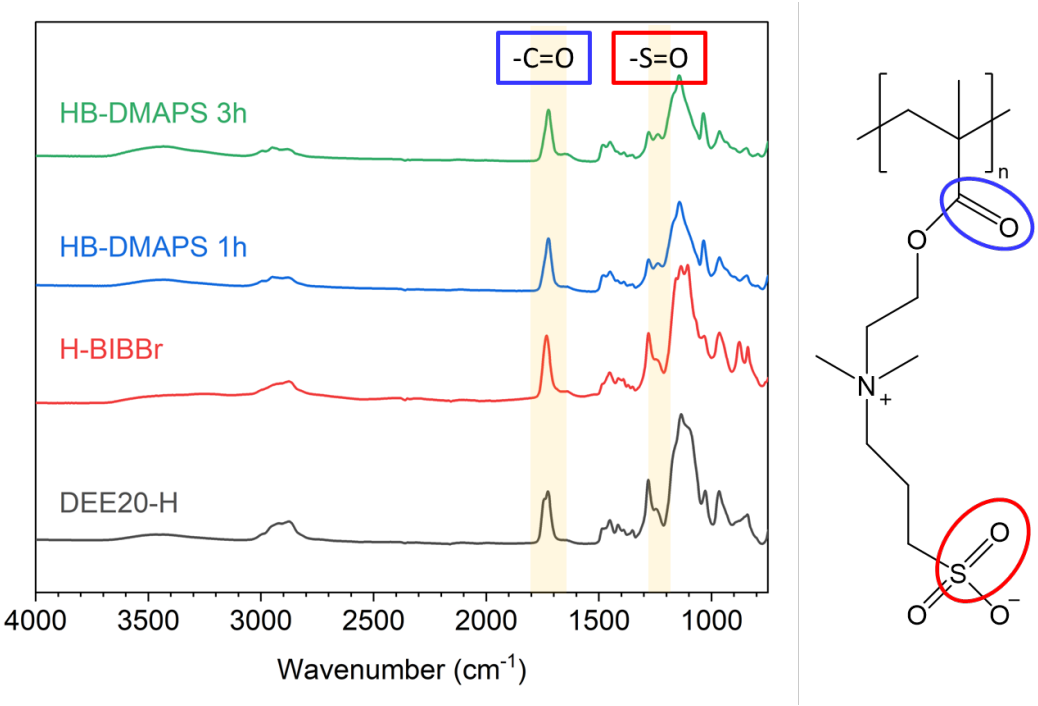

Figure 39. *FT-IR spectra of the polyDMAPS functionalized DEE20-H membranes for different reaction times.*

However, FT-IR alone is not sufficient to address any changes related to the different chain length. In fact, the spectra for the two reaction times employed for SI-ATRP are almost superimposable.

7. Conclusions

Fouling mitigation is a topic of high importance both for industries and researchers, as it represents the only way to cope with the unavoidable deposition of solutes that causes throughput and economic losses in membrane based separation processes.

In this chapter the main fouling mitigation strategies were reviewed, together with their advantages and limitations. Three classes of alleviation approaches were listed, each one acting on a specific stage of fouling. The optimization of process conditions is the first and most cost effective mitigation approach and takes action on all the fouling stages. Membrane cleaning, instead, is the most efficient method for flux recovery, despite being potentially dangerous for the membrane due to the use of aggressive chemicals. Greater focus was given to membrane modification techniques, which represent an interesting approach to prevent fouling, with specific attention to membrane functionalization and nano-structure modifications. In these regards, two experimental studies were then presented.

A first experimental study, carried out in a microfluidic filtration module, concerned the study of dopamine-based coatings on membrane hydrophilicity. Two different commercial membranes were investigated, a hydrophobic PVDF and a hydrophilic PES one. Further improvements in the hydrophilicity were also explored by means of additional grafting of molecules on dopamine-functionalized membranes. Despite the enhanced hydrophilicity for both membranes, no significative improvement was observed in terms of antifouling performances, possibly due to the combined effects of a reduction of the pore size reduction upon polydopamine deposition and of the interactions between the polydopamine layer and the BSA molecules.

The second experimental study involved the development of a set of tunable, solvent resistant membranes for nanofiltration applications. Such membranes

were designed to be suitable for the grafting of zwitterion via SI-ATRP. A "grafting from" approach was employed and polyDMAPS chains were successfully grown on the membrane surface.

References

[1] S.N. Jagannadh, H. Muralidhara, Electrokinetics methods to control membrane fouling, Industrial & engineering chemistry research 35(4) (1996) 1133-1140.
[2] C. Williams, R. Wakeman, Membrane fouling and alternative techniques for its alleviation, Membrane technology 2000(124) (2000) 4-10.
[3] T.M. Geislinger, T. Franke, Hydrodynamic lift of vesicles and red blood cells in flow - From F \aa hr \ae us \& Lindqvist to microfluidic cell sorting, Advances in Colloid and Interface Science 208 (2014) 161--176. https://doi.org/10.1016/j.cis.2014.03.002.
[4] J. Levesley, B. Bellhouse, Particulate separation using inertial lift forces, Chemical engineering science 48(21) (1993) 3657-3669.
[5] Y. Xu-Jiang, J. Dodds, D. Leclerc, Cake characteristics in crossflow and dead-end microfiltration, Filtration & separation 32(8) (1995) 795-798.
[6] Q. She, C.Y. Tang, Y.-N. Wang, Z. Zhang, The role of hydrodynamic conditions and solution chemistry on protein fouling during ultrafiltration, Desalination 249(3) (2009) 1079-1087.
[7] R. Wang, L. Shi, C.Y. Tang, S. Chou, C. Qiu, A.G. Fane, Characterization of novel forward osmosis hollow fiber membranes, Journal of membrane science 355(1-2) (2010) 158-167.
[8] B. Boissier, F. Lutin, M. Moutounet, A. Vernhet, Particles deposition during the cross-flow microfiltration of red wines—incidence of the hydrodynamic conditions and of the yeast to fines ratio, Chemical Engineering and Processing: Process Intensification 47(3) (2008) 276-286.
[9] R.W. Field, D. Wu, J.A. Howell, B.B. Gupta, Critical flux concept for microfiltration fouling, Journal of Membrane Science 100(3) (1995) 259--272. https://doi.org/10.1016/0376-7388(94)00265-Z.
[10] K. Lucas, S.D. Ahmad, M. Dehghani, T. Gaborski, J. McGrath, Critical flux behavior of ultrathin membranes in protein-rich solutions, Separation and Purification Technology 251 (2020) 117342.
[11] S.J. Pugh, G.F. Hewitt, H. Müller-Steinhagen, Fouling during the use of "fresh" water as coolant—The development of a "User Guide", Heat Transfer Engineering 30(10-11) (2009) 851-858.
[12] W. Wang, C.J. Roberts, Protein aggregation–mechanisms, detection, and control, International journal of pharmaceutics 550(1-2) (2018) 251-268.
[13] J. Haberkamp, M. Ernst, G. Makdissy, P.M. Huck, M. Jekel, Protein fouling of ultrafiltration membranes—investigation of several factors relevant for tertiary wastewater treatment, Journal of environmental engineering and science 7(6) (2008) 651-660.
[14] J.C.-T. Lin, D.-J. Lee, C. Huang, Membrane fouling mitigation: Membrane cleaning, Separation Science and Technology 45(7) (2010) 858-872.

[15] C.-W. Kang, J. Hua, J. Lou, W. Liu, E. Jordan, Bridging the gap between membrane bio-reactor (MBR) pilot and plant studies, Journal of Membrane Science 325(2) (2008) 861-871.
[16] C. Psoch, S. Schiewer, Anti-fouling application of air sparging and backflushing for MBR, Journal of Membrane Science 283(1-2) (2006) 273-280.
[17] S. Ebrahim, Cleaning and regeneration of membranes in desalination and wastewater applications: state-of-the-art, Desalination 96(1-3) (1994) 225-238.
[18] R. y Medioambiente, José Miguel Arnal, Beatriz García-Fayos and María Sancho Instituto de Seguridad Industrial, Expanding Issues in Desalination (2011) 63.
[19] M. Bagheri, S.A. Mirbagheri, Critical review of fouling mitigation strategies in membrane bioreactors treating water and wastewater, Bioresource Technology 258 (2018) 318-334.
[20] Z. Wang, Z. Wu, A review of membrane fouling in MBRs: characteristics and role of sludge cake formed on membrane surfaces, Separation Science and Technology 44(15) (2009) 3571-3596.
[21] Z. Wang, J. Ma, C.Y. Tang, K. Kimura, Q. Wang, X. Han, Membrane cleaning in membrane bioreactors: A review, Journal of membrane science 468 (2014) 276-307.
[22] K. Scott, Handbook of industrial membranes, Elsevier1995.
[23] E. Drioli, L. Giorno, Encyclopedia of membranes, Springer2016.
[24] F. Meng, S. Zhang, Y. Oh, Z. Zhou, H.-S. Shin, S.-R. Chae, Fouling in membrane bioreactors: An updated review, Water research 114 (2017) 151-180.
[25] S. Madaeni, Y. Mansourpanah, Chemical cleaning of reverse osmosis membranes fouled by whey, Desalination 161(1) (2004) 13-24.
[26] N. Porcelli, S. Judd, Chemical cleaning of potable water membranes: A review, Separation and purification technology 71(2) (2010) 137-143.
[27] C. Liu, S. Caothien, J. Hayes, T. Caothuy, T. Otoyo, T. Ogawa, Membrane chemical cleaning: from art to science, Pall Corporation, Port Washington, NY 11050 (2001).
[28] X. Shi, G. Tal, N.P. Hankins, V. Gitis, Fouling and cleaning of ultrafiltration membranes: A review, Journal of Water Process Engineering 1 (2014) 121--138. https://doi.org/10.1016/j.jwpe.2014.04.003.
[29] H. You, C. Huang, J. Pan, S. Chang, Behavior of membrane scaling during crossflow filtration in the anaerobic MBR system, Separation science and technology 41(7) (2006) 1265-1278.
[30] C. Causserand, B. Pellegrin, J.-C. Rouch, Effects of sodium hypochlorite exposure mode on PES/PVP ultrafiltration membrane degradation, Water research 85 (2015) 316-326.
[31] Y. He, L. Xu, X. Feng, Y. Zhao, L. Chen, Dopamine-induced nonionic polymer coatings for significantly enhancing separation and antifouling properties of polymer membranes: Codeposition versus sequential deposition, Journal of Membrane Science 539 (2017) 421-431.

[32] F. Li, J. Meng, J. Ye, B. Yang, Q. Tian, C. Deng, Surface modification of PES ultrafiltration membrane by polydopamine coating and poly (ethylene glycol) grafting: Morphology, stability, and anti-fouling, Desalination 344 (2014) 422-430.
[33] D.J. Miller, D.R. Dreyer, C.W. Bielawski, D.R. Paul, B.D. Freeman, Surface modification of water purification membranes, Angewandte Chemie International Edition 56(17) (2017) 4662-4711.
[34] Z. Yan, Y. Zhang, H. Yang, G. Fan, A. Ding, H. Liang, G. Li, N. Ren, B. Van der Bruggen, Mussel-inspired polydopamine modification of polymeric membranes for the application of water and wastewater treatment: A review, Chemical Engineering Research and Design 157 (2020) 195-214.
[35] H. Lee, S.M. Dellatore, W.M. Miller, P.B. Messersmith, Mussel-inspired surface chemistry for multifunctional coatings, science 318(5849) (2007) 426-430.
[36] J. Jiang, L. Zhu, L. Zhu, B. Zhu, Y. Xu, Surface characteristics of a self-polymerized dopamine coating deposited on hydrophobic polymer films, Langmuir 27(23) (2011) 14180-14187.
[37] S. Kasemset, L. Wang, Z. He, D.J. Miller, A. Kirschner, B.D. Freeman, M.M. Sharma, Influence of polydopamine deposition conditions on hydraulic permeability, sieving coefficients, pore size and pore size distribution for a polysulfone ultrafiltration membrane, Journal of Membrane Science 522 (2017) 100-115.
[38] C. Steffi, Z. Shi, C.H. Kong, W. Wang, Bioinspired polydopamine and polyphenol tannic acid functionalized titanium suppress osteoclast differentiation: a facile and efficient strategy to regulate osteoclast activity at bone–implant interface, Journal of the Royal Society Interface 16(152) (2019) 20180799.
[39] L.-P. Zhu, J.-H. Jiang, B.-K. Zhu, Y.-Y. Xu, Immobilization of bovine serum albumin onto porous polyethylene membranes using strongly attached polydopamine as a spacer, Colloids and Surfaces B: Biointerfaces 86(1) (2011) 111-118.
[40] M. Ali, S. Nasir, W. Ensinger, Stereoselective detection of amino acids with protein-modified single asymmetric nanopores, Electrochimica Acta 215 (2016) 231-237.
[41] K. Wu, X. Song, S. Cui, Z. Li, Y. Jiao, C. Zhou, Immobilization of bovine serum albumin via mussel-inspired polydopamine coating on electrospun polyethersulfone (PES) fiber mat for effective bilirubin adsorption, Applied Surface Science 451 (2018) 45-55.
[42] L.M. Hamming, P.B. Messersmith, Fouling resistant biomimetic poly (ethylene glycol) based grafted polymer coatings, Mater. Matters 3(52) (2008).
[43] X. Yang, L. Yan, Y. Wu, Y. Liu, L. Shao, Biomimetic hydrophilization engineering on membrane surface for highly-efficient water purification, Journal of Membrane Science 589 (2019) 117223.
[44] T.S. Sileika, D.G. Barrett, R. Zhang, K.H.A. Lau, P.B. Messersmith, Colorless multifunctional coatings inspired by polyphenols found in tea, chocolate, and wine, Angewandte Chemie 125(41) (2013) 10966-10970.

[45] B.P. Tripathi, P. Das, F. Simon, M. Stamm, Ultralow fouling membranes by surface modification with functional polydopamine, European Polymer Journal 99 (2018) 80-89.
[46] K. Aran, L.A. Sasso, N. Kamdar, J.D. Zahn, Irreversible, direct bonding of nanoporous polymer membranes to PDMS or glass microdevices, Lab on a Chip 10(5) (2010) 548-552.
[47] M. He, K. Gao, L. Zhou, Z. Jiao, M. Wu, J. Cao, X. You, Z. Cai, Y. Su, Z. Jiang, Zwitterionic materials for antifouling membrane surface construction, Acta biomaterialia 40 (2016) 142-152.
[48] S. Chen, J. Zheng, L. Li, S. Jiang, Strong resistance of phosphorylcholine self-assembled monolayers to protein adsorption: insights into nonfouling properties of zwitterionic materials, Journal of the American Chemical Society 127(41) (2005) 14473-14478.
[49] A. Erfani, J. Seaberg, C.P. Aichele, J.D. Ramsey, Interactions between biomolecules and zwitterionic moieties: a review, Biomacromolecules 21(7) (2020) 2557-2573.
[50] A. Lezov, P. Vlasov, G. Polushina, A. Lezov, Effect of chemical structure and charge distribution on behavior of polyzwitterions in solution, Macromolecular Symposia, Wiley Online Library, 2012, pp. 17-24.
[51] J.D. Delgado, J.B. Schlenoff, Static and dynamic solution behavior of a polyzwitterion using a Hofmeister salt series, Macromolecules 50(11) (2017) 4454-4464.
[52] S. Chen, L. Li, C. Zhao, J. Zheng, Surface hydration: Principles and applications toward low-fouling/nonfouling biomaterials, Polymer 51(23) (2010) 5283-5293.
[53] M. Ulbricht, Advanced functional polymer membranes, Polymer 47(7) (2006) 2217-2262.
[54] P. Vana, Controlled radical polymerization at and from solid surfaces, Springer2016.
[55] Y.-S. Guo, X.-D. Weng, B. Wu, Y.-F. Mi, B.-K. Zhu, Y.-L. Ji, Q.-F. An, C.-J. Gao, Construction of nonfouling nanofiltration membrane via introducing uniformly tunable zwitterionic layer, Journal of Membrane Science 583 (2019) 152-162.
[56] W.-W. Yue, H.-J. Li, T. Xiang, H. Qin, S.-D. Sun, C.-S. Zhao, Grafting of zwitterion from polysulfone membrane via surface-initiated ATRP with enhanced antifouling property and biocompatibility, Journal of Membrane Science 446 (2013) 79-91.
[57] Y. Sui, X. Gao, Z. Wang, C. Gao, Antifouling and antibacterial improvement of surface-functionalized poly (vinylidene fluoride) membrane prepared via dihydroxyphenylalanine-initiated atom transfer radical graft polymerizations, Journal of membrane science 394 (2012) 107-119.
[58] N. Luo, S.M. Husson, D.E. Hirt, D.W. Schwark, Surface grafting of polyacrylamide from polyethylene-based copolymer film, Journal of applied polymer science 92(3) (2004) 1589-1595.

[59] Y. Chen, L. Ying, W. Yu, E. Kang, K. Neoh, Poly (vinylidene fluoride) with grafted poly (ethylene glycol) side chains via the RAFT-mediated process and pore size control of the copolymer membranes, Macromolecules 36(25) (2003) 9451-9457.
[60] R. Zhang, Y. Liu, M. He, Y. Su, X. Zhao, M. Elimelech, Z. Jiang, Antifouling membranes for sustainable water purification: strategies and mechanisms, Chemical Society Reviews 45(21) (2016) 5888-5924.
[61] Y. Zhang, N.E. Almodovar-Arbelo, J.L. Weidman, D.S. Corti, B.W. Boudouris, W.A. Phillip, Fit-for-purpose block polymer membranes molecularly engineered for water treatment, npj Clean Water 1(1) (2018) 1-14.
[62] F.S. Bates, M.A. Hillmyer, T.P. Lodge, C.M. Bates, K.T. Delaney, G.H. Fredrickson, Multiblock polymers: Panacea or Pandora's box?, Science 336(6080) (2012) 434-440.
[63] J.R. Hoffman, W.A. Phillip, 100th anniversary of macromolecular science viewpoint: integrated membrane systems, ACS Macro Letters 9(9) (2020) 1267-1279.
[64] J.R. Hoffman, W.A. Phillip, Dual-functional nanofiltration membranes exhibit multifaceted ion rejection and antifouling performance, ACS applied materials & interfaces 12(17) (2020) 19944-19954.
[65] J.L. Sargent, D.J. Hoss, W.A. Phillip, B.W. Boudouris, Solution self-assembly behavior of A-B-C triblock polymers and the implications for nanoporous membrane fabrication, Journal of Applied Polymer Science 135(24) (2018) 45531.
[66] J.U.M. Garcia, Understanding Membrane Formation in Nonsolvent-Induced Phase Separation, University of California, Santa Barbara2020.
[67] N.I. Mat Nawi, M.R. Bilad, N. Zolkhiflee, N.A.H. Nordin, W.J. Lau, T. Narkkun, K. Faungnawakij, N. Arahman, T.M.I. Mahlia, Development of a novel corrugated polyvinylidene difluoride membrane via improved imprinting technique for membrane distillation, Polymers 11(5) (2019) 865.
[68] J.H. Jang, J. Lee, S.-Y. Jung, D.-C. Choi, Y.-J. Won, K.H. Ahn, P.-K. Park, C.-H. Lee, Correlation between particle deposition and the size ratio of particles to patterns in nano-and micro-patterned membrane filtration systems, Separation and Purification Technology 156 (2015) 608-616.
[69] N.U. Barambu, M.R. Bilad, Y. Wibisono, J. Jaafar, T.M.I. Mahlia, A.L. Khan, Membrane surface patterning as a fouling mitigation strategy in liquid filtration: A review, Polymers 11(10) (2019) 1687.
[70] B.J. De Gans, P.C. Duineveld, U.S. Schubert, Inkjet printing of polymers: state of the art and future developments, Advanced materials 16(3) (2004) 203-213.
[71] Z.-X. Low, Y.T. Chua, B.M. Ray, D. Mattia, I.S. Metcalfe, D.A. Patterson, Perspective on 3D printing of separation membranes and comparison to related unconventional fabrication techniques, Journal of membrane science 523 (2017) 596-613.

[72] I.M. ElSherbiny, A.S. Khalil, M. Ulbricht, Surface micro-patterning as a promising platform towards novel polyamide thin-film composite membranes of superior performance, Journal of membrane science 529 (2017) 11-22.
[73] J.A. Kharraz, M. Bilad, H.A. Arafat, Simple and effective corrugation of PVDF membranes for enhanced MBR performance, Journal of membrane science 475 (2015) 91-100.
[74] M. Xie, W. Luo, S.R. Gray, Surface pattern by nanoimprint for membrane fouling mitigation: Design, performance and mechanisms, Water research 124 (2017) 238-243.
[75] F.M. Mirabella, Internal reflection spectroscopy: theory and applications, CRC Press1992.
[76] J. Lei, Z. Guo, PES asymmetric membrane for oil-in-water emulsion separation, Colloids and Surfaces A: Physicochemical and Engineering Aspects 626 (2021) 127096.
[77] K. Nayak, A. Kumar, P. Das, B.P. Tripathi, Amphiphilic antifouling membranes by polydopamine mediated molecular grafting for water purification and oil/water separation, Journal of Membrane Science 630 (2021) 119306.
[78] K.M. Persson, G. Ctu haiapannelli, A. Bottino, G. Träg, Porosity and protein adsorption of four polymeric microfiltration membranes, Journal of membrane science 76(1) (1993) 61-71.
[79] C.-C. Ho, A.L. Zydney, Effect of membrane morphology on the initial rate of protein fouling during microfiltration, Journal of Membrane Science 155(2) (1999) 261-275.
[80] H. Van der Horst, J. Hanemaaijer, Cross-flow microfiltration in the food industry. State of the art, Desalination 77 (1990) 235-258.
[81] J. Mueller, R.H. Davis, Protein fouling of surface-modified polymeric microfiltration membranes, Journal of membrane Science 116(1) (1996) 47-60.
[82] G. Belfort, R.H. Davis, A.L. Zydney, The behavior of suspensions and macromolecular solutions in crossflow microfiltration, Journal of membrane science 96(1-2) (1994) 1-58.
[83] J. Jiang, L. Zhu, L. Zhu, H. Zhang, B. Zhu, Y. Xu, Antifouling and antimicrobial polymer membranes based on bioinspired polydopamine and strong hydrogen-bonded poly (N-vinyl pyrrolidone), ACS applied materials & interfaces 5(24) (2013) 12895-12904.
[84] Y. Li, Y. Su, X. Zhao, X. He, R. Zhang, J. Zhao, X. Fan, Z. Jiang, Antifouling, high-flux nanofiltration membranes enabled by dual functional polydopamine, ACS applied materials & interfaces 6(8) (2014) 5548-5557.
[85] K.Y. Jee, J.S. Kim, J. Kim, Y.T. Lee, Effect of hydrophilic Cu3 (BTC) 2 additives on the performance of PVDF membranes for water flux improvement, Desalination and Water Treatment 57(38) (2016) 17637-17645.
[86] E.M. Muzammil, A. Khan, M.C. Stuparu, Post-polymerization modification reactions of poly (glycidyl methacrylate) s, RSC advances 7(88) (2017) 55874-55884.

[87] D.-M. Wang, A. Venault, J.-Y. Lai, Fundamentals of nonsolvent-induced phase separation, Hollow Fiber Membranes, Elsevier2021, pp. 13-56.

Chapter 3

Forward Osmosis Processes in Microfluidic Systems

Chapter Contents

1. Introduction

Water scarcity refers to the correlation between the supply of water resources and its demand and represents a high-impact global risk. Indeed, over the last century water usage has rapidly increased, with a current growth rate of 1% per year [1]. Water scarcity is actually a relative concept since the amount of physically accessible and suppliable water, together with its demand, may vary both in time and space due, for example due to a decrease in water quantity or quality. Population growth, economic development and climate change impact on the issue of scarcity as well, affecting a plethora of different sectors going from the food industry, unable to keep the production levels coming from agriculture to the domestic one. Proper water treatment and recovery processes are thus essential to optimally manage water resources while covering the current daily requirements.

A possible solution comes from forward osmosis (FO) processes, where water is recovered thanks to the presence of an osmotic pressure gradient across a semipermeable membrane, which separates the feed solution from a concentrated one, the draw solution [2]. FO processes are increasingly being used in several industrial fields, ranging from beverage production to heavy industry and are employed for wastewater management, product concentration and water recycling. However, different disadvantages characterize these processes, such as the effectiveness limit imposed by the osmotic equilibrium between the feed and draw solution, at which no water permeation would be possible due to the absence of a driving force. The main drawback of FO processes is actually represented by concentration polarization phenomena, both on the membrane surface and inside its bulk [3]. Indeed, the increase in solute concentration leads to a reduction of the effective driving force and consequently of the process throughput. It is thus essential to finely optimize the main process parameters affecting FO performance to maximize water recovery.

To this aim, microfluidics constitutes an innovative high potential tool for the investigation of the still debated aspects characterizing CP. Indeed, the use of such technologies was proven to be helpful for the visualization of the CP layer and for the optimization of the filtration module design in order to reduce its detrimental effects [4-6].

In the following sections, the main concepts related to FO will be reviewed. An experimental study on the optimization of process parameters will then be presented. Such investigation was carried out in the same microfluidic system used in the previous chapters and focuses on the role of CP on process throughput.

2. Forward Osmosis Processes

Forward osmosis (FO) is an emerging membrane separation technology that has gained much attention for many applications in the past few years. It is a separation process which exploits a semi-permeable membrane to draw water from dissolved solutes. The driving force for this separation is an osmotic pressure gradient, such that a draw solution at higher concentration compared with that of the feed solution is used to induce a net flow of water through the membrane, thus effectively separating the feed water from its solutes.

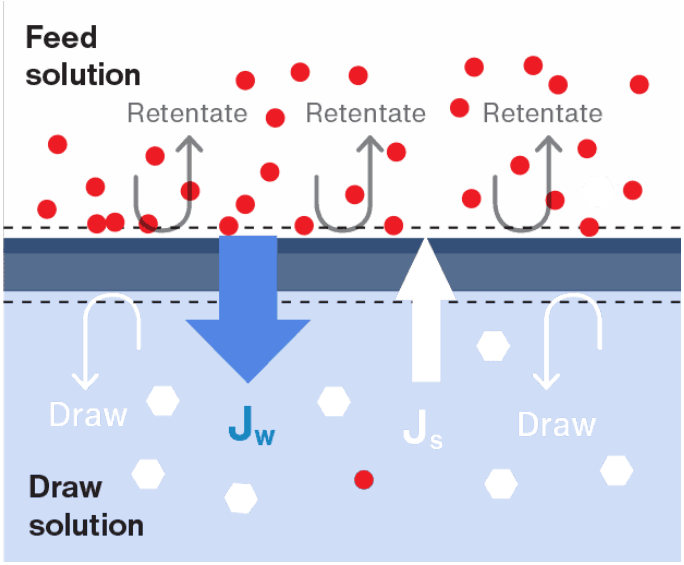

***Figure 1**. Schematic representation of a forward osmosis process. J_w and J_s represent the pure water flux and solute flux across the membrane, respectively. Adapted from [7].*

Osmotic pressure is a colligative property whose constitutive law was deduced empirically by van't Hoff, whose theory of dilute solutions supports the view that solute particles in a dilute solution behave in a similar fashion to that of gas molecules in a gaseous mixture. In analogy with gases, dilute solutions are also found to obey a similar equation concerning the variation of osmotic pressure as a function of solutes concentration:

$$\pi = cRT \qquad \textbf{(1)}$$

where π is the osmotic pressure in bar, c is the molar concentration of a solute ($\mathrm{mol\ L^{-1}}$), R is the gas constant equal to $0.08314\ \mathrm{L\ bar\ mol^{-1}\ K^{-1}}$ and T is the temperature in K. If the solute is an electrolyte which dissociates into ions, the van't Hoff coefficient i is introduced and Equation (1) becomes:

$$\pi = icRT \quad \textbf{(2)}$$

where i is a nondimensional factor representing the number of dispersed particles and can be equal to 2, 3, 4, …, depending on the number of ions produced by the dissociation of the electrolyte. For $NaCl$, $i = 2$.

The general equation describing water transport in osmotic processes is:

$$J_w = A(\Delta\pi - \Delta P) \quad \textbf{(3)}$$

where J_w is the water flux, A the water permeability constant, $\Delta\pi$ the osmotic pressure difference and ΔP the hydraulic pressure difference across the membrane. Usually, for FO processes $\Delta P = 0$, however a certain hydraulic pressure might be applied to compact the membrane and meet the manufacturer's operating conditions specifications. On the other side, solute flux (J_s) can be modeled by Fick's law:

$$J_s = B\Delta c \quad \textbf{(4)}$$

where B is the solute permeability coefficient, while Δc is the transmembrane solute concentration difference. Clearly, a solute will diffuse from a higher concentration zone, to a lower concentration one. In FO processes, solute diffusion can happen in both directions according to both the feed and draw solution composition; specifically, when solutes are transported from the draw to the feed side, the process is termed back diffusion [8].

2.1. Forward Osmosis Membranes

Forward osmosis membranes represent a relatively new type of membrane among the usual ones employed in filtration processes. The first tests on forward osmosis

were performed in the 1970s using reverse osmosis (RO) membranes. However, due to the structure of such membranes, which are characterized by an active layer and a thick porous support one, permeate fluxes were extremely low [9]. Indeed, an ideal FO membrane should have a thin support layer with low tortuosity, in order to provide a short path for the transport of water from the feed bulk to the draw solution across the active layer [10]. The first studies on the development of FO membranes were carried out on a plethora of materials, including animal bladders, cellulose, nitrocellulose, rubber and porcelain [11]. During the 1990s, a special membrane was developed by Osmotek Inc., currently known as Hydration Technologies Inc. (HTI) (Albany, USA). Such membrane was made of cellulose triacetate (CTA) and was characterized by the absence of a support layer and a polyester net to provide mechanical support. Results proved the better performance of CTA membranes produced by HTI in comparison with reverse osmosis membranes adapted for FO applications [11]. CTA membranes were the first polymeric membranes employed for FO operations and are characterized by several advantages, such as good hydrophilicity and an asymmetric structure that can be obtained in the same fabrication process, which make these membranes fouling resistant and easy to produce. However, the strict operating conditions at which CTA membranes can be used while preserving their integrity limit their applicability [12].

The performance of FO membranes critically depends on the efficient diffusion of solutes in the draw solution through the support layer, whose characteristics are therefore one of the most important factors in the design of the whole membrane. Indeed, differently from RO membranes, which are required to have a proper mechanical strength in order to resist to the applied pressure, optimized FO membranes are constituted by a comparable active layer (AL) and a much thinner and porous support layer (Figure 2) [13].

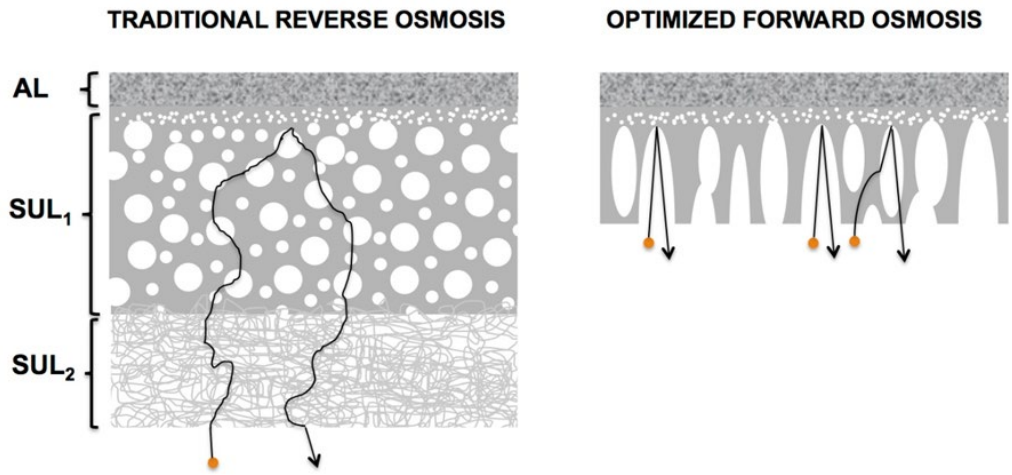

Figure 2. *Reverse osmosis and forward osmosis membrane section schematics. RO membranes are frequently characterized by two support layers for increased mechanical resistance [13].*

Three parameters are usually employed to describe FO membranes performance, namely the water flux (in L $m^{-2}h^{-1}$ or LMH) from the feed to the draw solution, solutes back flux (in g $m^{-2}h^{-1}$ or MH) and solute rejection, in %, from the feed to the draw solution side. Based on such parameters, CTA membranes are characterized by high rejection values due to the dense active layer and a high water flux, guaranteed by the thin support [13].

The water permeability (A) and solute permeability (B) coefficients are typically used to characterize a FO membrane. The former is a property of the active layer and affects the volume of water transported across the membrane surface at a given osmotic pressure. The latter, instead, is related to the selectivity of the active layer towards a specific solute, determining therefore its back diffusion. Membrane developers are interested in enhancing the A value and minimizing the B one, to have higher permeate flux while limiting the transport of solutes from the draw to the feed solution, which would reduce the driving force of the process hindering its throughput [14].

2.2. Advantages and Limitations of Forward Osmosis

Figure 3 summarizes the main advantages of the application of forward osmosis processes for water recovery. Firstly, thanks to the low required hydraulic pressure, the energetic consumption associated with forward osmosis is very low, with a positive impact on operating costs. The problem of fouling is then relatively small. Indeed, in FO process solutes deposition is generally reversible and most foulants are effectively repelled by the membrane itself. Finally, the presence of a high osmotic pressure gradient across the membrane makes forward osmosis potentially suitable for high efficiency water recovery applications [15].

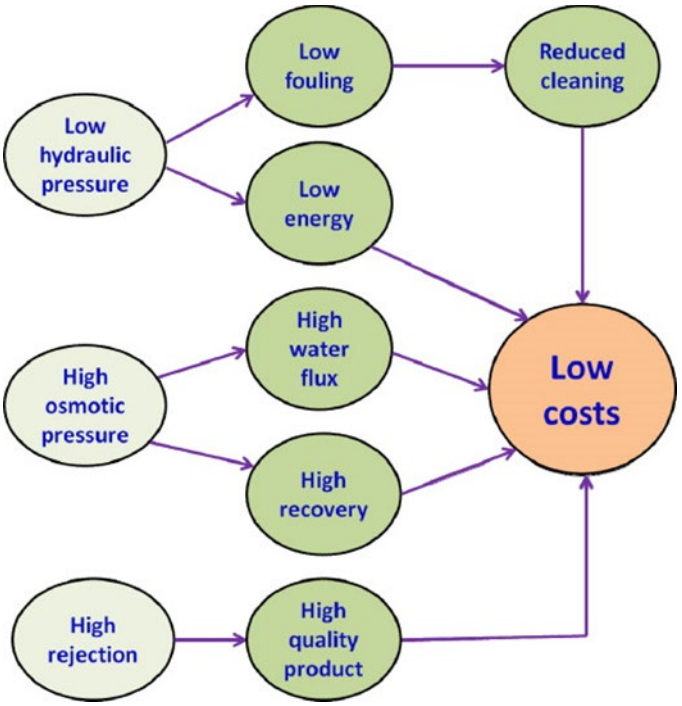

Figure 3. *Main advantages of forward osmosis processes [15].*

Despite the cited advantages and the increasing progress made by researchers on the optimization of osmotic processes, forward osmosis is still facing critics, mostly because of its limitations. The main drawback of such processes is concentration polarization, or rather the concentration increase at the membrane surface cause by mechanical rejection exerted by the membrane on the transported

solutes, which eventually accumulates in the boundary layer. The accumulation of solutes at the membrane proximity generates a concentration gradient which in turn determines a solute back flux toward the solution bulk, reducing the effective osmotic pressure and thus the permeate flux [13].

Solutes back diffusion represents a problem as well. Indeed, the transport of solutes from the draw to the feed side promoted by the concentration difference between the two solutions may lead to composition variations in the latter with potentially dangerous effects on the separation process [3].

3. Concentration Polarization Phenomena

Concentration polarization (CP) represents the main drawback of forward osmosis processes, since it negatively affects permeate flux [3]. Such phenomenon occurs during water permeation through the membrane and leads to sensible variations in the concentration gradients both on the membrane surface and inside its bulk, reducing the effective driving force.

Depending on where it takes place, concentration polarization can be divided into external concentration polarization (ECP) and internal concentration polarization (ICP), which in turn can be of concentrative or dilutive nature [3].

3.1. External Concentration Polarization (ECP)

When the feed solution flows across the active layer of the membrane, solutes accumulate and their concentration increases with respect to the solution bulk. This phenomenon is termed concentrative external concentration polarization. Parallelly, permeated water dilutes the draw solution lapping the membrane support layer, determining a dilutive external concentration polarization at the draw solution-membrane interface. Both ECP phenomena reduce the effective driving force. Concentrative ECP takes place when the support layer of the membrane faces the draw solution, whereas dilutive ECP occurs when the active layer faces the draw solution. The detrimental effects of ECP on the permeate flux can be mitigated by inducing turbulence or optimizing the flow field inside the membrane module to improve the degree of mixing [15].

Owing to the reduced hydraulic pressure that characterizes FO processes, ECP effects on water flux are milder compared to other pressure driven filtration processes. As a matter of fact, ECP is not addressed as the main cause of flux reduction in FO [11].

3.2. Internal Concentration Polarization (ICP)

Internal concentration polarization is the most important phenomenon hindering the performance of osmotic pressure driven processes. Indeed, the water flux decrease in FO is mainly caused by ICP, which may reduce the initial permeate flux up to 80% [16, 17].

Just like ECP, ICP may be dilutive and concentrative. Both phenomena take place inside the porous support layer and can be differentiated according to the orientation of the membrane as shown in Figure 4.

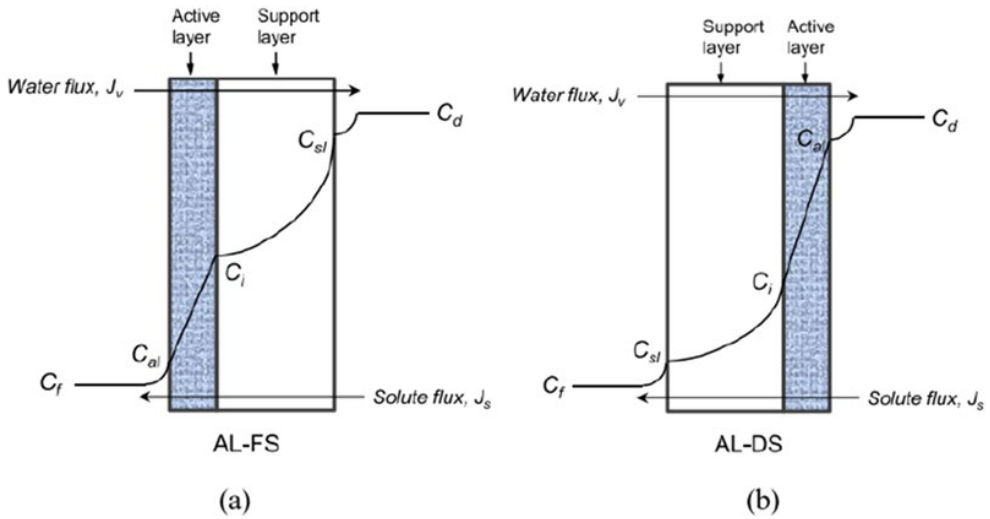

Figure 4. *Schematic representation of a membrane cross section affected by ICP. **(a)** AL-FS (Active Layer – Feed Side) configuration, **(b)** AL-DS (Active Layer-Draw side) configuration [18].*

When the draw solution faces the support layer (AL-FS configuration) (Figure 4a), permeated water determines a decrease in solute concentration across the support layer, leading to dilutive internal concentration polarization. On the other side, if the draw solution faces the active layer of the membrane (AL-DS configuration) (Figure 4b), solutes in the feed solution accumulate inside the support layer due to the permeation of water through the active layer. In this case, the phenomenon is termed concentrative internal concentration polarization.

Since ICP takes place inside the support layer, it can not be alleviated by optimizing the hydrodynamic of the system as for ECP [15].

Figure 5 clearly shows that the osmotic pressure gradient between the feed solution and the draw solution bulk ($\Delta\pi_{bulk}$) is higher than the osmotic pressure gradient across the membrane ($\Delta\pi_m$) due to ECP and that the effective driving force across the active layer ($\Delta\pi_{eff}$) is actually even smaller due to ICP.

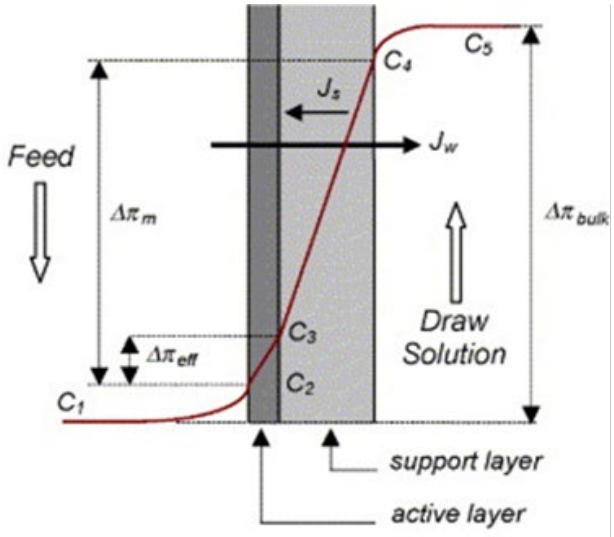

Figure 5. *Osmotic pressure differences across an asymmetric semipermeable membrane. The effects of ICP and ECP can be clearly observed by comparing the osmotic pressure gradients [15].*

3.3. Determination of the Structural Parameter

In FO applications, asymmetric semipermeable membranes are usually operated with the active side facing the feed solution. In such configuration, both concentrative ECP and dilutive ICP take place respectively on the feed and draw solution sides of the membrane. Differently from concentrative ECP, which can be minimized and is not responsible for the permeate flux reduction, dilutive ICP cannot be easily controlled and heavily affects water flux.

Dilutive ICP represents one of the biggest issues to face when dealing with FO processes modeling, indeed, such phenomenon is hard to be measured directly. In

order to assess the influence of ICP, a structural parameter S is employed for modeling purposes [19]. ICP can be modeled according to Equation (5):

$$\frac{\pi_{D,i}}{\pi_{D,b}} = \exp(-J_w K) \quad \textbf{(5)}$$

Considering a dilutive ICP, $\pi_{D,i}$ represents the osmotic pressure of the draw solution at the interface between the active layer and the support one, $\pi_{D,b}$ is the osmotic pressure in the draw solution bulk, whereas J_w is the water flux and K is the mass resistivity for diffusion within the membrane, defined as:

$$K = \frac{t\tau}{D\varepsilon} = \frac{S}{D} \quad \textbf{(6)}$$

where τ is the pore tortuosity ($1 < \tau < 2$), t the membrane thickness, ε the porosity and D the solute diffusion coefficient which can be obtained from the Stokes-Einstein equation. Equation (7) is used to describe the ICP model for mass transfer resistance developed by McCutcheon and Elimelech [20]:

$$K = \left(\frac{1}{J_w}\right) \ln\left(\frac{B + A\pi_{D,b}}{B + A\pi_{F,m} + J_w}\right) \quad \textbf{(7)}$$

The structural parameter S measures the actual length of the path followed by water diffusing through the support layer of the membrane, or rather the degree of ICP, and is used to represent the mass transfer resistance in an asymmetric membrane.

In the beginning, S was termed "intrinsic structural parameter" (S_{int}) and was determined by measuring structural properties of the membrane such as porosity, tortuosity and thickness:

$$S_{int} = \frac{t\tau}{\varepsilon} \quad \textbf{(8)}$$

In this way, S_{int} was constant and not influenced by the operating conditions.

In spite of a precise characterization of the membrane, S_{int} values are not accurate in real FO conditions, where temperature and pressure are not constant throughout the whole process. For these reasons, an effective structural parameter S_{eff} was developed:

$$S_{eff,FO} = \frac{D}{J_w} \ln\left(\frac{B + A\pi_{D,b}}{B + A\pi_{F,m} + J_w}\right) \quad \textbf{(9)}$$

where D ($m^2 s^{-1}$) is the solute diffusion coefficient, J_w (LMH) the water flux, A ($L\, m^{-2} h^{-1} bar^{-1}$) the water permeability coefficient, B ($g\, m^{-2} h^{-1}$) the solute permeability coefficient, $\pi_{D,b}$ the draw solution bulk osmotic pressure and $\pi_{F,m}$ the feed solution osmotic pressure at the membrane surface, which is considered equal to the bulk one ($\pi_{F,b}$) due to the negligible ECP.

4. Optimization of the Process Conditions in Forward Osmosis Processes for Water Recovery

Forward osmosis has been widely recognized as one of the most promising technologies playing an important role in alleviating the issues of water sustainability. The number of FO publications per year before 2005 were insignificant in number, however a steep increase has occurred during the last 13 years (2009–2021), accounting for 97.5% of total publications on such topic. This phenomenon revealed that the research on FO technology has only recently attracted significant attention from researchers [21].

Nevertheless, being based on concentration as driving force, FO has its own intrinsic limitations. The most important one concerns the net transfer of water across the membrane, which occurs until the point of osmotic equilibrium between the draw solution (DS), i.e. the most concentrated one, and the feed solution (FS). Without external intervention, it is impossible to dilute the DS beyond the point of osmotic equilibrium [22]. In order to maximize water recovery a useful approach lies in the optimization of process conditions.

In the following section, the role of three different process parameters in water recovery was explored by means of a microfluidic filtration module. Specifically, FS and DS flowrate variations were explored together with the effects of transmembrane concentration and membrane compaction under hydraulic pressure. The role of concentration polarization phenomena was studied as well.

4.1. Experimental

4.1.1. Materials and Methods

FO tests were carried out by means of cellulose triacetate (CTA) membranes (TSH20 Flat Sheet Membrane, CTA, FO, Sterlitech, USA) in the same microfluidic filtration device described in *Chapter 1 – Fouling Phenomena*,

section 5: Experimental Study on the Effect of Pumping Systems on Fouling Evolution. Both the feed and draw solutions were processed using peristaltic pumps (Cole-Palmer Masterflex L/S® Digital Drive with Easy-Load® II) in a countercurrent configuration. Permeated water samples were weighted at the end of every filtration test, taking into account the employed flowrate and the initial water volume present in the beaker containing the processed draw solution. $NaCl$ (HIMEDIA) was employed as a solute in the draw solution. An originally designed pulsation dampener was also employed during compaction tests to minimize pressure oscillations associated with the peristaltic pumps. Figure 6 depicts the experimental setup, including pressure sensors placed on the inlet side of the filtration cell and the beakers from which the feed and draw solutions are withdrawn and delivered.

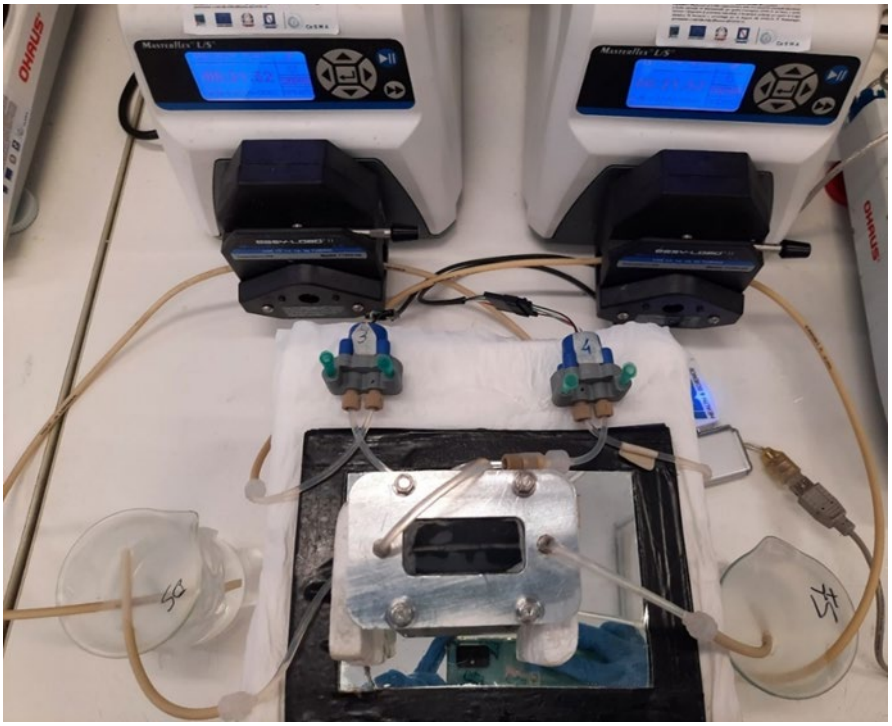

Figure 6. *FO experimental setup comprising the two peristaltic pumps used to process the feed and draw solutions, the microfluidic filtration module and the pressure sensors.*

Pure water recovery was evaluated as a function of various process conditions. Firstly it was calculated at different FS and DS flowrates with a pure water FS and a 2% $NaCl$ draw solution; afterwards, the DS and FS salt concentrations were varied at constant $\Delta c = 4.1\%$, employing a FS flowrate of $1.5\ \mathrm{ml\ min^{-1}}$ and a DS one of $15\ \mathrm{ml\ min^{-1}}$. Finally the application of a hydraulic pressure to compact the membrane was investigated.

Water recovery for active area unit was calculated as follows:

$$R|_A = \frac{|\bar{m}_{t=0} - \bar{m}_{t=30}|}{Q_F * 30} * \frac{1}{A} \quad \textbf{(10)}$$

where $\bar{m}_{t=0} - \bar{m}_{t=30}$ is the net permeated mass after 30 minutes, Q_F is the feed flowrate, whereas $A = 0.756\ \mathrm{cm^2}$ is the active surface area. Every test was repeated at least twice for a robust evaluation of mean and standard deviation. Prior to every filtration test, the system was cleaned for at least 30 minutes with deionized water to remove salt deposits; such operation will be termed priming.

4.2. Results and Discussion

4.2.1. Effect of the Inlet Flowrates

To investigate the effect of the inlet flowrates on water recovery, a pure water feed solution and a 2% $NaCl$ draw solution were used. The investigated flowrates were kept the same between FS and DS and were equal to 0.8, 1.5, 10 and $15\ \mathrm{ml\ min^{-1}}$.

The effect of flowrate variations was first investigated on the permeate mass, then on water recovery from the feed solution.

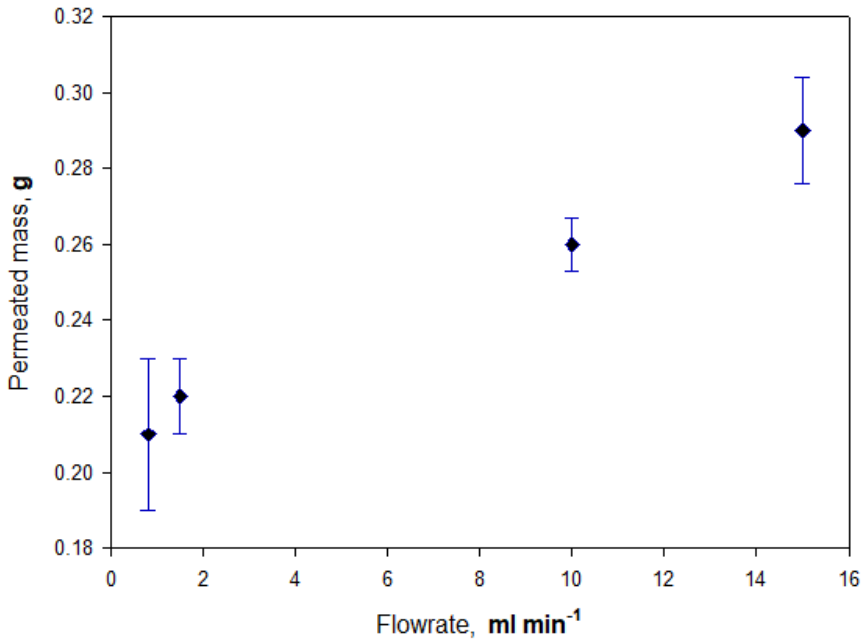

Figure 7. *Permeated mass as a function of FS/DS flowrate. Pure water was used for the FS, whereas a 2% $NaCl$ solution was used as DS.*

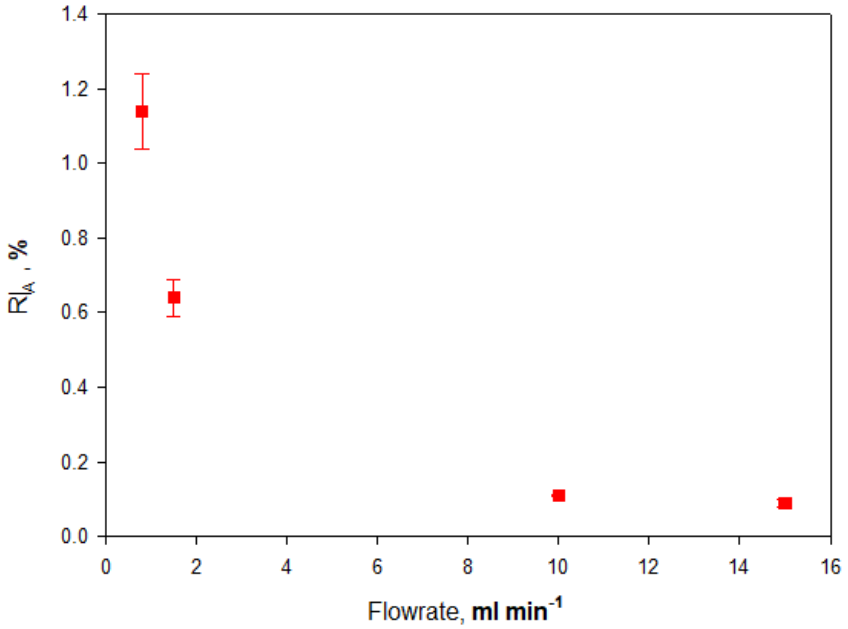

Figure 8. *Water recovery for active area unit as a function of FS/DS flowrate.*

Figure 7 and Figure 8 show how an increase in the FS and DS flowrates results in enhanced permeated mass values, yet in a decrease of water recovery. Results can

be explained considering by Equation (10) for the calculation of $R|_A$. Recovery decrease is related to the fact that the flowrate increase is actually bigger than the permeated mass one [23].

ICP is the main problem affecting FO performance due to the associated permeate flux reduction. In order to assess the influence of ICP, the structural parameter S was evaluated according to Equation (9), considering $\pi_{F,m} = \pi_{F,b} = 0$.

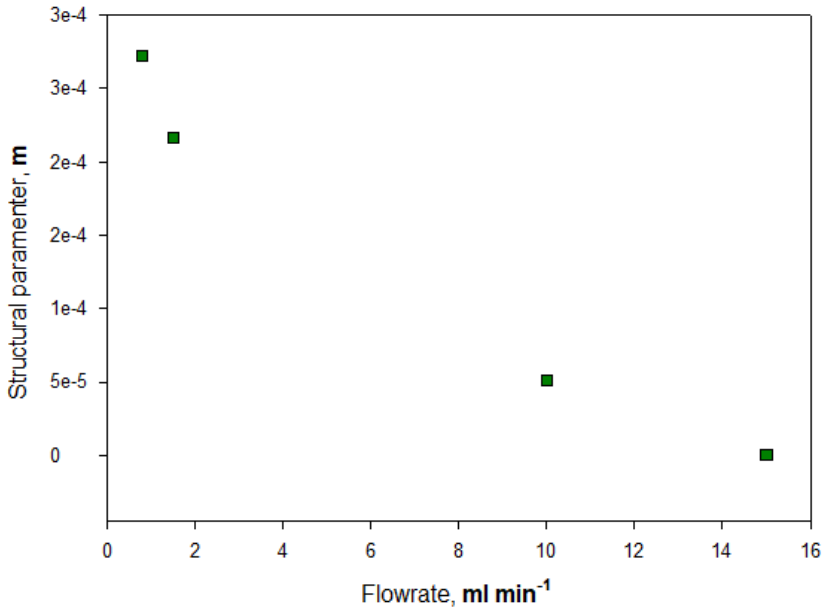

Figure 9. *Structural parameter as a function of FS/DS flowrate.*

Figure 9 shows a decreasing trend of the structural parameter as a function of FS and DS flowrates, indicating a reduced impact of concentration polarization. As a consequence, solutes diffuse through the support layer more easily, reducing salt concentration at the active layer and enhancing the effective driving force, which will be closer to the bulk one. Results are explained by the higher degree of mixing provided by the increased FS and DS flowrates, which hinder ICP and improves water flux [23].

Working at high flowrates minimizes the effects of ICP, resulting however in low water recovery values. Therefore, if the aim is to maximize the latter, working at low flowrates might be the best solution despite the heavier effects of ICP.

4.2.2. Effect of Concentration Variations

The effect of a parallel variation of both the FS and DS concentrations, while keeping a constant $\Delta c = 4.1\%$, was investigated employing a FS flowrate of $1.5\ \mathrm{ml\ min^{-1}}$ and a DS flowrate of $15\ \mathrm{ml\ min^{-1}}$. Specifically, concentration values reported in Table 1 were employed.

Table 1. *FS and DS $NaCl$ concentration values.*

Feed Solution	Draw Solution
0.9%	5%
2.9%	7.9%
4.9%	9%
6.9%	11%
8.9%	13%

The Δc value was selected based on the first concentration value for the feed solution, which corresponds to that of physiological saline, and on the will to keep the DS concentration low enough to prevent salt accumulation.

The effect of concentration variations was studied on permeated mass and water recovery.

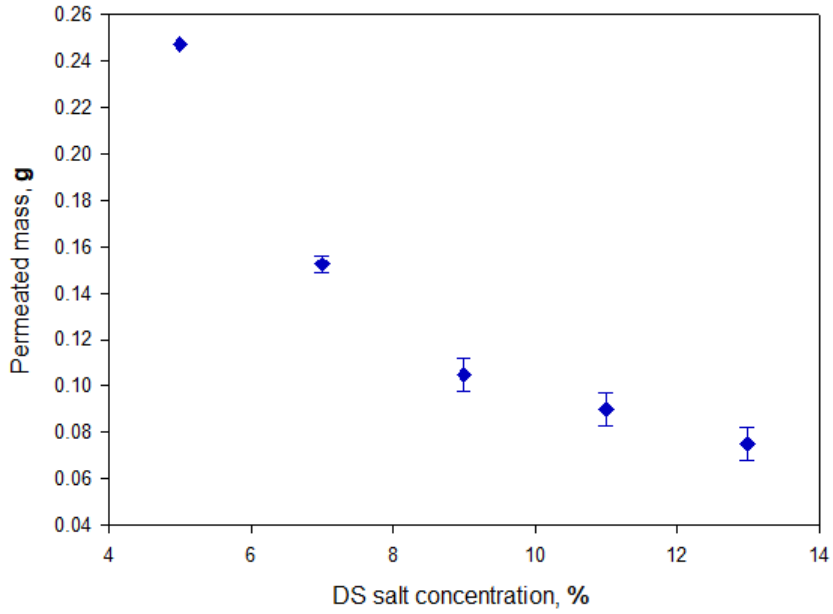

Figure 10. *Permeated mass as a function of draw solution salt concentration. Both Δc and inlet flowrates were kept constant and equal to 4.1%.*

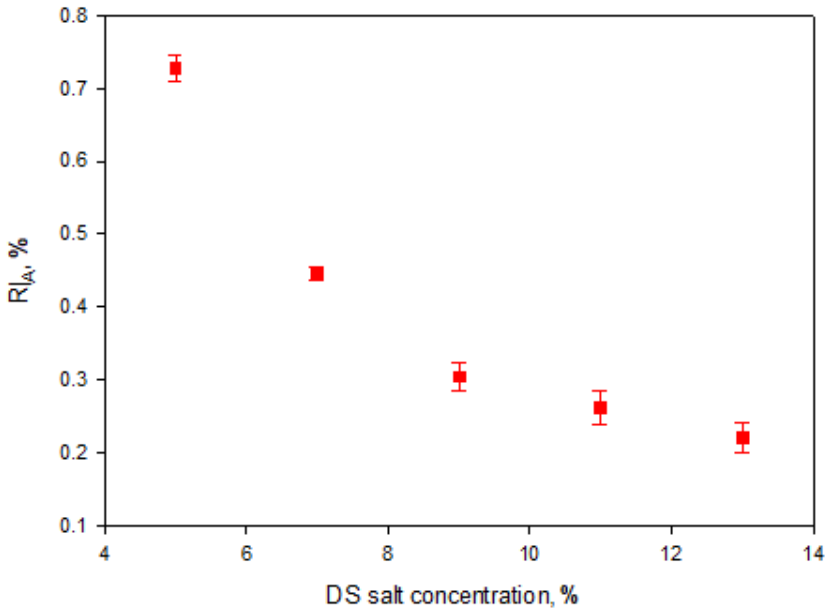

Figure 11. *Water recovery for active area unit as a function of draw solution salt concentration.*

Accordingly to the permeated mass trend (Figure 10), water recovery (Figure 11) also decreases at increasing DS (or FS) concentrations and constant flowrates. Such trends are related to the onset of dilutive ICP. Indeed, an increase in concentration for the processed solutions, especially for the DS, enhances solute buildup in the membrane support layer. Once again, due to the low characteristic permeate fluxes, ECP can be neglected, therefore the FS concentration increase has a marginal impact on the reduced water recovery [20].

To quantify the extent of the ICP, the structural parameter was evaluated according to Equation (10), considering ECP negligibility and thus $\pi_{F,m} = \pi_{F,b}$. Figure 12 clearly shows that increasing DS (or FS) concentration results in a rise of the structural parameter, indicating therefore greater dilutive internal concentration polarization. It can be concluded that, despite the same concentration difference between the FS and DS solutions, higher concentrations negatively impact on water recovery due to the detrimental effects of dilutive ICP, which reduce the effective driving force acting on water transport [20].

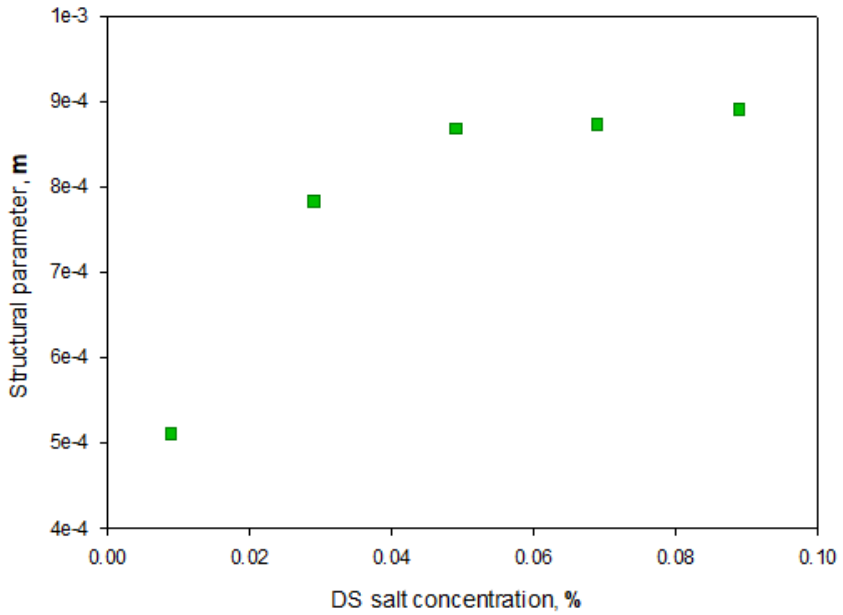

Figure 12. *Structural parameter as a function of draw solution salt concentration.*

Results show that the optimal operating conditions to maximize water recovery correspond to the following concentration values for the FS and DS respectively 0.9% and 5%, a flowrates of 1.5 ml min^{-1} and 15 ml min^{-1}.

4.2.3. Effect of Membrane Compaction

The effect of the application of a hydraulic pressure to compact the membrane during the priming process was finally investigated. Upon priming, filtration tests were carried out using a 5% $NaCl$ DS processed at 15 ml min^{-1} and a 0.9% $NaCl$ FS processed at 1.5 ml min^{-1}. Such conditions were selected owing to the good results provided for the optimization of FS and DS concentrations.

Membranes were compacted at 0, 200 and 400 mbar using only pure water on both sides of the membrane. Pressure was applied on the feed side of the system. Upon compaction, the FS and DS were processed without the application of any additional hydraulic pressure. Permeated mass and water recovery were evaluated. Only when membranes were compacted at 400 mbar, an additional filtration test was performed at the same transmembrane pressure to address any positive effect.

Results showed in Figure 13 and Figure 14 indicate the modest positive effect of membrane compaction on both permeated water and recovery. A further evaluation of the structural parameter points out a decreasing trend as a function of increasing compaction pressure, or rather a reduction of the ICP (Figure 15). Such trend may be justified by a reduction in the thickness of the membrane support layer, which positively affects water diffusion. No significant improvement was brought by the use of a hydraulic pressure of 400 mbar both during compaction and operation.

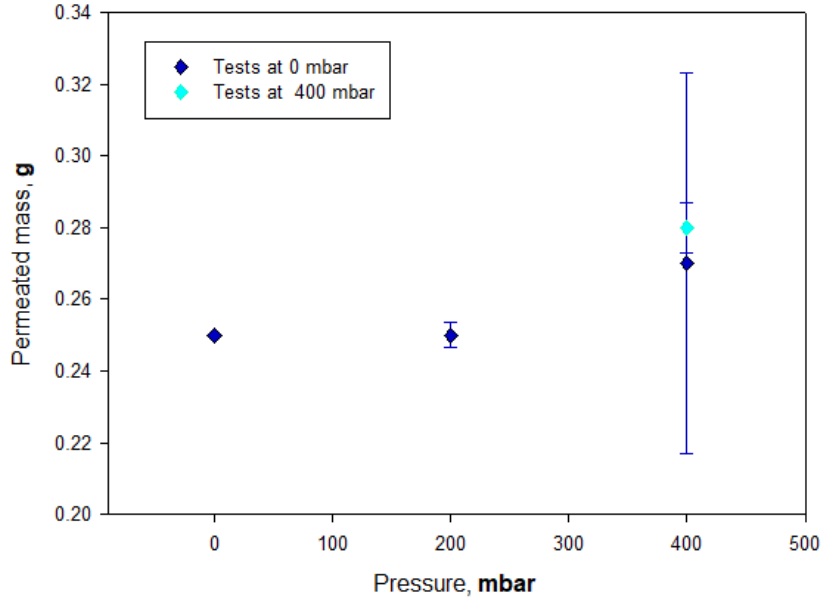

Figure 13. *Permeated mass as a function of compaction pressure. Filtration tests were carried out at the following FS and DS flowrates and concentrations, respectively:* $1.5\ ml\ min^{-1}$ *and* $15\ ml\ min^{-1}$*, 0.9% and 5%.*

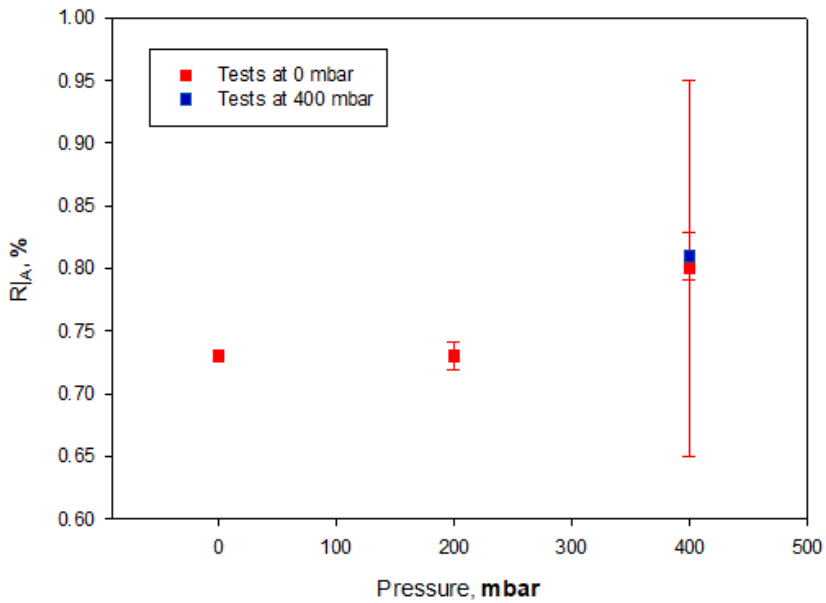

Figure 14. *Water recovery for active area unit as a function of compaction pressure.*

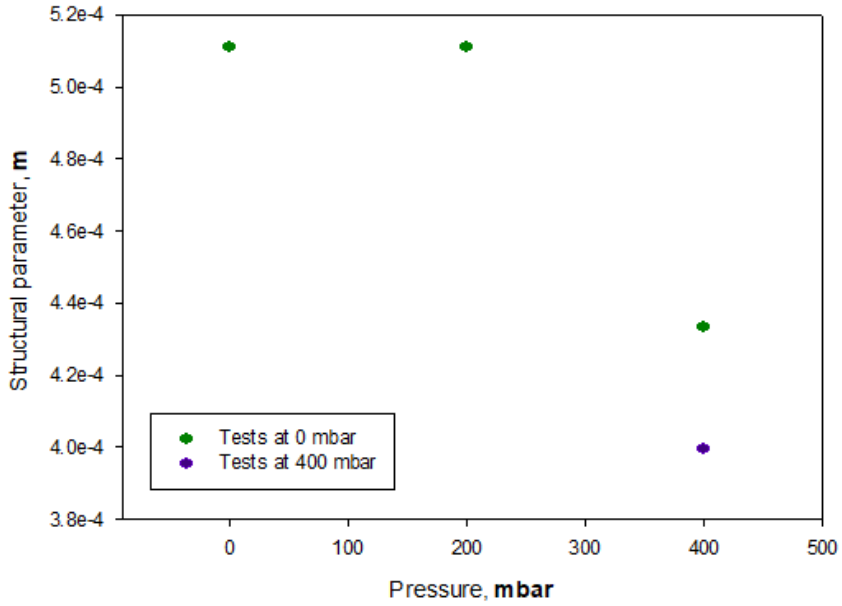

Figure 15. *Structural parameter as a function of compaction pressure.*

Membrane compaction was proved to be slightly effective in terms of water recovery maximization. Further tests at higher pressures are however needed to individuate an optimum, which will also be dependent on the energy expenses related to the higher compaction pressure.

5. Conclusions

Being an energy-efficient purification process, FO has been widely recognized as one of the most promising technologies playing a key role in alleviating the issue of water sustainability.

In this chapter the main concepts of forward osmosis were reviewed, with particular attention to concentration polarization. Taking place both on the outside and on the inside of the membranes (ECP and ICP), this phenomena represent one of the main drawbacks of FO, causing flux decrease and process throughput loss.

An experimental study on the optimization of process parameters in FO to maximize water recovery was then presented. Such study was carried out with the help of a microfluidic filtration module, which enabled a high resolution investigation of the impact of the inlet flowrates, feed and draw solution concentrations and membrane compaction on permeate flux. The role of concentration polarization was investigated as well by means of the evaluation of structural parameter, which measures the average distance a solute molecule has to cross through the support layer when transported from the draw solution bulk to the membrane active layer. Results pointed out the detrimental effects of concentration polarization on water recovery. Indeed, despite the use of the same theoretical driving force (i.e., concentration difference), at higher salt concentrations a lower amount of recovered water was observed due to the heavier impact of concentration polarization, as denoted by the higher values of the structural parameters.

References

[1] F. Morante-Carballo, N. Montalván-Burbano, X. Quiñonez-Barzola, M. Jaya-Montalvo, P. Carrión-Mero, What Do We Know about Water Scarcity in Semi-Arid Zones? A Global Analysis and Research Trends, Water 14(17) (2022) 2685.
[2] D. Alex Mikaberidze Ph, Letter To The Editor: "Letter to the Editor", The Journal of Slavic Military Studies 20(1) 135-136 , year = 2007. https://doi.org/10.1080/13518040701205365.
[3] A. Haupt, A. Lerch, Forward osmosis application in manufacturing industries: A short review, Membranes 8(3) (2018) 47.
[4] Y. Jiao, C. Zhao, Y. Kang, C. Yang, Microfluidics-based fundamental characterization of external concentration polarization in forward osmosis, Microfluidics and Nanofluidics 23(3) (2019) 1-10.
[5] Y. Kaufman, R. Kasher, R.G. Lammertink, V. Freger, Microfluidic NF/RO separation: Cell design, performance and application, Journal of membrane science 396 (2012) 67-73.
[6] C. Completo, V. Geraldes, V. Semião, M. Mateus, M. Rodrigues, Comparison between microfluidic tangential flow nanofiltration and centrifugal nanofiltration for the concentration of small-volume samples, Journal of Membrane Science 578 (2019) 27-35.
[7] A. Inc., The difference between forward and reverse osmosis? https://aquaporin.com/difference-between-fo-and-ro/.
[8] P.G. Nicoll, Forward osmosis—A brief introduction, Proceedings of the international desalination association world congress on desalination and water reuse, Tianjin, China, 2013, pp. 20-25.
[9] A.I. Cirillo, G. Tomaiuolo, S. Guido, Membrane Fouling Phenomena in Microfluidic Systems: From Technical Challenges to Scientific Opportunities, Micromachines 12(7) (2021) 820.
[10] A. Tiraferri, N.Y. Yip, W.A. Phillip, J.D. Schiffman, M. Elimelech, Relating performance of thin-film composite forward osmosis membranes to support layer formation and structure, Journal of membrane science 367(1-2) (2011) 340-352.
[11] T.Y. Cath, A.E. Childress, M. Elimelech, Forward osmosis: principles, applications, and recent developments, Journal of membrane science 281(1-2) (2006) 70-87.
[12] H. Chu, W. Zhang, L. Wang, X. Wei, Z. Yu, Y. Zhang, X. Zhou, Cellulose triacetate (CTA)-based forward osmosis membranes for water purification: optimization of dope solution composition and preparation conditions, Desalination and Water Treatment 106 (2018) 11-20.
[13] P. Mark, Forward osmosis (FO) membranes and membrane processes. https://www.forwardosmosistech.com/forward-osmosis-membranes-and-membrane-processes/.

[14] W. Suwaileh, N. Pathak, H. Shon, N. Hilal, Forward osmosis membranes and processes: A comprehensive review of research trends and future outlook, Desalination 485 (2020) 114455.
[15] S. Zhao, L. Zou, C.Y. Tang, D. Mulcahy, Recent developments in forward osmosis: Opportunities and challenges, Journal of membrane science 396 (2012) 1-21.
[16] C.H. Tan, H.Y. Ng, Revised external and internal concentration polarization models to improve flux prediction in forward osmosis process, Desalination 309 (2013) 125-140.
[17] J.-G. Gai, X.-L. Gong, Zero internal concentration polarization FO membrane: functionalized graphene, Journal of Materials Chemistry A 2(2) (2014) 425-429.
[18] A. Karabelas, T. Matsuura, S. Hong, REVIEWS ON RESEARCH AND DEVELOPMENT IN DESALINATION, Desalination 434 (2018) 1-1.
[19] J.F. Sark, N. Jullok, W.J. Lau, Improving the Structural Parameter of the Membrane Sublayer for Enhanced Forward Osmosis, Membranes 11(6) (2021) 448.
[20] J.R. McCutcheon, M. Elimelech, Influence of concentrative and dilutive internal concentration polarization on flux behavior in forward osmosis, Journal of membrane science 284(1-2) (2006) 237-247.
[21] W.L. Ang, A.W. Mohammad, D. Johnson, N. Hilal, Forward osmosis research trends in desalination and wastewater treatment: A review of research trends over the past decade, Journal of Water Process Engineering 31 (2019) 100886.
[22] S. Phuntsho, S. Hong, M. Elimelech, H.K. Shon, Osmotic equilibrium in the forward osmosis process: Modelling, experiments and implications for process performance, Journal of membrane science 453 (2014) 240-252.
[23] R. Jalab, A.M. Awad, M.S. Nasser, J. Minier-Matar, S. Adham, Pilot-scale investigation of flowrate and temperature influence on the performance of hollow fiber forward osmosis membrane in osmotic concentration process, Journal of Environmental Chemical Engineering 8(6) (2020) 104494.

Conclusions

The application of microfluidics to the study of different membrane separation processes (e.g., microfiltration and forward osmosis) constitutes a new and interesting approach whose scientific relevance is still increasing. Indeed, in the presented PhD thesis the use of micro-confined technologies was demonstrated to be effective for the investigation of relevant phenomena such as fouling with high spatial and temporal resolutions, enabling even small changes like those concerning the deposits' morphology to be pointed out.

In the first chapter, the main concepts regarding fouling and microfluidics were introduced. The evolution of fouling was characterized by its stages and the main interactions involved in foulant deposition were discussed. A modeling approach was also explored for the characterization of the predominant fouling mechanisms. Finally, several *in situ* microfluidic investigation techniques were analyzed as potential approaches capable of overcoming the limitations of the current monitoring techniques, which relate on permeate flux and TMP variations measurement. An experimental study on the effect of different pumping systems on the evolution of fouling from protein solutions was then presented. The whole study was carried out by means of an originally designed microfluidic filtration module and the effects of membrane pore size and $\overline{\mathrm{TMP}}$ were assessed as well. Results pointed out the key role of foulant residence time inside the membrane on both fouling propensity and deposit morphology, showing a significant influence of the pumping system which in some cases can actually alleviate flux decrease.

Fouling mitigation strategies were the topic of interest of the second chapter. Here, three classes of mitigation approaches were identified, each one affecting a specific stage of foulants deposition. The optimization of the process conditions was discussed to be the most cost-effective strategy, whereas membrane cleaning was examined for its efficacy in terms of flux recovery. A deeper focus was given to membrane modification techniques, which represent a promising approach to

prevent fouling. In these regards, two experimental studies were described concerning membrane coating and membrane nano-structure modification. The former was carried out in a microfluidic filtration system and assessed the influence of improved hydrophilicity on membrane antifouling properties. Results showed how a mere increase in hydrophilicity was not enough to effectively mitigate protein deposition either on hydrophobic or hydrophilic commercial membranes. Despite the excellent separation performance, polymeric membranes are usually sensible to organic solvents, being therefore not suitable for modification such as the incorporation of antifouling molecules on the surface. In the latter study, the attention was shifted from deposition processes to membrane chemistry and a set of tunable, solvent resistant nanofiltration membranes was developed to be suitable for zwitterion grafting via SI-ATRP. According to results, polyDMAPS chains were successfully grown on the membrane surface via a "grafting from" approach, constituting therefore a nanofiltration membrane with high antifouling potential.

In the last chapter of this work, forward osmosis processes were explored. The main notions regarding this osmotic driven separation process were revied and concentration polarization was discussed as the most relevant issue affecting water recovery. An experimental study on the use of microfluidics for the optimization of process parameters in FO was then presented. Water recovery was selected as the variable to be maximized and the effects of flowrate changes, concentration increases and membrane compaction were assessed.

The results obtained in this research work aim to help the scientific community fill the gaps in the understanding of fouling, which despite being the main drawback of membrane separation processes still represents a partially unsolved challenge.

List of Publications

Published papers

- Cirillo, A.I.; Tomaiuolo, G.; Guido, S. *Membrane Fouling Phenomena in Microfluidic Systems: From Technical Challenges to Scientific Opportunities*. Micromachines 2021, 12, 820. https://doi.org/10.3390/mi12070820

In preparation papers

- Cirillo, A. I.; Tomaiuolo, G.; Guido, S. *Effect of processing conditions on membrane fouling in microfiltration by a miniaturized modular device*;
- Cirillo, A. I.; Tomaiuolo, G.; Guido, S. *Effect of process conditions on forward osmosis in water recovery applications;*
- Cirillo, A.I.; Ouimet J.A.; Phillip, W.A.; Tomaiuolo G.; Guido S. *Development and characterization of tunable, solvent resistant, nanoporous membranes suitable for SI-ATRP antifouling functionalization*.

Activities

Attended conferences, oral presentations and posters

- Oral presentation at cREOgiovani 2021 - online conference (http://www.sirreologia.com/creogiovani/index.asp);
- Oral presentation at Euromembrane 2021 – Copenhagen (Denmark) (https://euromembrane2021.eu/);
- Oral presentation at AERC 2022 – Seville (Spain) (https://www.aercsevilla2022.es/aerc2022/welcome);
- Oral presentation at SoftComp/EUSMI Annual Meeting 2022 – Salerno (Italy) (https://eu-softcomp.net/news/meetings/softcomp-annual-meeting-2022/);

- Poster presentation at GRS & GRC Membranes: Materials and Processes 2022 – New London (USA) (https://www.grc.org/membranes-materials-and-processes-conference/2022/);
- Poster presentation at CBE Graduate Research Symposium – Notre Dame (USA) (https://cbegso.nd.edu/symposium/);